

---

# Development and characterization of a transportable aluminum ion quantum logic optical clock setup

---

Von der QUEST-Leibniz-Forschungsschule der  
Gottfried Wilhelm Leibniz Universität Hannover

zur Erlangung des Grades  
Doktor der Naturwissenschaften  
Dr. rer. nat.

genehmigte Dissertation  
von

Stephan Hannig, M.Sc.  
geboren am 23. Dezember 1988 in Minden

2018

Referent: Prof. Dr. Piet O. Schmidt  
Koreferent: Prof. Dr. Christian Ospelkaus  
Tag der Promotion: 24.08.2018

# Abstract

At the time of writing, state of the art stationary optical clocks reach  $10^{-18}$  systematic fractional frequency uncertainty, which allows for the search of new physics beyond the standard model and lays the foundation for new applications such as chronometric leveling, where height differences relative to the geoid are derived from frequency comparisons among optical clocks.

Transportable optical clocks allow for chronometric leveling between distant locations which are not connected by a direct line of sight but via length stabilized optical fiber. Moreover, they facilitate frequency comparisons between distant stationary clocks via subsequent side-by-side comparisons without the necessity of a long-range fiber connection. A transportable optical clock employing a single  $^{40}\text{Ca}^+$  ion has been reported and a neutral atom  $^{87}\text{Sr}$  lattice clock has been employed in a chronometric leveling campaign. However, these clocks report an estimated systematic fractional frequency uncertainty in the high  $10^{-17}$  range, which limits their height resolution to a level of approximately 1 m.

$^{27}\text{Al}^+$  has one of the smallest blackbody radiation shifts, small linear and quadratic Zeeman shifts and a negligible quadrupole shift, which makes it a candidate for a highly accurate optical clock. This thesis reports on the development, set-up, and characterization of a transportable  $^{27}\text{Al}^+$  clock setup with  $^{40}\text{Ca}^+$  as logic ion. The setup is simple, modular, compact, and mechanically stable. Ions of both species are generated via pulsed laser ablation and subsequent photoionization. They are confined in a multi-layer trap with segmented loading and experiment zones. Using a single  $^{40}\text{Ca}^+$  ion as probe, heating rates of below 10 quanta per second have been measured in all three directions for trap frequencies around  $2\pi \times 2\text{ MHz}$ , and pulsed sideband cooling to mean motional quantum numbers below 0.1 quanta was demonstrated. Imaging close to the diffraction limit with a signal to noise ratio of 800 for 300 ms exposure time on a sCMOS camera was achieved using a single  $\text{NA} = 0.51$  biaspheric lens. Simultaneously, a state discrimination error below  $10^{-5}$  in 100  $\mu\text{s}$  was obtained using a PMT. From the excess micromotion second order Doppler shift, secular motion second order Doppler shift, BBR shift, and background gas collision shift, a partial systematic fractional frequency uncertainty of  $1.7 \times 10^{-18}$  was inferred, which is equivalent to a height resolution of ca. 2 cm.

Moreover, a highly stable mechanical monolithic enhancement cavity for SHG has been developed and demonstrated to withstand accelerations of  $3 g_{\text{rms}}$  for 30 min. It has been operated for an uninterrupted period of 130 h without decay in output power in the mid-UV due to  $\text{O}_2$ -purging, its sealed design, and material selection, which solves the often observed crystal degradation in UV applications. The cavity has been employed in the  $^{27}\text{Al}^+$  logic laser system.

In conclusion, it has been shown that an  $^{27}\text{Al}^+$  ion quantum logic optical clock operated in the present transportable setup could reach an estimated systematic fractional frequency uncertainty of  $1.7 \times 10^{-18}$ , provided that all other shifts, such as the second order Zeeman shift, are negligible. This paves the way towards chronometric leveling with an unprecedented height resolution of about 2 cm.

**Keywords:** Transportable  $^{27}\text{Al}^+$  ion clock, highly stable SHG cavity



## Zusammenfassung

Aktuell erreichen ortsfeste optische Uhren eine relative systematische Frequenzunsicherheit von  $10^{-18}$ . Diese ermöglicht die Suche nach physikalischen Effekten jenseits des Standardmodells und bildet die Grundlage für neue Anwendungen wie z.B. Höhenmessung anhand optischer Frequenzvergleiche. Transportable optische Uhren erlauben die Messung von Höhendifferenzen zwischen Orten, welche nicht über eine direkte Sichtlinie, sondern eine längenstabilisierte Glasfaser verbunden sind. Des Weiteren können Dank ihnen auch die Frequenzen solcher ortsfester Uhren verglichen werden, die über keinerlei Glasfaserverbindung verfügen, indem die ortsfesten Uhren einzeln nacheinander mit der transportablen Uhr verglichen werden. Zwar wurde bereits eine transportable  $^{40}\text{Ca}^+$  Einzelionenuhr vorgestellt und mit einer  $^{87}\text{Sr}$  Gitteruhr eine Höhenmessung durchgeführt, jedoch erreichen diese Uhren eine relative systematische Frequenzunsicherheit im hohen  $10^{-17}$ -Bereich, welches die erreichbare Höhenauflösung auf ca. 1 m limitiert.

$^{27}\text{Al}^+$  hingegen weist eine der kleinsten Schwarzkörper-Verschiebungen sowie geringe lineare und quadratische Zeeman-Verschiebungen auf. Da zudem die Quadrupolverschiebung vernachlässigbar ist, ist  $^{27}\text{Al}^+$  ein Kandidat für die genaueste optische Uhr. Diese Arbeit hat die Entwicklung, den Aufbau und die Charakterisierung einer transportablen  $^{27}\text{Al}^+$ -Uhr mit  $^{40}\text{Ca}^+$  als Logik-Ion zum Gegenstand. Der vorgestellte Aufbau ist einfach, modular, kompakt und mechanisch stabil. Ionen beider Spezies werden durch gepulste Laserablation mit anschließender Photoionisation erzeugt und in einer mehrlagigen segmentierten Falle gefangen. Mit einem einzelnen  $^{40}\text{Ca}^+$  Ion wurden bei Fallenfrequenzen von gerundet 2 MHz Heizraten von weniger als 10 Phononen pro Sekunde in allen drei Raumrichtungen gemessen und mittlere Besetzungszahlen von unter 0.1 Phononen mithilfe von gepulstem Seitenbandkühlen erzielt. Mittels einer biasphärischen Linse mit  $\text{NA} = 0.51$  werden Ionen nahezu beugungsbegrenzt auf einer sCMOS Kamera abgebildet, wobei für eine Belichtungszeit von 300 ms ein Signal-Rausch-Verhältnis von 806.1 erzielt wird. Gleichzeitig lässt sich innerhalb von 100  $\mu\text{s}$  mit einem PMT der Zustand mit einem Fehler von unter  $10^{-5}$  bestimmen. Aus den Messungen der fallenspezifischen Frequenzverschiebungen wurde eine systematische Frequenzunsicherheit von  $1.7 \times 10^{-18}$  abgeschätzt, welche einer Höhenauflösung von ca. 2 cm entspricht.

Des Weiteren wurde ein mechanisch hoch stabiler optischer Resonator zur Frequenzverdopplung entwickelt, welcher Beschleunigungen von  $3 g_{\text{rms}}$  über eine Dauer von 30 min standhält. Während 130 Stunden ununterbrochenen Betriebs wurde kein Rückgang der Ausgangsleistung im mittleren UV beobachtet. Somit lösen die eingesetzte  $\text{O}_2$ -Spülung, das gasdichte Design und die verwendeten Materialien das Problem der oft beobachteten Kristalldegradation in UV-Anwendungen. Der Resonator wurde zum Bestandteil des  $^{27}\text{Al}^+$  Logiklaser-Systems.

Zusammenfassend ist festzustellen, dass eine optische  $^{27}\text{Al}^+$  Quantenlogikuhr in dem hier vorgestellten transportablen System eine relative systematische Frequenzunsicherheit von  $1.7 \times 10^{-18}$  erreichen kann. Damit werden Höhenmessungen durch optische Frequenzvergleiche mit einer unerreichten Auflösung von ca. 2 cm möglich.

**Schlagwörter:** Transportable  $^{27}\text{Al}^+$  Ionenuhr, hochstabile Verdopplungsresonatoren

# Contents

<b>1. Introduction</b>	<b>1</b>
<b>2. Foundations and theoretical background</b>	<b>7</b>
2.1. Optical clocks . . . . .	7
2.1.1. Concept of optical ion clocks . . . . .	7
2.1.2. Optical clocks: figures of merit . . . . .	9
2.2. Ion trapping in linear Paul traps . . . . .	11
2.3. Light interaction of a trapped ion . . . . .	15
2.4. The clock ion . . . . .	18
2.5. The logic ion . . . . .	19
2.6. Quantum logic spectroscopy . . . . .	20
<b>3. Transportable aluminum optical clock setup</b>	<b>23</b>
3.1. Ion trap . . . . .	23
3.2. RF drive source . . . . .	26
3.3. DC voltage source . . . . .	28
3.4. Vacuum system . . . . .	30
3.5. Coil system . . . . .	31
3.6. Laser system for ionization and Doppler cooling . . . . .	32
3.6.1. Wavelength meter laser frequency stabilization . . . . .	34
3.7. Calcium logic laser system . . . . .	38
3.8. Optical setup around the vacuum chamber . . . . .	40
3.9. Imaging system . . . . .	42
3.10. Ablation targets . . . . .	47
3.10.1. Aluminum ion generation . . . . .	48
3.10.2. Time of flight measurements . . . . .	50
3.10.3. Aluminum ion trapping . . . . .	57
3.11. Experimental control system . . . . .	60
3.12. Transportability . . . . .	61

<b>4. Measurements</b>	<b>65</b>
4.1. Laser cooling . . . . .	65
4.1.1. First stage: Doppler cooling . . . . .	66
4.1.2. Second stage: Sideband cooling . . . . .	67
4.1.3. Experimental implementation of ground state cooling . . . . .	68
4.2. Excess micromotion compensation . . . . .	71
4.3. Error budget . . . . .	78
<b>5. Aluminum logic laser system</b>	<b>85</b>
5.1. Higher harmonic generation theory . . . . .	86
5.2. A setup for second harmonic generation to the UV . . . . .	90
5.2.1. Length stabilization and its limit . . . . .	96
5.3. Cavity design . . . . .	97
5.4. Setup . . . . .	99
5.5. Experiment . . . . .	102
5.5.1. SHG to 267 nm in the first generation cavity . . . . .	105
5.5.2. Summary of the first generation SHG cavity . . . . .	107
5.6. Second generation UV SHG cavity . . . . .	108
5.7. Aluminum logic laser setup . . . . .	109
<b>6. Summary and Outlook</b>	<b>115</b>
6.1. Summary . . . . .	115
6.2. Outlook . . . . .	118
<b>A. Appendix</b>	<b>123</b>

# List of Figures

2.1. Functional principle of an optical clock. . . . .	9
2.2. Frequency accuracy and stability . . . . .	10
2.3. Linear Paul trap. . . . .	12
2.4. Ion trap potentials. . . . .	13
2.5. Quantum harmonic oscillator. . . . .	16
2.6. Product states. . . . .	18
2.7. Reduced $^{27}\text{Al}^+$ level scheme. . . . .	18
2.8. Reduced $^{40}\text{Ca}^+$ level scheme. . . . .	20
2.9. Quantum logic spectroscopy sequence. . . . .	21
3.1. Segmented multi-layer trap. . . . .	24
3.2. Trap assembly. . . . .	26
3.3. Trap drive rf chain. . . . .	27
3.4. Radial modes versus trap drive power. . . . .	28
3.5. Axial trap frequency versus confining potential. . . . .	29
3.6. Vacuum setup. . . . .	31
3.7. Laser setup for ionization and Doppler cooling. . . . .	33
3.8. Wavelength meter frequency stabilization. . . . .	35
3.9. Wavelength meter drift characterization. . . . .	36
3.10. Stability of the wavelength meter frequency readout. . . . .	37
3.11. $^{40}\text{Ca}^+$ logic laser system. . . . .	38
3.12. Vacuum chamber and surrounding optics . . . . .	41
3.13. Imaging system. . . . .	43
3.14. Imaging performance. . . . .	44
3.15. State discrimination error vs. detection time. . . . .	46
3.16. Ablation target. . . . .	47
3.17. Setup and sequence for Al TOF measurements. . . . .	51
3.18. Fluorescence vs. TOF and ionization laser frequency. . . . .	52
3.19. Fluorescence vs. TOF and ablation laser power. . . . .	53

*List of Figures*

3.20. Fluorescence vs. TOF and target bias potential. . . . .	54
3.21. Fluorescence vs. TOF and ablation laser spot position. . . . .	55
3.22. Aluminum time of flight spectrum and velocity distribution. . . . .	56
3.23. $^{27}\text{Al}^+$ loading sequence. . . . .	57
3.24. $^{27}\text{Al}^+$ energy budget. . . . .	59
3.25. $^{27}\text{Al}^+$ loading. . . . .	60
3.26. Physics package. . . . .	61
3.27. Schematic inner layout of the clock-container. . . . .	62
4.1. Sideband coolings scheme. . . . .	68
4.2. 729 nm transition structure. . . . .	69
4.3. Sideband cooling sequence. . . . .	69
4.4. Axial heating rate measurement. . . . .	70
4.5. Micromotion in the radial plane of a linear Paul trap. . . . .	73
4.6. Micromotion compensation methods. . . . .	74
4.7. Excess micromotion compensation. . . . .	76
4.8. Rf field along the axial direction. . . . .	77
4.9. Rabi excitation on the carrier. . . . .	77
4.10. EMM second order Doppler shift along the trap axis. . . . .	80
5.1. SHG in BBO: phasematching and angle definitions. . . . .	89
5.2. Cavity layouts: linear versus bow-tie. . . . .	92
5.3. Cross section of the first generation SHG cavity. . . . .	97
5.4. Complete setup for 313 nm generation. . . . .	99
5.5. Long term SHG output power measurement at 313 nm. . . . .	103
5.6. Cavity SHG output power during vertical acceleration excitation. . .	104
5.7. SHG power before and after 30 min ISO 13355:2016 shaker test. . . .	105
5.8. 267 nm output power recording 1 <sup>st</sup> generation cavity. . . . .	106
5.9. BBO facet after 267 nm generation . . . . .	107
5.10. Cross section of the second generation UV SHG cavity. . . . .	108
5.11. Overview of the 267 nm $^{27}\text{Al}^+$ logic laser system. . . . .	110
5.12. Spectroscopy on the $^1\text{S}_0 \rightarrow ^3\text{P}_1$ logic transition in $^{27}\text{Al}^+$ . . . . .	111
A.1. Characterization B-field coils. . . . .	123
A.2. Characteristic curve 1068 nm fiber amplifier. . . . .	125
A.3. Characteristic curve single-pass waveguide SHG IR to VIS. . . . .	125

A.4. 267 nm output power recording 2<sup>nd</sup> generation cavity. . . . . 126  
A.5. Cross section 2<sup>nd</sup> generation UV to VIS SHG cavity. . . . . 126





# List of Tables

4.1. Average motional quantum numbers and heating rates measured on a single $\text{Ca}^+$ ion after pulsed sideband cooling to the ground state and micromotion compensation. . . . .	71
4.2. Residual rf field at the trap center. . . . .	76
4.3. Mode frequencies and scaling factors for the $^{27}\text{Al}^+ / ^{40}\text{Ca}^+$ crystal. . .	79
4.4. Estimated apparatus-related partial error budget in fractional units. .	82
5.1. Geometric parameters of the 626 nm SHG cavity. . . . .	95
A.1. Parameters of the B-field coils. . . . .	123
A.2. Dimensions of the helical resonator. . . . .	124
A.3. Biaspherical lens surface profile parameters. . . . .	124



# Nomenclature

## Latin Letters

Variable	Meaning	Unit
$c$	speed of light	m/s
$B$	walk-off parameter	1
$B$	magnetic field	$\frac{\text{kg}}{\text{A}\cdot\text{s}^2}$
$b$	confocal parameter	m
$d$	distance	m
$d_{ij}$	component of nonlinear dielectric susceptibility tensor	$\frac{\text{A}\cdot\text{s}}{\text{V}^2}$
$E$	electric field	V/m
$F$	finesse	1
$f$	frequency	Hz
$f$	focal length	m
$k$	wavenumber	1/m
$l$	length	m
$m / M$	mass	kg
$P$	power	$\frac{\text{kg}\cdot\text{m}^2}{\text{s}^3}$
$r$	radius	m
$R$	reflectivity	1
$T$	transmittivity	1
$U$	electric potential	V

## Greec Letters

Variable	Meaning	Unit
$\alpha$	light absorbtion coefficient	1/cm
$\theta_B$	Brewster's angle	rad.
$\theta_{pm}$	phasematching angle	rad.
$\kappa_0$	linear dielectric susceptibility	$\frac{A \cdot s}{m \cdot V}$
$\kappa$	SHG conversion coefficient	$\frac{s^3}{kg \cdot m^2}$
$\lambda$	wavelength	m
$\omega$	angular frequency	$2\pi \times \text{MHz}$
$\tau$	averaging time	s
$\varrho$	walk-off angle	rad.
$\chi^{(2)}$	2 <sup>nd</sup> order nonlinear dielectric susceptibilities	$\frac{A \cdot s}{V^2}$

## Indices

Index	Meaning
ax	axial
B	Brewster
Beat	(optical) Beat
c	crystal
cm	curved mirror
diag	diagonal
e	extra ordinary
geo	geometric
ic	incoupling
M	mirror
Mon	monitor
meas	measured
o	ordinary
PL	pump light
pm	phasematching
rad	radial
rf	radio frequency
SHG	second-harmonic generation
vert	vertical

## Acronyms

Acronym	Meaning
ABL	ablation laser
ABT	ablation target
AMP	amplifier
AOM	acousto-optic modulator
AP	aperture
ASL	aspheric lens
AT	attenuator
BBR	black-body radiation

## Nomenclature

<b>Acronym</b>	<b>Meaning</b>
BP	band-pass filter
BSB	blue sideband transition
CCD	charge coupled device
CIC	clock-induced charges
CMOS	Complementary metal-oxide-semiconductor
COM	center of mass
CTE	coefficient of thermal expansion
DAC	digital analog converter
DFB	distributed feedback grating
DM	dichroic mirror
e	extra ordinary
ECDL	external-cavity diode laser
EIT	electromagnetically induced transparency
EMCCD	electron-multiplying CCD
EMM	excess micromotion
EOM	electro-optic modulator
FDA	frequency distribution amplifier
FFC	fiber frequency comb
FG	frequency generator
FPGA	field-programmable gate array
FS	fused silica
FSC	fiber splitter combiner
FWHM	full width at half-maximum
GL	glan laser
GT	glan taylor
GSC	ground state cooling
HC	Hänsch-Coulliaud
IMM	intrinsic micromotion
IR	infrared
LO	local oscillator
MCA	multi-channel analyzer
MBS	motorized beam sampler
MOPA	master oscillator power amplifier
NA	numerical aperture

<b>Acronym</b>	<b>Meaning</b>
NEG	non evaporative getter (pump)
NF	(spectral) notch filter
NIST	National Institute of Standards and Technology (national metrology institute of the United States)
NPL	National Physical Laboratory (national metrology institute of the UK)
o	ordinary
PBS	polarizing beam splitter
PCI	Peripheral Component Interconnect
PD	photodiode
PDET	phase detector
PDH	Pound-Drever-Hall
PID	proportional differential integral controller
PL	pump light
PMT	photomultiplier tube
PSD	power spectral density
PTB	Physikalisch-Technische Bundesanstalt (national metrology institute of Germany)
PTFE	Polytetrafluoroethylene
QPN	quantum projection noise
rf	radio-frequency
RMS	root mean square
ROI	region of interest
RSB	red sideband transition
S	splitter
SBC	sideband cooling
SHG	second-harmonic generation
SNR	signal-to-noise ratio
SP	single-pass
SWRM	standing-wave-ratio-meter
TTL	Transistor-transistor logic
UV	ultraviolet
WLM	wavelength meter





# 1. Introduction

The ability to measure time using calendars and clocks contributed to the evolution of mankind to the world we live in today e.g. in the fields of agriculture, navigation, trade, and science. For millennia, clocks were basically mechanical devices such as water clocks, candle clocks, or pendulum clocks, while time was defined by astronomical observations. Until the middle of the 20<sup>th</sup> century the second was defined as the 86400<sup>th</sup> fraction of the mean solar day [Bureau International des Poids et Mesures, 2006]. In the early 20<sup>th</sup> century, electronic quartz oscillator clocks were invented and surpassed the accuracy and stability of their mechanical counterparts due to their smaller sensitivity to environmental perturbations. In 1960, the second was defined more precisely based on the tropical year 1900 [Conference Generale des Poids et Mesures, 1961].

In 1967, more than one decade after the invention of the *microwave atomic clock* [Essen and Parry, 1955] the definition of the second was changed from celestial quantities to a fundamental natural reference: "The second is the duration of 9,192,631,770 periods of the radiation corresponding to the transition between the two hyperfine levels of the ground state of the caesium 133 atom." [Terrien, 1968]. This definition can be realized with much higher accuracy and has the fundamental advantage of the practically unlimited availability of caesium (Cs) 133 atoms, which are per definition identical and therefore interchangeable. Since then, the systematic fractional frequency uncertainty of Cs clocks was reduced to the low  $10^{-16}$  range in recent fountain clocks [Guená et al., 2017].

With the invention of the laser, optical transitions in atoms became accessible and therefore available as reference, which led to the development of *optical atomic clocks*. While the linewidths of microwave and optical clocks are comparable, the latter feature up to five orders of magnitude higher transition frequencies which result in substantially lower absolute fractional frequency uncertainties, given a sufficiently stable and narrow clock laser. Thanks to these prerequisites, optical clocks surpassed the best microwave clocks by achieving estimated systematic fractional frequency

## 1. Introduction

uncertainties of a few  $10^{-18}$  [Huntemann et al., 2016, Chou et al., 2010a, Nicholson et al., 2015, Ushijima et al., 2015]. This unprecedented performance might lead to a future redefinition of the SI-second [Gill, 2011, Riehle, 2015] and takes the search for a variation of fundamental constants on a new level [Godun et al., 2014, Huntemann et al., 2014, Safronova et al., 2018]. Optical clocks can also serve as quantum sensors for novel applications such as *chronometric leveling*. This approach for height measurements relative to the geoid was presented more than 30 years ago by [Vermeer, 1983] and [Bjerhammar, 1985]: due to the relativistic redshift derived from the theory of general relativity developed by [Einstein, 1916], two stationary clocks of the same type run at different frequencies, when they are operated at non-identical geopotentials. Therefore, the difference in geopotential and thereby height referred to the geoid can be derived from clock frequency comparisons [Müller et al., 2018, Mehlstäubler et al., 2018]. [Chou et al., 2010b] demonstrated this technique experimentally by lifting one of two optical clocks by 33 cm between subsequent side-by-side frequency comparisons, observing a relative frequency shift of  $(4.1 \pm 1.6) \times 10^{-17}$ .

Chronometric leveling is a particularly interesting technique for height difference measurements between locations that are not connected by a direct line of sight, e.g. between different continents or between off-shore islands and the mainland. For chronometric leveling at such sites, a transportable optical clock is required, which is calibrated to a reference clock before it is operated at the point of interest and compared to the same reference clock again via phase-stabilized optical fiber links [Lisdat et al., 2016, Raupach et al., 2015, Riehle, 2017, Lee et al., 2017] or via a satellite link [Fujieda et al., 2018].

Recently, a few transportable optical clocks have been presented by various groups. A transportable optical single  $^{40}\text{Ca}^+$  clock has been reported to reach a systematic fractional frequency uncertainty of  $7.8 \times 10^{-17}$  in a system occupying a volume of less than  $1 \text{ m}^3$  [Cao et al., 2017]. Moreover, a  $^{87}\text{Sr}$  optical lattice clock with an estimated systematic fractional frequency uncertainty of  $7 \times 10^{-17}$  [Koller et al., 2017] has been installed inside a car trailer and employed in the first measurement campaign involving a transportable optical clock to determine the gravitational red shift between the Modane underground laboratory in the Alps and stationary clocks at INRIM (Turin) [Grotti et al., 2018]. However, clocks with  $1 \times 10^{-18}$  systematic fractional frequency uncertainty (cf. 2.1.2) are needed to reach 1 cm height resolution [Vermeer, 1983]. Satellite-borne gravimetry measurements as performed in the scope

of the GRACE [National Aeronautics and Space Administration, 2018] and GOCE [European Space Agency, 2018] space mission already achieve 1 cm geoid height resolution, but only for lateral resolutions of a few hundred km [Reigber et al., 2005, Drinkwater et al., 2003]. Therefore, atomic clocks with  $1 \times 10^{-18}$  systematic fractional frequency uncertainty could be employed to add significant details to geoid maps calculated from satellite measurements [Bondarescu et al., 2012], since the lateral resolution of chronometric leveling measurements is below 1 m.

Of all realized optical frequency references, aluminum ( $^{27}\text{Al}^+$ ) has one of the smallest black-body radiation shifts [Rosenband et al., 2006, Safronova et al., 2011]. Therefore, the thermal environment of the clock ion needs to be known to only 18.2 K at room temperature [Dolezal et al., 2015] to reach  $10^{-18}$  systematic uncertainty of this shift. Additionally,  $\text{Al}^+$  has only small linear and quadratic Zeeman shifts [Rosenband et al., 2007] and a negligible quadrupole shift [Beloy et al., 2017]. Instead, due to its low mass the error budget can be dominated by the trap-related second order Doppler shifts from secular and micromotion or the shift due to collisions with background gas particles.

In summary, geodetic applications require height measurements with 1 cm resolution that can be performed anywhere on earth. Chronometric leveling by comparing two optical clocks to yield the gravitational redshift and therefore the difference in geopotential at the location of the clock ions is a promising approach which has been demonstrated in the field.

This thesis reports on the development and characterization of a setup for the first transportable single  $^{27}\text{Al}^+$  ion quantum logic optical clock. Employing a single  $^{40}\text{Ca}^+$  ion for its characterization, a partial error budget for the  $^{27}\text{Al}^+$  ion clock is derived resulting in an estimated systematic fractional frequency uncertainty of  $1.7 \times 10^{-18}$ .

The thesis is structured as follows:

- Chapter 2 reviews the concepts of optical clocks, ion trapping in linear Paul traps and atom light interaction of trapped ions. The level schemes of the clock and logic ion are introduced. The chapter concludes with a summary of quantum logic spectroscopy.
- Chapter 3 presents the experimental setup of the transportable  $^{27}\text{Al}^+$  ion optical clock in detail and provides the characterization results of selected components, especially of the imaging system and on the setup for loading via pulsed

## 1. Introduction

laser ablation and subsequent photoionization.

- Chapter 4 reports on the ground state cooling performance using pulsed side-band cooling and excess micromotion compensation results employing a single  $^{40}\text{Ca}^+$  as a probe. Afterwards, a partial error budget for an  $^{27}\text{Al}^+$  clock in this setup is estimated.
- Chapter 5 describes the  $^{27}\text{Al}^+$  logic laser system, focusing on the development and characterization of a highly stable enhancement cavity for second harmonic generation to the near and middle ultra-violet (UV). The system has been demonstrated to be suitable for transportable applications.
- Chapter 6 provides a summary of the results of the thesis and gives an outlook on the remaining steps towards a fully operational transportable  $^{27}\text{Al}^+ / ^{40}\text{Ca}^+$  quantum logic optical clock that facilitates chronometric leveling in the field and side-by-side comparisons to various stationary clocks at different sites.





## 2. Foundations and theoretical background

The implementation of chronometric leveling requires optical clocks to reach a sufficient height resolution for applications in research and applied technology. Optical clocks are based on laser spectroscopy of atoms that are required to be fixed in space and isolated from environmental perturbations which can cause frequency shifts of the relevant atomic lines.

This chapter starts with a discussion of the fundamental concept of optical clocks, followed by the explanation of their key properties. Afterwards, the concept of ion confinement in Paul traps is explained. The next part describes atom light interaction of trapped ions which is required for cooling, state detection, and manipulation using laser beams. Afterwards, the level schemes of  $^{27}\text{Al}^+$  and  $^{40}\text{Ca}^+$ , the building blocks of the aluminum ion quantum logic optical clock, are presented. The chapter ends with a summary of the quantum logic spectroscopy technique, which is required for clock state detection in state of the art  $^{27}\text{Al}^+$  clocks.

### 2.1. Optical clocks

#### 2.1.1. Concept of optical ion clocks

This subsection introduces the concept of optical clocks. A comprehensive overview of the topic is given e.g. in the review article by [Ludlow et al., 2015].

In Fig. 2.1 the principal constituents of a single ion optical clock are depicted. A *clock ion* is confined in an ion trap mounted inside a vacuum chamber. The ion features an internal electronic energy level structure that is per definition identical for all ions of the same isotope. Therefore, the spacing between two of these levels is a natural choice as reference for a clock, since the undisturbed transition frequency is the same for all ions of that isotope. However, the exact transition frequency is not

## 2. Foundations and theoretical background

only given by the level structure, but also by the shifts caused by perturbing electric and magnetic fields, relativistic effects, and background gas particle collisions, as will be discussed in Sec. 4.3.

The *clock transition* is interrogated by applying a frequency stable narrow linewidth *clock laser*, trying to excite the clock ion. Afterwards, the electronic state of the ion is determined e.g. by *electron shelving detection* proposed by [Dehmelt, 1973]. Since a single measurement of the state yields a binary result, it is typically repeated tens of times to obtain the excitation probability. Then, a feedback is applied on the clock laser to stabilize its frequency on the clock transition, i.e. to adjust it such that the excitation probability of the clock transition is maximized<sup>1</sup>.

Typical clock transitions and also clock laser linewidths are below 1 Hz, while the frequency drift of a free running laser can reach  $1 \text{ MHz s}^{-1}$ , and interrogation times of seconds are desirable. Therefore, the feedback from the ion is too slow to stabilize the clock laser directly on the atomic line. Instead, the clock laser is prestabilized to a resonance of an ultrastable reference cavity [Kessler et al., 2012, Häfner et al., 2015, Amairi, 2014]. The latter is composed of two mirrors which are attached to the ends of an usually several 10 cm long spacer made of ultra low thermal expansion material which is temperature stabilized, kept under vacuum, and shielded against vibrations. By stabilizing the clock laser frequency to a resonance of that cavity the length stability of the cavity can be transferred to the frequency stability of the clock laser. This *prestabilization* provides feedback on short timescales. On longer timescales the clock laser frequency is stabilized on the clock transition.

The setup described up to here provides a stable clock laser frequency and is therefore referred to as *optical frequency standard*. A fraction of the clock light is sent to a beat with an optical frequency comb, i.e. a mode-locked pulsed laser generating a ruler of evenly spaced "teeth" in frequency space [Hall, 2006, Hänsch, 2006]. The result of the beat is an electrical signal in the radio frequency (rf) regime whose periods are counted electronically and therefore provide time information, i.e. the number of cycles from a chosen starting time, forming a *clock*.

---

<sup>1</sup>In practice, the laser is often stabilized on either side of the fringe where the slope of the error signal is maximal and the direction of frequency deviation unambiguous.



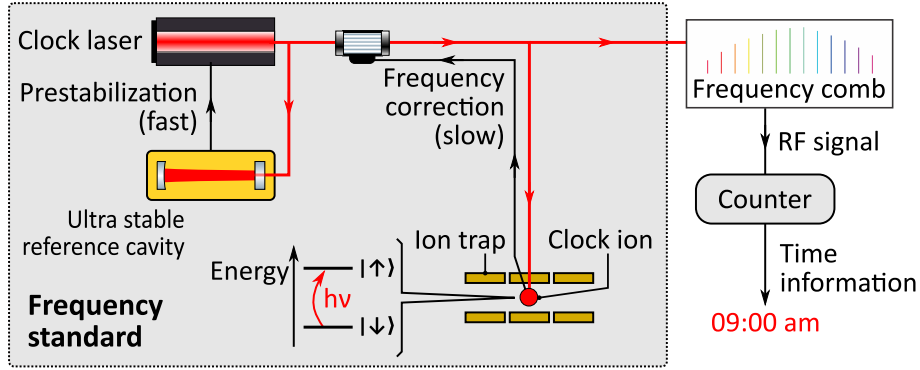


Figure 2.1.: Schematic functional principle of an optical clock, not to scale. A laser that is prestabilized to an ultra stable optical reference cavity interrogates the clock transition between internal energy levels of the clock ion. From the obtained result a correction signal is generated and fed back on the laser frequency, forming a frequency standard. By converting the clock laser frequency to the radio frequency (rf) regime and counting the cycles a clock is obtained. Some components in the figure are adapted from [Franzen, 2009].

### 2.1.2. Optical clocks: figures of merit

Frequency standards and therefore clocks are usually characterized by two figures of merit: *systematic fractional frequency uncertainty* and *statistic fractional frequency uncertainty*. In Fig. 2.2 both are depicted similar to [Riehle, 2004] for the results of a dart game (first row) and for frequency measurements (second row). Statistic fractional frequency uncertainty is the property that describes by how much subsequent measurements differ from each other, e.g. the dart results and frequency measurements depicted in column (2) are more stable than in (1). Stability is usually quantified using the *Allan variance* [Allan, 1966]:

$$\sigma_y^2(\tau) = \frac{1}{2} \langle (\bar{y}_2 - \bar{y}_1)^2 \rangle, \quad (2.1)$$

where the angled brackets denote the mean value of the difference of two subsequent frequency measurement results  $\bar{y}_i$ , which are both averaged over the duration  $\tau$ . A more extensive treatment of the topic can be found in textbooks such as [Riehle, 2004].

The statistic fractional frequency uncertainty achievable with an atomic clock is fundamentally limited by the fact that every single interrogation yields only one

## 2. Foundations and theoretical background

byte of information by projecting the internal state of the clock ion on one of the two eigenstates  $|\uparrow\rangle$  or  $|\downarrow\rangle$ . Therefore, the error of multiple measurements  $\sigma_{\text{QPN}}$  follows the binomial distribution. It is termed *quantum projection noise* (QPN) and is described by [Itano et al., 1993]:

$$\sigma_{\text{QPN}} = \frac{1}{\kappa} \frac{\Delta\nu}{\nu} \frac{1}{\sqrt{N}} \sqrt{\frac{t}{T}}, \quad (2.2)$$

where  $\kappa$  is a numerical factor of order unity that depends on the interrogation scheme,  $\Delta\nu$  the FWHM of the clock line,  $\nu$  the clock transition frequency,  $N$  the number of atoms interrogated,  $T$  the total measurement time, and  $t$  the duration of a single interrogation. It is worth noting that this limit only applies in absence of collective effects and can be overcome by a factor of up to  $\sqrt{N}$  via entanglement of the clock ions as proposed by [Wineland et al., 1992].

The second figure of merit is sometimes called the systematic fractional frequency uncertainty which is the accuracy of the clock, i.e. the deviation of the mean measured frequency value from the idealized undisturbed transition. Therefore, the results depicted in Fig. 2.2 (3) and (4) are more accurate than those in (1) and (2), but only (4) is accurate and stable at the same time.

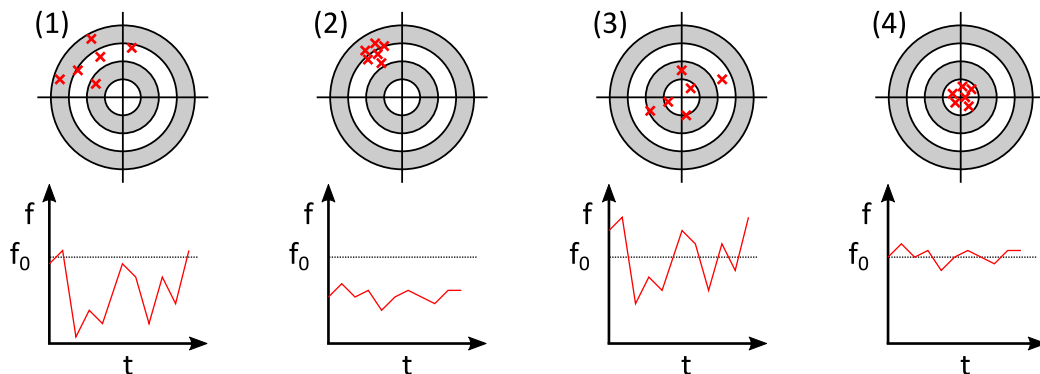


Figure 2.2.: Graphical representation of frequency accuracy and stability. First row: results of a dart game as instructive example. Second line: depicted course of frequency measurements compared to the frequency of the undisturbed transition  $f_0$ . From left to right: inaccurate and instable (1), inaccurate but stable (2), accurate but instable (3), accurate and stable (4).

Frequency inaccuracies are caused by shifts due to perturbing electric and magnetic fields, relativistic effects and background gas collisions, cf. Sec. 4.3. However, known shifts can be accounted in the evaluation of clock comparisons and chro-

nometric leveling campaigns. Therefore, the clock performance is in the end not limited by the inaccuracy due to known frequency shifts, but due to the errors of these shifts. The estimation of those errors results in the reported systematic fractional frequency uncertainty of the clock.

## 2.2. Ion trapping in linear Paul traps

This section sums up the key concepts of classical ion trapping in rf traps, provided by textbooks such as [Ghosh, 1995] or [Major et al., 2005], to which the reader is referred for a more extensive treatment of the topic.

Since an ion is an electrically charged particle, the obvious naive way to achieve stable confinement is a static 3d parabolic potential

$$\Phi_1(x, y, z) = U_1 (c_x x^2 + c_y y^2 + c_z z^2), \quad (2.3)$$

with the positive real prefactor  $U_1$  and the three non-zero real coefficients  $c_i$ . The volume around the ion is charge free, therefore the Laplace equation

$$\Delta\Phi = 0 \quad (2.4)$$

has to be fulfilled, which is only achievable if at least one of the  $c_i$  is negative. In conclusion it is not possible to confine an ion in 3 dimensions in a purely static potential.

Therefore, ion traps based on a combination of alternating current (ac) and direct current (dc) electric potentials have been invented [Paul et al., 1958, Dehmelt, 1968], including the linear Paul trap [Paul, 1990], which has been employed for the experiments presented in this thesis. Fig. 2.3(a) shows one possible implementation of a Paul trap (left): four parallel metal rods are mounted in a square configuration. A rf potential is applied to a pair of opposing rods (blue). The other two rods (red) are segmented, connected to dc potentials, and serving as rf ground. This configuration leads to an electric ac quadrupole field in the central plain perpendicular to the rods, cf. Fig. 2.3(b), which traps the ion in center. Confinement along the trap axis is achieved by applying positive dc potentials to the rod segments on both sides of the central segment, cf. Fig. 2.3(c). Since one of the rod pairs is on a dc potential and the other on ac, this configuration is referred to as *asymmetric drive*. It is simpler to implement than a *symmetric drive*, but has the drawback of a not

## 2. Foundations and theoretical background

fully vanishing ac field on the trap axis, except for a single point.

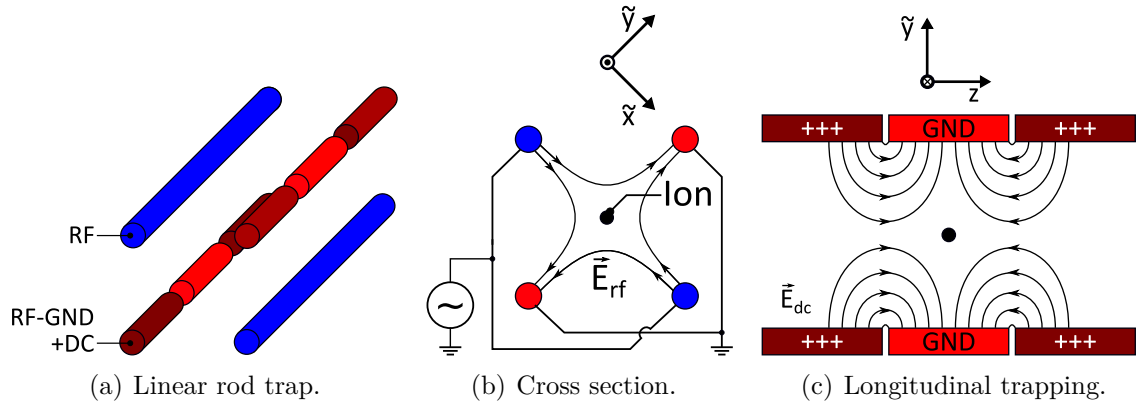


Figure 2.3.: Linear Paul trap with asymmetric rf drive. Four parallel rods (a) generate an electric rf quadrupole field (black lines, b) for the radial confinement of the ion. Axial trapping is achieved by applying positive potentials to the ends of the dc-rods (c).

In the coordinate system of the trap spanned by  $(\tilde{x}, \tilde{y}, z)$ , the potential becomes

$$\Phi_I(\tilde{x}, \tilde{y}, z) = U_{\text{end}} \frac{1}{2} (c_x \tilde{x}^2 + c_y \tilde{y}^2 + c_z z^2) + U_{\text{rf}} \cos(\Omega_{\text{rf}} t) \frac{1}{2} (c_x \tilde{x}^2 + c_y \tilde{y}^2 + c_z z^2), \quad (2.5)$$

with the rf-drive frequency  $\Omega_{\text{rf}}$ , rf amplitude  $U_{\text{rf}}$ , and the real coefficients

$$-(c_x + c_y) = c_z > 0 \quad (2.6)$$

$$\tilde{c}_x = -\tilde{c}_y. \quad (2.7)$$

In one dimension, the classical equation of motion, is given by:

$$\ddot{\tilde{x}} = -\frac{Z|e|}{m} \frac{\partial \Phi}{\partial \tilde{x}}, \quad (2.8)$$

with the charge number  $Z$ , the elementary charge  $e$ , and the ion mass  $m$ . It is then transformed to the standard form of the Mathieu differential equations

$$\frac{d^2 \tilde{x}}{d\xi^2} + (a_x - 2q_x \cos(2\xi)) \tilde{x} = 0 \quad (2.9)$$

with the substitutions

$$\xi = \frac{\Omega_{\text{rf}} t}{2}; \quad a_x = \frac{4Z|e|U_{\text{end}}c_x}{m\Omega_{\text{rf}}^2}; \quad q_x = \frac{2Z|e|U_{\text{rf}}\tilde{c}_x}{m\Omega_{\text{rf}}^2}. \quad (2.10)$$

The entire trap geometry is included in the parameters  $c_x$  and  $\tilde{c}_x$ . The Mathieu differential equations have stable solutions only in specific stability regions, which are presented in standard textbooks on ion trapping. Most ion traps are operated in the regime  $a_i, q_i \ll 0$ .

While the axial ion confinement in the parabolic dc potential is conceptually simple, an intuitive understanding of the radial trapping mechanism is provided by Fig. 2.4. Fig. 2.4(b) shows the radial potential for a fixed time  $t_0$ . Due to its saddle shape, an ion would experience a force towards the trap center in x-direction, but away from it in y-direction. In (b), only the potential along the x-direction is depicted. During every cycle of the rf potential, a net reduction of the ion-to-trap center distance is achieved and the effect of the real ac potential can be described by a dc pseudopotential, depicted in (c).

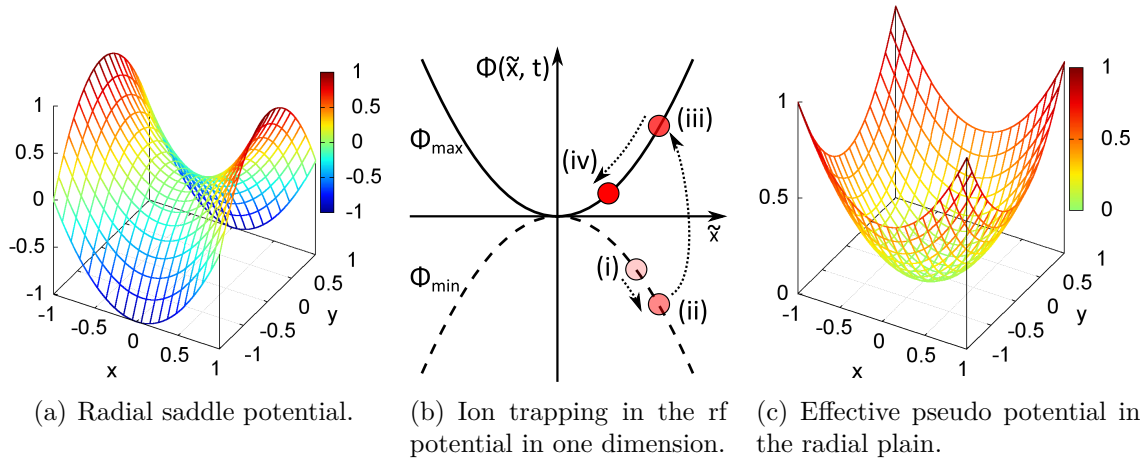


Figure 2.4.: Ion trap potentials, schematically, in arbitrary units. The potential in the xy-plane at a given time has a saddle form (a.). Depicted in (b.) are the maximum and minimum potentials  $\Phi_{\text{max}}$  and  $\Phi_{\text{min}}$  for one radial direction. The ion-to-trap center distance is reduced during one cycle of the rf potential: (i) to (iv). The time-averaged result is an effective pseudo potential (c.).

## 2. Foundations and theoretical background

The lowest order classical solution to equation of motion in one dimension  $\tilde{x}$  is

$$\tilde{x}(t) \approx \underbrace{2AC_0 \cos\left(\beta_{\tilde{x}} \frac{\Omega_{\text{rf}}}{2} t\right)}_{\text{secular motion}} \left[ 1 - \underbrace{\frac{q_{\tilde{x}}}{2} \cos(\Omega_{\text{rf}} t)}_{\text{micromotion}} \right] \quad \text{with} \quad \beta_x \approx \sqrt{a_{\tilde{x}} + q_{\tilde{x}}^2/2}, \quad (2.11)$$

composed of a slow, *secular motion* that can be reduced by laser-cooling as explained in Sec. 4.1, and a faster *micromotion* that is driven by the rf potential and cannot be cooled efficiently. Its amplitude depends on the position of the ion with respect to potential. Moreover, due to the finite spread of the ion's wave packet in the motional ground state  $x_0 = \sqrt{\hbar/2m\omega_x}$  an *intrinsic micromotion* (IMM) is unavoidable.

For one singly charged ion confined in a linear Paul trap, the secular motional frequency in axial direction is

$$\omega_{\text{ax}} = \frac{\Omega_{\text{rf}}}{2} \sqrt{a_z} = \sqrt{\frac{2\kappa e U_{\text{end}}}{m z_0^2}}, \quad (2.12)$$

where  $\kappa$  is a geometry factor between 0 and 1,  $e$  the elementary charge,  $U_{\text{end}}$  the electric potential applied to the neighboring trap electrodes in axial direction and  $z_0$  the distance from the trap center to the axially confining electrodes.

The secular motion frequencies in radial direction are

$$\omega_{\text{rad},\tilde{x}/\tilde{y}} = \frac{\Omega_{\text{rf}}}{2} \sqrt{\pm a_{\tilde{x}} + \frac{q_{\tilde{x}}^2}{2}} = \sqrt{\mp \frac{\kappa e U_{\text{end}}}{m z_0^2} + \frac{1}{2} \left( \frac{e U_{\text{rf}}}{m r_0^2} \right)^2}, \quad (2.13)$$

with the rf amplitude  $U_{\text{rf}}$  and the ion-to-electrode distance  $r_0$ .

When  $N$  ions are loaded into a stable Paul trap and sufficiently cooled, these form an ion crystal. For every direction the ion motion can be composed of  $n$  Eigenmodes. In case of a two ion crystal, these are the center of mass or in-phase (IP) mode, where both ions move in the same direction for any given point of time, and the stretch or out-of-phase (OOP) mode, where both ions always move in opposing directions. For different ion masses  $m_1$  and  $m_2$  with the ratio  $\mu = m_2/m_1$ , the corresponding secular frequencies in the axial direction are [Wübbena, 2014]:

$$\omega_{\text{ax,IP/OOP}} = \sqrt{\frac{1 + \mu \mp \sqrt{1 - \mu + \mu^2}}{\mu}} \omega_{\text{ax}}. \quad (2.14)$$

It is worth noting that the ratio of the IP and OOP frequencies is related to the

ratio of the ion masses:

$$\frac{\omega_{\text{ax,IP}}}{\omega_{\text{ax,OOP}}} = \sqrt{\frac{1 + \mu - \sqrt{1 - \mu + \mu^2}}{1 + \mu + \sqrt{1 - \mu + \mu^2}}} \quad (2.15)$$

$$\approx 0.56 \quad \text{for } {}^{27}\text{Al}^+ / {}^{40}\text{Ca}^+. \quad (2.16)$$

Therefore, if a single ion of a known mass is loaded into a perfectly harmonic ion trap with fixed confinement strength, the mass of a co-trapped ion can be determined by measurement of two secular frequencies.

Lastly, the separation  $s_2$  of two singly charged ions forming a crystal oriented along the trap axis is [Wineland et al., 1998]

$$s_2 = \left( \frac{e^2}{2\pi\epsilon_0 m \omega_{\text{ax}}^2} \right)^{1/3} = \left( \frac{e z_0^2}{4\pi\epsilon_0 \kappa U_{\text{end}}} \right)^{1/3}, \quad (2.17)$$

i.e. it is independent of the confined species. Typical values are on the order of a few  $\mu\text{m}$ .

## 2.3. Light interaction of a trapped ion

Up to here, the ion inside the trap has been treated as classical point particle. However, an ion confined in a trap is an ideal system for the observation of quantum properties such as discrete energy levels and a spatial extent described by a wave function. Therefore, this subsection recaps the main features of the quantum mechanical harmonic oscillator and atom light interaction. For a more extensive introduction to the topic the reader is referred to textbooks such as [Cohen-Tannoudji, 2004] or [Knoop et al., 2015].

The one dimensional Hamilton operator for motion along the direction  $i$  in a harmonic potential is

$$\hat{H}_i = \hbar\omega_i \left( \hat{n}_i + \frac{1}{2} \right), \quad (2.18)$$

where  $\omega_i$  denotes the angular frequency of the motion and  $\hat{n}_i$  the number operator, i.e. the number of phonons in mode  $i$ . This corresponds to an equally spaced ladder of energy eigenstates as depicted in Fig. 2.5(a), where  $V$  denotes the harmonic potential and  $x$  the spatial extent of the wave function.

## 2. Foundations and theoretical background

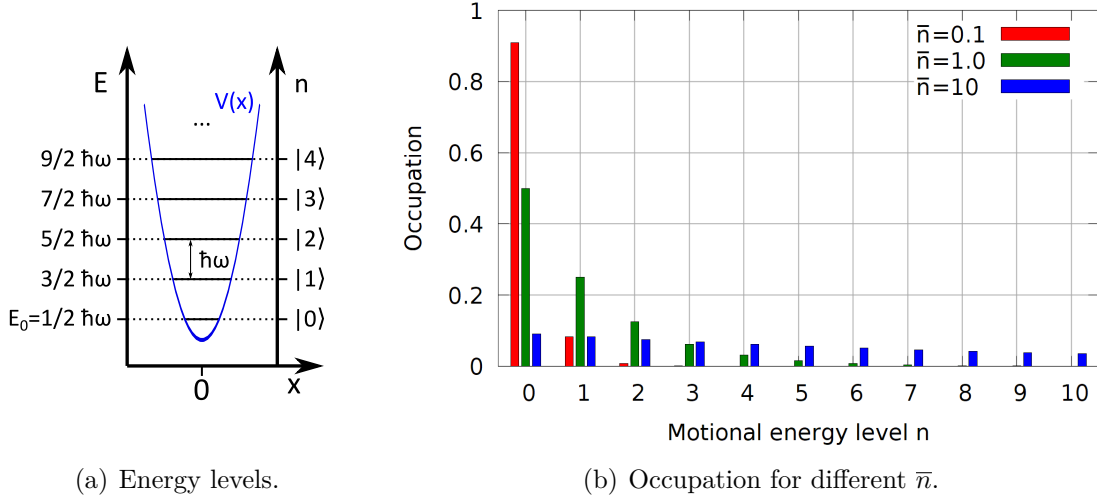


Figure 2.5.: (a): quantum harmonic oscillator energy levels. (b): occupation of number states for three different  $\bar{n}$ .

For a thermal state of temperature  $T$ , the occupation of the energy eigenstates  $|n\rangle$  with phonon number  $n$  follows the Boltzmann distribution. The average motional quantum number  $\bar{n}$  is

$$\bar{n} = \frac{1}{e^{\hbar\omega/k_B T} - 1} \quad (2.19)$$

and the occupation probability  $p_n$  of the energy level  $|n\rangle$  is

$$p_n(\bar{n}) = \frac{\bar{n}^n}{(\bar{n} + 1)^{(n+1)}}, \quad (2.20)$$

which is shown for different average motional quantum numbers in Fig. 2.5(b).

Besides the kinetic energy eigenstates, an ion also has internal eigenstates, in case of a two level system these are the ground state  $|\downarrow\rangle$  and the excited state  $|\uparrow\rangle$ , which are separated by an energy difference  $\Delta E = \hbar\omega_0$ .

The bare internal Hamiltonian for a two level system is:

$$\hat{H}_{\text{ion}} = \frac{\hbar\omega_0}{2} \hat{\sigma}_z, \quad (2.21)$$

with the Pauli spin matrix  $\hat{\sigma}_z$ .

The interaction of the free ion with a monochromatic coherent light field detuned by a small  $\delta$  from the resonance frequency  $\omega_0$  is in the interaction picture after



rotating wave approximation given by:

$$\hat{H}_{\text{int}} = \frac{\hbar\Omega}{2} \left( e^{-i\delta t} \hat{\sigma}_+ + e^{i\delta t} \hat{\sigma}_- \right), \quad (2.22)$$

where  $\hat{\sigma}_{\pm}$  are the internal raising and lowering operators build from linear combinations of Pauli spin matrices.  $\Omega$  is the *Rabi frequency*, i.e. the frequency of the population oscillations between the states  $|\downarrow\rangle$  and  $|\uparrow\rangle$ , which is a measure for the coupling strength between the light field and the internal levels. For optical dipole transitions, it is proportional to the scalar product of the dipole element and the electric field:  $\Omega \propto \vec{d} \cdot \vec{E}$ .

For a confined ion the level structure is the direct product of the ladder of motional states and the internal structure. In case of the two level system considered here, this yields two displaced equally spaced ladders, as depicted in Fig. 2.6. In this case, the light field cannot only drive internal transitions while the motional quantum number is conserved (*carrier transitions*, CAR), but also so-called *sideband transitions*, where  $n$  changes. For the  $|\downarrow\rangle \rightarrow |\uparrow\rangle$  transition, red sideband (RSB) transitions reduce  $n$ , blue sideband (BSB) transitions increase motion. In the *Lamb-Dicke regime*, the spatial extent of the ion's wave function is much smaller than the wavelength of the cooling laser; the ratio is referred to as *Lamb-Dicke factor*  $\eta = \frac{x_0}{\lambda}$ . The coupling strengths of the different transitions in terms of Rabi frequency is [Wineland et al., 1998]

$$\Omega_{n,n+m} = \Omega e^{-\eta^2/2} \eta^{|m|} \sqrt{\frac{\min(n, n+m)!}{\max(n, n+m)!}} L_{\min(n, n+m)}^{|m|}(\eta^2), \quad (2.23)$$

where  $L$  denotes the generalized Laguerre polynomial. It is worth noting that the Rabi frequencies for the same order RSB and BSB transitions are different, which is employed for near ground state temperature measurements, cf. Sec. 4.1. In the regime  $\eta \ll 1$ , the trap absorbs the recoil energy of photons emitted by the ion and transitions that change the motional quantum number by more than 1 are strongly suppressed.

## 2. Foundations and theoretical background

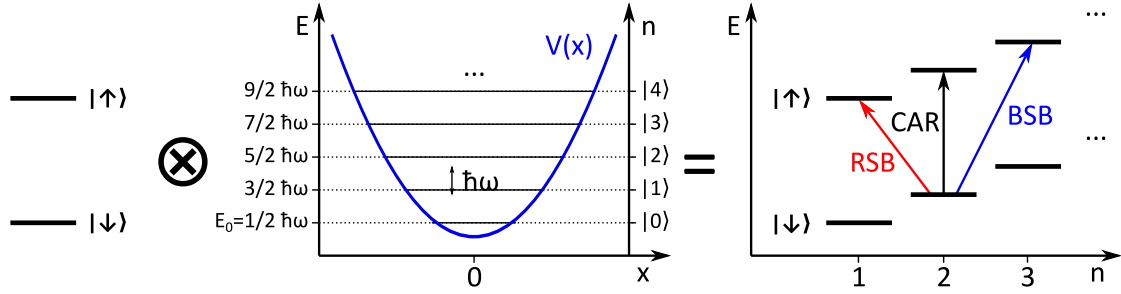


Figure 2.6.: Product states, not to scale. The internal structure of a free two level system (left) combined with the motional energy level structure of a 1d quantum harmonic oscillator (center) yields to product states (right). Transitions with  $\Delta n = -1$  (+1) are called red (blue) sideband transitions (RSB/BSB),  $\Delta n = -0$  carrier transition (CAR).

## 2.4. The clock ion

Major parts of the content of this and the following section are presented in a publication by the author of this thesis [Hannig et al., 2018b]. For simplicity, individual citations in the main text are omitted.

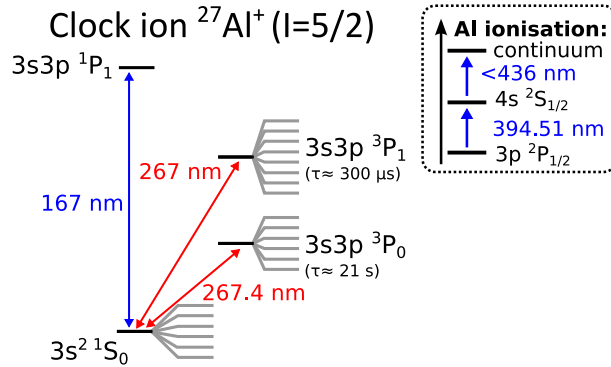


Figure 2.7.: Reduced  $^{27}\text{Al}^+$  level scheme, not to scale. Grey lines depict the Zeeman splitting of the levels when an external dc magnetic field is applied. From [Hannig et al., 2018b].

Fig. 2.7 shows the reduced level scheme of  $^{27}\text{Al}^+$  and one possible two-step photoionization path for neutral Al in the insert. Aluminum provides a 8 mHz narrow clock transition at 267.4 nm connecting the  $^1\text{S}_0$  ground state to the  $(20.6 \pm 1.4)$  s long lived [Rosenband et al., 2007]  $^3\text{P}_0$  level and a transition at 266.9 nm [Kramida et al., 2018] connecting the  $^1\text{S}_0$  ground state to  $^3\text{P}_1$  suitable for state preparation and quantum logic state transfer. However, direct laser cooling of aluminum would require 167 nm light [Kramida et al., 2018]. The required  $\text{KBe}_2\text{BO}_3\text{F}_2$  (KBBF) crystals

[Chen et al., 2009] for frequency doubling to that wavelength are to the knowledge of the author not commercially available on the world market. Due to the strong absorption of 167 nm light in air, the entire 167 nm beam path would be required to be in vacuum. These challenges can be circumvented by sympathetically cooling [Larson et al., 1986, Barrett et al., 2003] the clock ion with an ion of another species and using quantum logic spectroscopy [Schmidt et al., 2005] to transfer the internal state of the clock ion to the logic ion via a shared motional mode, as explained in Sec. 2.6. The logic ion needs to provide accessible closed transitions for Doppler cooling and electron shelving detection [Dehmelt, 1973]. Furthermore, a mass ratio of the species close to 1 enables fast cooling [Wübbena et al., 2012].

## 2.5. The logic ion

Fig. 2.8 shows the reduced level scheme for  $^{40}\text{Ca}^+$  and the later employed two-step photoionization path for neutral Al in the insert. This species is an advantageous choice as logic ion especially for a transportable clock, since all required wavelengths can be generated in compact and reliable diode lasers and guided in commercially available optical fibers, which allow for a modular setup. Moreover, quantum logic operations on  $^{40}\text{Ca}^+$  are very well developed through its use in quantum information processing, while its mass ratio with  $^{27}\text{Al}^+$  allows efficient sympathetic cooling. However, also  $^{27}\text{Al}^+$  clocks with  $\text{Mg}^+$  or  $\text{Be}^+$  as logic ion have been demonstrated. While the mass ratio of  $\text{Al}^+/\text{Mg}^+$  is close to 1 and therefore enables high cooling rates, its broad Doppler cooling linewidth leads to either a larger second order Doppler shift or longer GSC times. The cooling transition in the UV results in a lower detection efficiency than for  $^{40}\text{Ca}^+$  [Hemmerling et al., 2012] and requires custom optical fibers.  $\text{Be}^+$  as logic ion shares the challenges related to the UV transition and additionally provides comparatively inefficient cooling due to the small mass ratio of  $\text{Al}^+/\text{Be}^+$ .

For these reasons here and at other experiments [Guggemos, 2016, Cui et al., 2018]  $^{40}\text{Ca}^+$  has been chosen as the logic ion species. It provides a cooling transition at 396.847 nm [Wan et al., 2014] with a linewidth of 22.4 MHz. Since the upper  $^2\text{P}_{1/2}$  level decays with a branching ratio of 0.06435(7) [Ramm et al., 2013] to the metastable  $^2\text{D}_{3/2}$  level, a repumping laser at 866.214 nm [Kramida et al., 2018] is required to avoid population trapping. Electron shelving is implemented on the 136 mHz narrow quadrupole transition [Barton et al., 2000] at 729.147 nm

## 2. Foundations and theoretical background

[Kramida et al., 2018]. For sideband cooling, the upper  $^2D_{5/2}$  level is cleared out via a 854.209 nm laser [Kramida et al., 2018] that pumps to the 6.8 ns short lived  $^2P_{3/2}$  level which quickly decays to the ground state, effectively quenching the 729 nm transition, more details are provided in Sec. sec:sbcool.

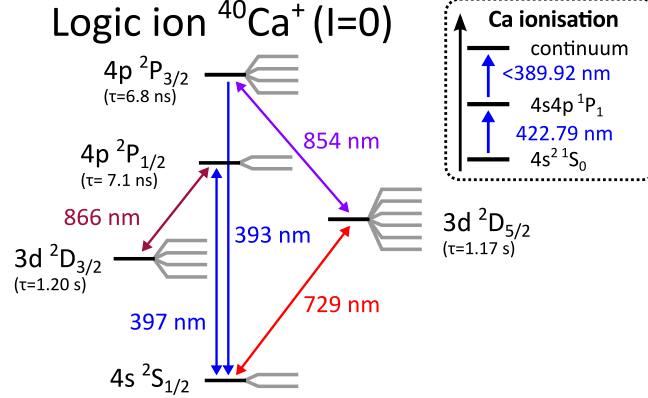


Figure 2.8.: Reduced  $^{40}\text{Ca}^+$  level scheme, not to scale. Grey lines depict the Zeeman splitting of the levels when an external dc magnetic field is applied. From [Hannig et al., 2018b].

## 2.6. Quantum logic spectroscopy

As discussed above,  $^{27}\text{Al}^+$  requires a logic ion for sympathetic cooling internal state readout. For the latter, the *quantum logic spectroscopy* (QLS) protocol has been invented and implemented by [Schmidt et al., 2005], which will be briefly recapped. Prior to the actual QLS sequence, all modes of the ion crystal are Doppler cooled. Then at least one of the modes is cooled to the motional ground state, cf. Sec. 4.1. Afterwards, the  $^{27}\text{Al}^+$  is pumped to one of the  $|S_0, m = \pm 5/2\rangle$  states by the circularly polarized  $^{27}\text{Al}^+$  logic laser.

The QLS sequence starts with both ions in the internal and motional ground state, as depicted in Fig. 2.9 (left). First, a CAR- $\pi$ -pulse is applied on the clock transition in (1), followed by RSB- $\pi$ -pulse on the  $^{27}\text{Al}^+$  clock transition (2), which maps the internal state of  $^{27}\text{Al}^+$  on the shared motional state of  $^{27}\text{Al}^+ / ^{40}\text{Ca}^+$ , i.e. the information whether  $^{27}\text{Al}^+$  was successfully excited by the clock laser in step (1), can now be inferred from the motional state of the logic ion by applying in a  $^{40}\text{Ca}^+$  RSB- $\pi$ -pulse (3) for electron shelving to the internal excited state of the  $^{40}\text{Ca}^+$  logic transition. In the end, the cooling lasers are applied (4) to determine the

internal state of  $^{40}\text{Ca}^+$  from the fluorescence signal and therewith whether  $^{27}\text{Al}^+$  was excited in step (1). The excitation probability required to stabilize the clock laser on the transition is determined by repeating the entire sequence on the order of 10 times. For locking on the line center, both slopes of the transition are interrogated alternately.

In summary, in QLS a shared motional mode is employed to map the internal state of the clock ion to that of the logic ion, which is read out via electron shelving detection.

To conclude, not only an  $^{27}\text{Al}^+$  clock laser is required to operate an  $^{27}\text{Al}^+$  clock, but also an  $^{27}\text{Al}^+$  logic laser for fast and efficient state preparation. Since the wavelengths are separated by 0.4 nm, two individual laser systems had to be built, as explained in Chap. 5.

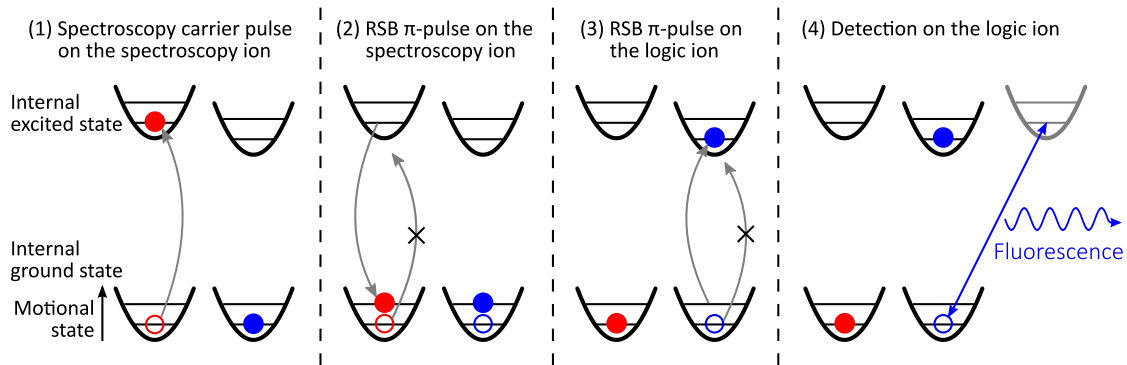


Figure 2.9.: Quantum logic spectroscopy sequence. The internal state of the spectroscopy ion (red) is transferred to the internal state of the logic ion (blue) via a shared motional mode. Adapted by kind permission of N. Scharnhorst.



# 3. Transportable aluminum optical clock setup

The previous chapter provided the theoretical basis of the  $^{27}\text{Al}^+ / ^{40}\text{Ca}^+$  optical clock. In this Chapter the setup used to perform experiments will be presented in detail. Its main constituent parts are the vacuum system including the ion trap, the laser system and the electronic experiment control system. The ion trap is mounted in a vacuum chamber providing an environment of low background gas collision rate. The trap is electrically connected to a rf drive for radial ion confinement and dc control voltages for axial confinement and micromotion compensation. The laser system is required for ion ablation, photoionization, cooling, and coherent manipulation. Fluorescent light emitted by the  $^{40}\text{Ca}^+$  is collected with an imaging system. All aforementioned components are operated via the experimental control system composed of a FPGA system and two PCs.

*Parts of the content of this chapter are presented in a publication by the author of this thesis [Hannig et al., 2018b]. For simplicity, individual citations in the main text are omitted.*

## 3.1. Ion trap

The Al clock requires at least a  $^{27}\text{Al}^+ / ^{40}\text{Ca}^+$  two ion crystal, but multi-ion quantum logic optical clock schemes have already been proposed [Schulte et al., 2016]. Therefore, a linear Paul trap was chosen, since this geometry provides a nearly micromotion-free confinement for multiple ions along the trap axis. Important requirements for optical ion clocks are spectroscopy in the Lamb-Dicke regime, cooling to the motional ground state and low heating rates. In the Lamb-Dicke regime, the ion trap absorbs the recoil from scattered photons. The second is necessary to obtain a low second order Doppler shift, cf. Sec. 4.3, and the last reduces cooling requirements during interrogation and the Dick effect, an aliasing phenomenon causing low

### 3. Transportable aluminum optical clock setup

frequency noise [J. Dick, 1987]. Since so-called anomalous heating in ion traps scales inversely with the second to fourth power of the ion-to-electrode distance [Brownmatt et al., 2015], these requirements translate to a large distance. Additionally, a design with multiple trapping zones allows for the use of distinct loading and spectroscopy zones, which reduces the risk of micromotion caused by unisotropic deposition from the neutral atom beams used for loading. Moreover, the ion loading and the actual experiment can be carried out in different zones avoiding ion operation near patch charges possibly created in the loading zone during the loading procedure due to inhomogeneous coating of the adjacent electrodes with evaporated material.

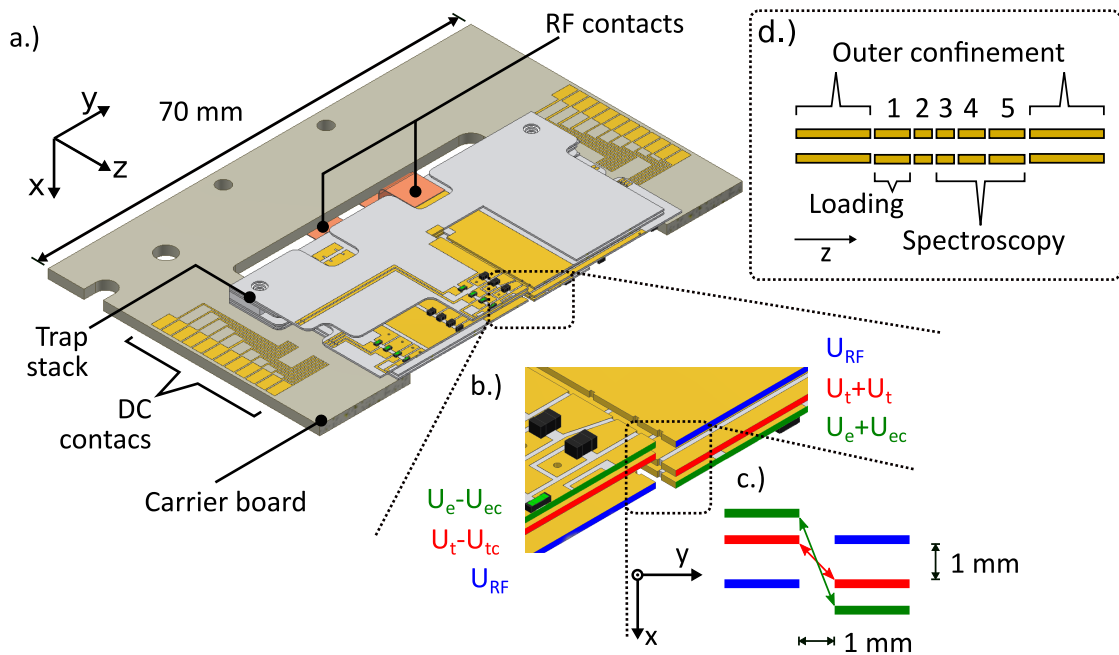


Figure 3.1.: Segmented multi-layer trap. a.) Half section of the trap. b.) Structure of the rf- and dc-electrodes in the radial ( $xy$ ) plane. c.) The voltage pairs  $U_{ec}$  and  $U_{tc}$  act in different directions and therefore allow for radial micromotion compensation. Insert d.) Electrode structure along the trap axis ( $z$ ).

Here, a segmented multilayer linear Paul trap of the design described by [Herschbach et al., 2012] was chosen, which is depicted in Fig. 3.1 and has been known for its low excess micromotion [Pyka et al., 2014] and heating rates [Keller, 2015]. It is a multi layer multi zone trap based on precisely aligned stacked  $250\ \mu\text{m}$  thick Rogers<sup>TM</sup> printed circuit boards with  $35\ \mu\text{m}$  thick conductive tracks made of copper. The electrode structures are laser cut. All conductive structures are coated



with a NiPdAu plating, where a  $3\ \mu\text{m}$  to  $7\ \mu\text{m}$  thick nickel layer provides adhesion for a  $0.05\ \mu\text{m}$  to  $0.25\ \mu\text{m}$  thick palladium and  $300\ \text{nm}$  thick gold layer. The inner two layers of the trap stack feature the rf drive electrodes and one set of compensation electrodes that are also used for the axial dc confinement, cf. Fig. 2.3, while the outer layers provide the second set of electrodes required for 2D positioning of the dc electric field minimum in the radial plane. All dc electrode voltages are low-pass filtered directly on the trap boards by first order RC lowpasses<sup>1</sup> with a cutoff frequency of  $113\ \text{Hz}$ . Furthermore, one PT100 temperature sensor on each of the rf boards provides *in situ* trap temperature measurements during operation [Dolezal et al., 2015]. The experiment zones are  $1.0$ ,  $1.5$ , and  $2.0\ \text{mm}$  long, respectively. These different lengths allow for a compromise between the maximum achievable axial trap frequency for a given voltage and the homogeneity of the axial field [Herschbach et al., 2012]. Moreover, it is possible to trap multiple ion ensembles in different zones of the trap simultaneously, allowing e.g. for dead time-free interleaved interrogation of two ion clocks in a single trap or other multi-ensemble protocols in the future. Lastly, several small mirrors are mounted directly on the trap for future interferometric clock laser phase stabilization.

An ion trap has to be mechanically stable and requires a good heat conductance from the trap to the environment to reduce its temperature rise due to the uncertainty of the blackbody radiation shift caused by dielectric loss during operation. Fig. 3.2 shows the the trap assembly. The trap stack is glued<sup>2</sup> on a carrier board made of AlN, featuring high mechanical stability and heat conductivity. The board is held by ceramic feet that are mounted on a titanium base plate for the installation inside the vacuum chamber. To ensure a good heat conductance between these components, at their junctions  $100\ \mu\text{m}$  thick indium foil has been placed between them. All dc voltages are provided to the trap via  $0.25\ \text{mm}$  diameter Kapton<sup>®</sup> coated copper wires that are soldered to the carrier board. Wire bonds electrically connect the carrier board to the trap chips. The rf drive and ground electrodes are connected to flat oxygen-free (OFHC) copper stripes with a cross section of  $5.0 \times 0.1\ \text{mm}^2$  providing a relatively large surface and therefore a high rf conductivity via the skin effect [Lamb, 1884]. Lastly, the copper stripes also facilitate heat conductance from the trap to the environment.

The assembly process followed the instructions given by [Pyka et al., 2014].

<sup>1</sup>Resistors:  $300\ \text{k}\Omega$ , Barry Industries RP0402BA-3003JN-91; capacitors:  $4.7\ \text{nF}$ , Novacap 0402 C472 J500 PH-HB.

<sup>2</sup>Optocast 3410 Gen2 UV curable epoxy.

### 3. Transportable aluminum optical clock setup

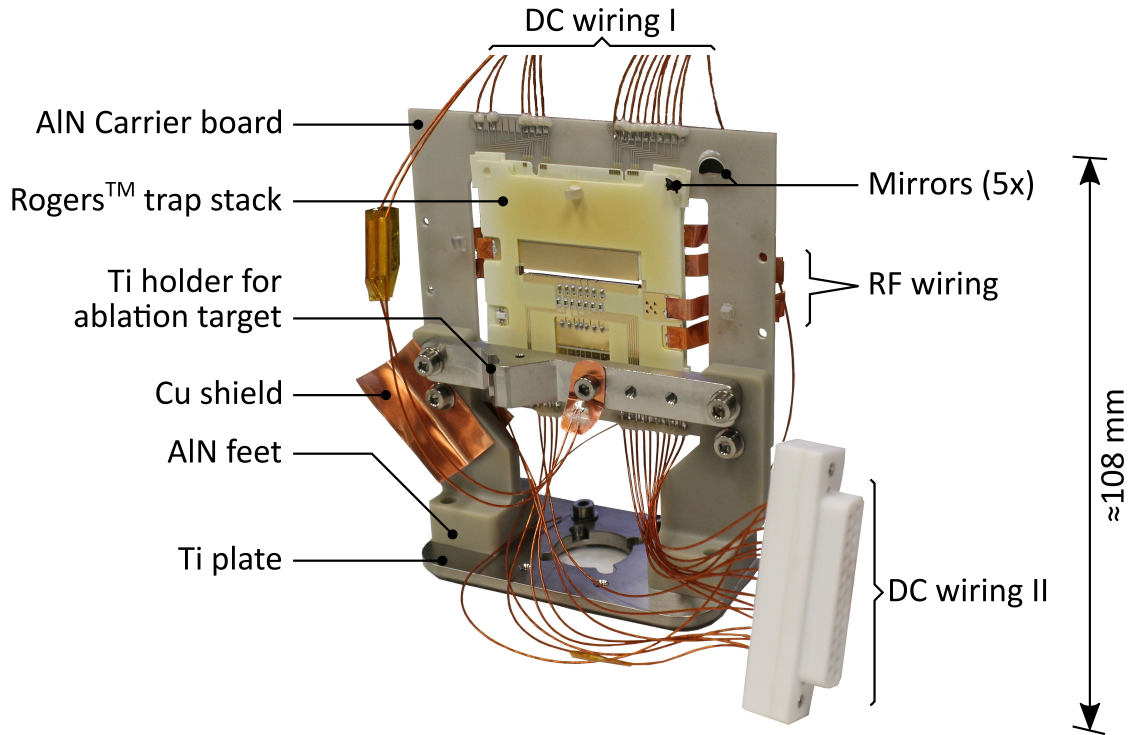


Figure 3.2.: Photo of the trap assembly. The trap stack is glued on top of a carrier board which is attached to ceramic feet that are mounted on a baseplate for installation inside the vacuum chamber. All mounting parts are made of AlN or Ti which are rigid, vacuum-compatible, and provide a good heat conductivity. A Cu shield below the trap stack blocks the direct line of sight between the trap center and the vacuum pump (cf. Sec. 3.4).

## 3.2. RF drive source

In Sec. 2.2 has been explained that a rf potential of up to 1 kV amplitude is required to achieve the desired radial secular frequencies on the order of 1 MHz to 3 MHz. An amplitude stability on the 0.1 % level over several hours is required for an radial mode frequency stability on the order of a few kHz, which is necessary for sideband cooling without subsequent frequency scans to track the actual sideband frequency. Fig. 3.3 shows all components which feed the rf signal to the trap. A frequency generator<sup>3</sup> (FG) referenced to a 10 MHz maser signal acts as frequency source. The output of the generator is attenuated (AT) by 5 dB. A small fraction of the output power is send as reference signal to a photon correlator, which bins PMT counts to that reference for micromotion compensation, c.f. Sec. 4.2. The remainder of the

<sup>3</sup>Marconi 2024

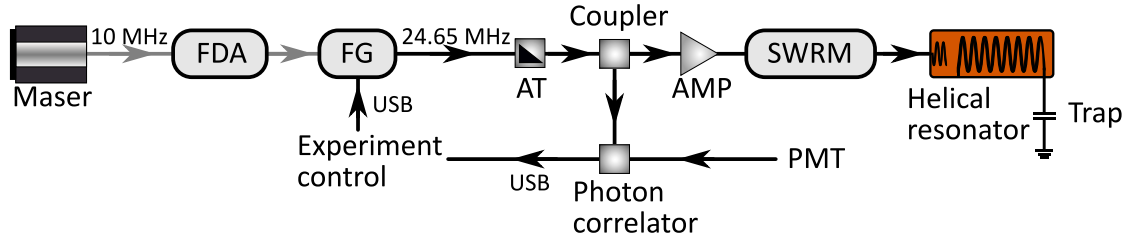


Figure 3.3.: Trap drive rf chain. A frequency generator (FG) referenced to a maser via a frequency distribution amplifier (FDA) generates the trap drive frequency at 24.65 MHz. The attenuated (AT) output signal is amplified and impedance matched to the trap via a helical resonator. A possible backreflection is detected in a standing-wave-ratio-meter (SWRM). For micromotion detection, PMT counts are binned to the trap drive in a photon correlator that is referenced to the FG via a rf coupler. Some components in the figure are adapted from [Franzen, 2009].

FG output seeds a 10 W amplifier (AMP). Its output power is measured by a rf powermeter<sup>4</sup> which also acts as backreflection detector via the integrated standing-wave-ratio-meter (SWRM). Since the impedances of the amplifier and the trap do not match and further voltage amplification is required, a helical resonator has been placed between the rf drive setup described and the rf electrodes of the trap. This shielded air-core transformer has been designed along the guidelines of [Macalpine and Schildknecht, 1959, Siverns et al., 2011], resulting in the parameters listed in Tab. A.2 and a quality factor  $Q \approx 300$ . The resonance frequency of the resulting device was shifted [Stepanova, 2017] to the so called *magic drive frequency* for  $^{40}\text{Ca}^+$  at 24.65 MHz, where the second order Doppler and ac Stark shift of the trap drive cancel [Dube et al., 2005]. Fig. 3.4(a) shows the obtained radial trap frequency of a single  $^{40}\text{Ca}^+$  versus the helical resonator input power and Fig. 3.4(b) the radial mode splitting as a function of one of the compensation voltages (right). The frequencies were measured by parametric excitation, i.e. application of a resonant ac potential to an axially neighboring electrode of the loading zone. The eigenfrequencies are revealed by a blurring of the ion on camera image and a drop in fluorescence counts. Both measurements were performed in the 1 mm long experiment zone 3, but the result should practically apply for the other zones as well, since the radial mode frequencies only weakly depend on the zone length, cf. Eq. (2.11). In conclusion, radial trap frequencies of up to 3 MHz can be obtained for a single  $^{40}\text{Ca}^+$  ion with approximately 3 W rf power. The radial mode splitting can be adjusted via one

<sup>4</sup>DAIWA CN-801

### 3. Transportable aluminum optical clock setup

of the compensation voltages in a range that is beneficial for possible future EIT cooling [Morigi et al., 2000, Roos et al., 2000, Schmidt-Kaler et al., 2001] in this setup, which allows for cooling of both radial modes with the same laser settings or even of all modes in the case of double-bright EIT cooling [Scharnhorst et al., 2017].

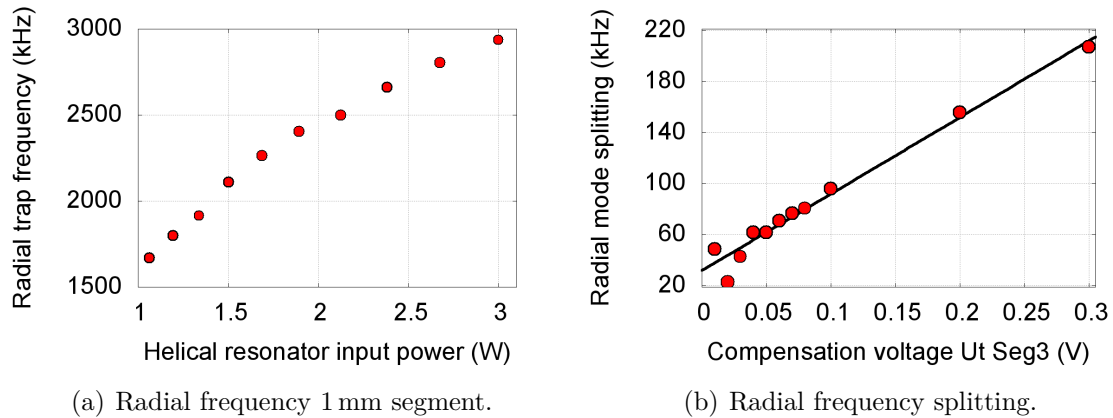


Figure 3.4.: Radial trap frequency in the 1 mm spectroscopy zone. (a): radial trap frequency as function of the rf output power of the frequency generator. (b): linear fit of the radial mode splitting, controlled by one of the compensation voltages, cf. Fig. 3.1). For both measurement series, the errors are too small to be depicted.

### 3.3. DC voltage source

Complementary to the single ac source described in the previous subsection, 28 dc electrodes are required to define the axial confinement and to compensate micromotion in all trap zones individually. For this purpose, a low-drift, low-noise, multichannel dc voltage source has been developed. In this section, the key properties will be presented. Further details are provided in the publication by [Beev et al., 2017]. To reach a low Lamb-Dicke factor (cf. Sec. 4.1.2), axial trap frequencies on the order of a few MHz are desirable. Trap zone lengths of 1 mm to 2 mm were chosen to obtain a reasonably homogeneous field distribution inside the trapping volume. Therefore, confining potentials of more than 100 V are required. At the same time, the voltages have to be set with few mV accuracy and mV stability on time scales of days; otherwise the micromotion compensation would be limited by the stability of the dc voltages. To fulfill those demands, 10 V output voltages of

16 bit DAC cards<sup>5</sup> are amplified by a factor of 12 to obtain 0 to 120 V common mode with 3.7 mV/LSB (least significant bit) and differential voltages of  $\pm 5$  V with 150  $\mu$ V/LSB or  $\pm 16$  V with 610  $\mu$ V/LSB resolution are added. Pairs of voltages are generated in one case by adding the fine stepped differential voltage channel to the common mode and in the other case by subtracting it. Moreover, one bias-t per output channel allows for galvanically isolated output voltage modulation, which is required for trap frequency determination via parametric excitation of the ion's motional modes. The assignment of the resulting voltages to the trap electrodes has implicitly been presented in Fig. 3.1,  $U_t$  and  $U_e$  are common mode voltages, while  $U_{tc}$  is a finely stepped differential voltage and  $U_{ec}$  the coarsely stepped counterpart.

Fig. 3.5 shows the measured axial trap frequency of a single  $^{40}\text{Ca}^+$  ion confined inside the 1 mm long spectroscopy zone as function of the axially confining potential. The measured values follow the expected square root dependency from the potential, cf. Eq. 2.12, as indicated by the fit curve.

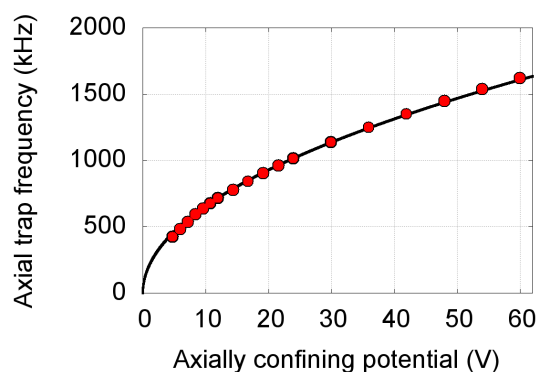


Figure 3.5.: Axial trap frequency versus confining potential in the 1 mm spectroscopy zone. The measured values follow the expected square root dependency from the potential, cf. (2.12), as indicated by the black fit curve. The errors are too small to be depicted.

<sup>5</sup>National Instruments<sup>®</sup> rack Mod. No. cDAQ-9174 equipped with three cards Mod. No. 9264

## 3.4. Vacuum system

Experiments on ions confined in rf traps require low background gas particle collision rates to prevent ion loss or heating due to particle impacts. Therefore, the experiments are performed in a chamber under ultra high vacuum. The chamber used here is depicted in Fig. 3.6. It is composed of an octagonal vessel<sup>6</sup> with a number of viewports, flanges, and extension tubes attached. All metal components are made of titanium alloy (Ti-6Al-4V) that features a low relative magnetic permeability of  $\mu - 1 \approx 5 \times 10^{-5}$ . Therefore, external fields are not disturbed by the chamber, which simplifies magnetic field stabilization at the trap center, when a field sensor mounted outside the chamber is used. A positive side effect is the high sticking coefficient of titanium making the inner walls a vacuum pump by adsorbing background gas particles. The ion trap assembly shown in Fig. 3.2 is connected to the inner surface of the bottom CF40 port of the octagon via grove grabbers. Therefore the chamber can act as heatsink to minimize the temperature rise of the trap due to dielectric loss of the rf drive. A t-tube connected to the bottom CF40 port houses a hot cathode gauge<sup>7</sup> (green) at one end and a valve (purple) at the other one. The latter is used to evacuate the chamber from ambient pressure down to approximately  $10^{-9}$  mbar using an external pump. After this level is reached the valve (purple) is closed and a non-evaporative getter pump<sup>8</sup> (red) reduces the pressure below  $10^{-10}$  mbar. Since this pump might possibly emit spurious particles during activation, its direct line of sight to the trap center is blocked with an OFHC copper sheet to prevent patch charge formation on the trap. Furthermore, an angled laser beam block made of aluminum with a light absorbent coating<sup>9</sup> is placed in the center of the t-tube to prevent light emerging from the top viewport from being scattered at the shiny inner tube surface. The helical resonator explained in Sec. 3.2 is connected to the trap via a custom-made two pin electric feedthrough and OFHC copper stripes inside the chamber. The pins of the feedthrough are electrically isolated from the flange by sapphire rings, since these provide low dielectric loss and additionally high heat conductance to transfer rf induced heat from the trap to the chamber. Two 25-pole d-sub feedthroughs (yellow) provide dc voltages via Kapton<sup>®</sup> isolated copper wires to the trap electrodes and the ablation target. Moreover, the two temperature

---

<sup>6</sup>Kimball Physics MCF800-SphOct-G2C8

<sup>7</sup>Agilent UHV-24 Bayard-Alpert Gauge Tube

<sup>8</sup>SAES Getters NEXTORR D 200-5

<sup>9</sup>Magic Black<sup>™</sup>

sensors on the trap are connected to these feedthroughs. All other CF40 flanges of the vessel are covered by UV fused silica (UVFS) viewports to optically access the ablation target and the ions inside the trap. The viewports are on both sides anti-reflective (AR) coated for 267 nm and partially reflective (PR) for 397 nm to 422 nm, since these wavelengths are most critical in terms of electric patch charge formation due to photoionization caused by reflections hitting the trap. The same goes for the CF160 viewports, which are inverted to grant adequate optical access to the trap volume. Therefore, the imaging system described in Sec. 3.9 is mounted in front of one of these viewports.

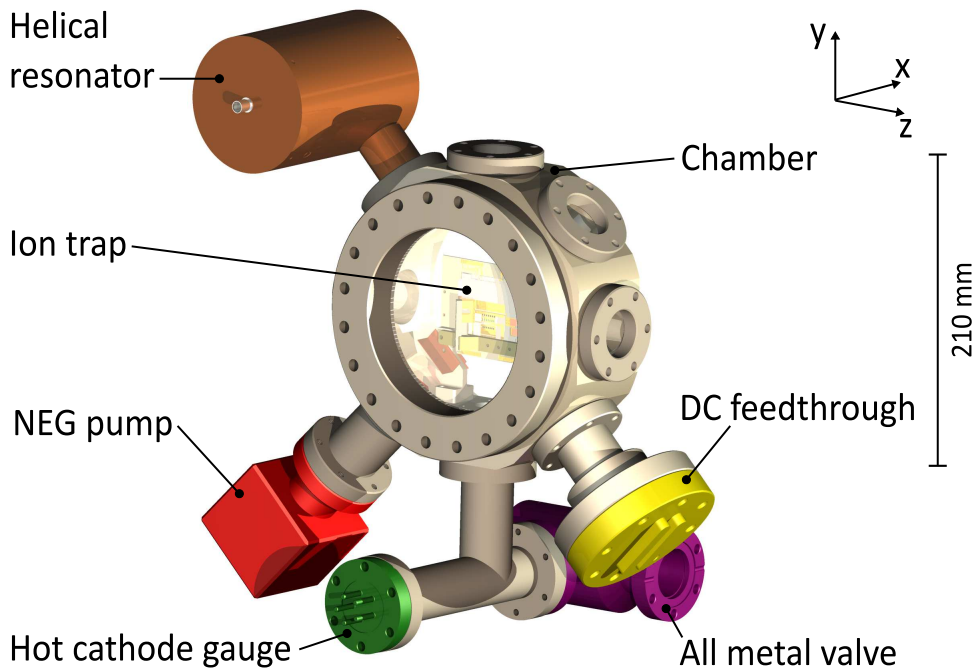


Figure 3.6.: Rendering of the vacuum setup. The central vessel, all viewports, tubes, and feedthroughs are made of titanium alloy (Ti-6Al-4V) with a low relative magnetic permeability.

### 3.5. Coil system

The magnetic field vector at the ions' position has to be set precisely to provide the quantization axis. The absolute value of the B-field determines the Zeeman splitting of the magnetic sublevels (cf. Fig. 4.2) and therefore the transition frequencies. Since the 729 nm laser has a narrow linewidth, the absolute value of the B-field has to be so stable that the corresponding frequency fluctuations of the transitions of interest

### 3. Transportable aluminum optical clock setup

are smaller than the actual linewidth of those transitions. Otherwise the relative drift of the transition and the laser frequency would cause the experiment to fail. Considering the  $S_{1/2}$  to  $D_{5/2}$  transition, whose frequency shifts by roughly 30 kHz per  $\mu\text{T}$ , this requires a B-field stability of about 30 nT over the duration of the experiment to reach 1 kHz frequency stability.

To set the B-field at the ion position, a cage composed of three pairs of magnetic coils each in a Helmholtz-like configuration has been build symmetrically around the center of the vacuum chamber. Its specifications are listed in Tab. A.1. Both coils of each pair feature the same number of windings and are electrically connected in series to a stable current source<sup>10</sup>. Experimentally, a quantization field of 86  $\mu\text{T}$  per Ampere coil current was inferred from the Zeeman splitting of the  $S_{1/2}$  to  $D_{5/2}$  transition. The noise and ripple of the current source are specified to be below 0.2 mA, which is equivalent to 17 nT or approximately 0.5 kHz on the  $^{40}\text{Ca}^+$  logic transition. This is a factor of two better than the design goal stated above.

## 3.6. Laser system for ionization and Doppler cooling

Figure 3.7 gives an overview of the lasers required for loading, Doppler cooling, and repumping  $^{40}\text{Ca}^+$ . Laser cooling is implemented with an external diode laser (ECDL<sup>11</sup>) at 397 nm that is split into two paths of equal optical power by a non-polarizing beamsplitter. Each path contains a 200 MHz center frequency double-pass acousto-optical modulator (AOM) for frequency tuning by  $\pm 50$  MHz. The zeroth order of DP – AOM<sub>1</sub> is split into two far detuned helper beams for rapid cooling of hot ions [Wübbena et al., 2012]. One of the helper beams is overlapped with the positive second order of the same AOM, the resonant Ca photoionization ECDL at 422 nm, and the two repumper beams to be coupled in a large mode area (LMA) photonic crystal fiber (PCF) that is polarization-maintaining (pm) and highly light-transmissive for all four wavelengths involved. The PCF output light is delivered on the trap axis, c.f. Fig. 3.12. The second helper beam is required for diagonal application through the loading zone for 3d laser cooling therein. Both helper beams are shuttered individually by mechanical shutters (MS). This configuration allows for ion loading and cooling in the loading zone, and subsequent shuttling the ions to the spectroscopy zone without any laser realignments. The repumper beams are

---

<sup>10</sup>TTI QL355TP

<sup>11</sup>All employed ECDLs are Toptica DL Pro Systems.



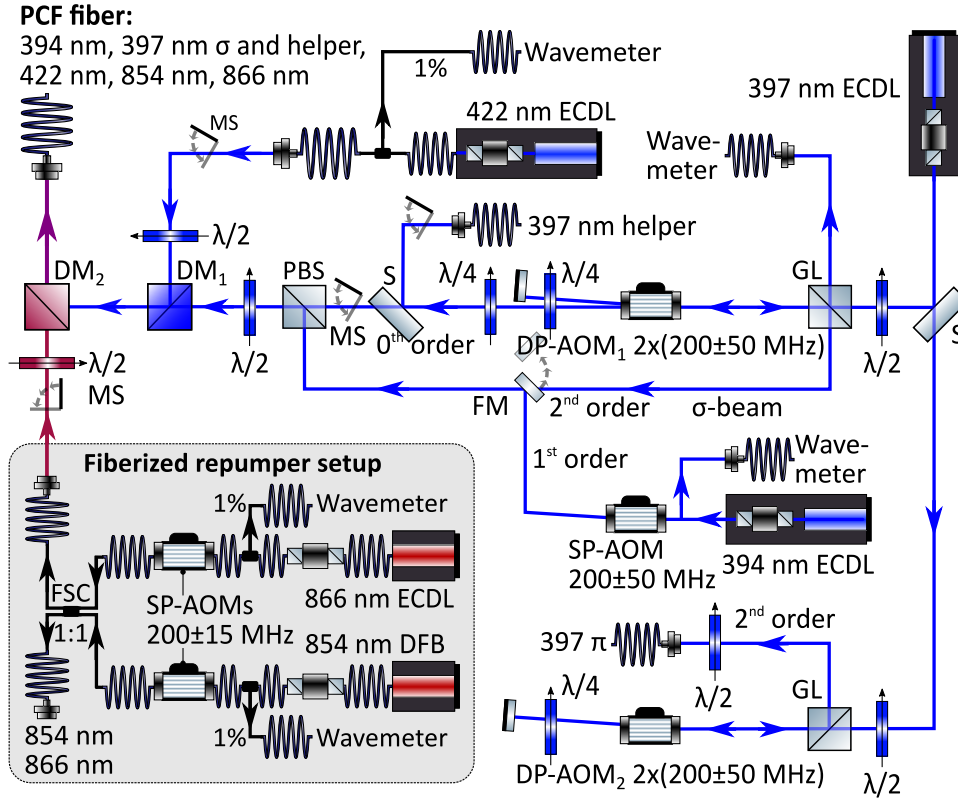


Figure 3.7.: Schematic layout of the  $\text{Ca}^+$  cooling laser system including the two resonant photoionization lasers for both species. The  $^{40}\text{Ca}^+$  cooling laser at 397 nm is split into two paths through a double-pass (DP) AOM each, generating independent beams for  $\sigma$ - and  $\pi$ -polarization (see also Fig. 3.12). The two repumper lasers are part of a compact fully fiberized setup, including optical isolators, fiber-taps to the wavelength meter, fiberized single-pass (SP) AOMs and fiber-combiners (FSC). Both beams are overlapped with the resonant photoionization laser beams at 422 nm for Ca and 394 nm for Al, before they are coupled into a large mode area photonic crystal fiber (PCF) to be delivered on the trap axis. DM: Dichroic mirror, FM: Flip-mirror, GL: Glan Laser, MS: motorized shutter, PBS: polarizing beam splitter, S: 50/50 splitter,  $\lambda/n$ : waveplate. From [Hannig et al., 2018b]. Some components in the figure are adapted from [Franzen, 2009].

generated in a all-fiber part of the setup, starting with a 866 nm ECDL and a 854 nm distributed feedback (DFB) laser<sup>12</sup>, which are send through individual fiberized optical isolators. In two fiber splitters 1% of the power is coupled to a wavelength meter (WLM). Two fiber-coupled single-pass AOMs are used as fast shutters and

<sup>12</sup>Eagleyard photonics EYP-DFB-0853-00050-1500-BFY02-0000

### 3. Transportable aluminum optical clock setup

for fine-tuning of the laser wavelength with a 3 dB bandwidth of  $\pm 15$  MHz. Behind those, both wavelengths enter a 50 % fiber combiner, which splits equal contributions to both of its output ports. All of the aforementioned optical fibers are polarization-maintaining in order to suppress power fluctuations after the polarization cleaning elements passing through the vacuum chamber. The last light source required for loading of  $^{40}\text{Ca}^+$  ions operates at a wavelength of 375 nm to provide the light for the second ionization step of Ca. Since the exact wavelength is not critical, cf. Sec. 2.5, a current and temperature stabilized laser diode that is not exposed to any optical feedback suffices for this task. The light is collimated, shuttered to avoid the creation of patch-charges on the trap after loading, and then fiber-coupled.

For sideband cooling and clock operation, a narrow linewidth logic laser at 729 nm is required. The corresponding laser system is discussed in Sec. 3.7, after the WLM frequency stabilization in the following section.

#### 3.6.1. Wavelength meter laser frequency stabilization

In the previous subsection, the laser system required for  $^{40}\text{Ca}^+$  ionization, cooling and coherent manipulation has been presented, including the pick-offs to the wavelength meter<sup>13</sup> (WLM) used for frequency monitoring. The requirements of the presented lasers in linewidth and frequency stability reach from sub-kHz linewidth and stability over minutes for the 729 nm logic laser to specifications given in nm for the 375 nm laser. While the latter does not require any stabilization but temperature control on the 1 K level, the logic laser requires frequency stabilization to an ultra stable cavity. All other lasers lie in between of these two extremes, e.g. cooling close to the Doppler limit requires MHz accuracy plus stability and therefore sub-MHz linewidth. While such linewidths are provided by state of the art ECDLs by design [Toptica Photonics AG, 2018], the frequencies need to be long-term stabilized to the WLM. The general approach of the WLM frequency stabilization is similar to previous work [Couturier et al., 2018, Saleh et al., 2015, Kobtsev et al., 2007], but here single-mode fiber-switches connected via single-mode pm photonic crystal fibers (PCF) to the WLM are employed and the WLM is not calibrated during the measurements. The setup is depicted in Fig. 3.8. Two fiber switches provide 14 freely usable single-mode (sm) polarization-maintaining (pm) inputs plus one calibration input. Here the 729 nm laser of the stationary  $^{27}\text{Al}^+$  clock setup is employed

---

<sup>13</sup>High Finesse ANGSTROM WS/U-10U

for frequency calibration since its frequency is stabilized to an ultrastable reference via a fiber frequency comb [Scharnhorst et al., 2015].

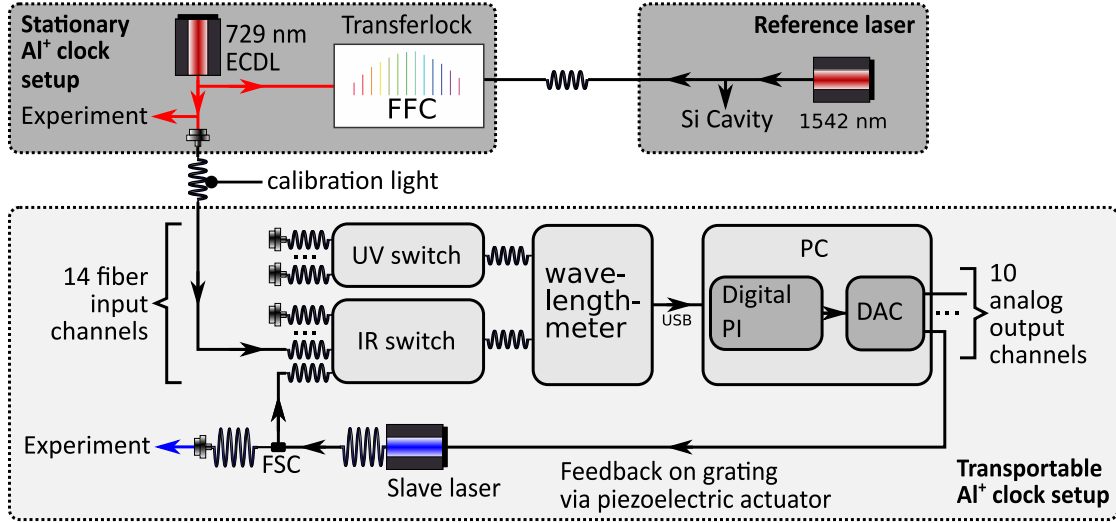


Figure 3.8.: Schematic overview of the frequency stabilization via the WLM. The IQLOC1 729 nm ECDL is frequency stabilized to an external reference laser at 1542 nm that is stabilized to a cryogenic Si cavity [Scharnhorst et al., 2015]. The IQLOC1 729 nm light is used to calibrate the IQLOC2 wavelength meter. For the frequency stabilization of slave lasers, a fraction of the output light is sent to the WLM via a fiber splitter combiner (FSC). Its reading is fed in a software PID on a PC, which acts back on the laser frequency via an analog output voltage generated by a DAC card that acts on the grating in the ECDL. Some components in the figure are adapted from [Franzen, 2009].

For the frequency stabilization of the slave lasers, the corresponding frequency measurement results of the WLM are processed by software proportional integral (PI) controllers on a standard PC, that control analog voltages generated by a digital analog converter (DAC) Peripheral Component Interconnect (PCI) card that act on the diffractive gratings in the resonators of the ECDL or on the current through the DFB laser and therefore close the feedback loop. Due to the subsequent measurements of the laser frequencies for exposure times on the order of tens of ms, this method is much slower than e.g. individual frequency stabilization to reference cavities implemented in specialized analog or digital PI controllers such as presented by [Fenske, 2015]. But since ECDLs in a temperature-stabilized environment typically drift by less than  $1 \text{ MHz s}^{-1}$  a frequency stabilization to the WLM is sufficient. Moreover, the setup employed to stabilize all the frequencies to the WLM is more

### 3. Transportable aluminum optical clock setup

compact than the alternative solution based on wavelength specific reference cavities. Since major parts of the frequency stabilization to the WLM are implemented in optical fibers, this solution is mechanically robust and therefore well-suited for a transportable optical clock.

During the calibration process the WLM cannot perform any other measurement and therefore not stabilize any laser frequency. Since the calibration lasts for several seconds, severe laser drift can occur during this time, which affects the clock operation e.g. by inefficient Doppler cooling resulting in crystal heat-up. Thus, it is preferable to choose a low calibration rate.

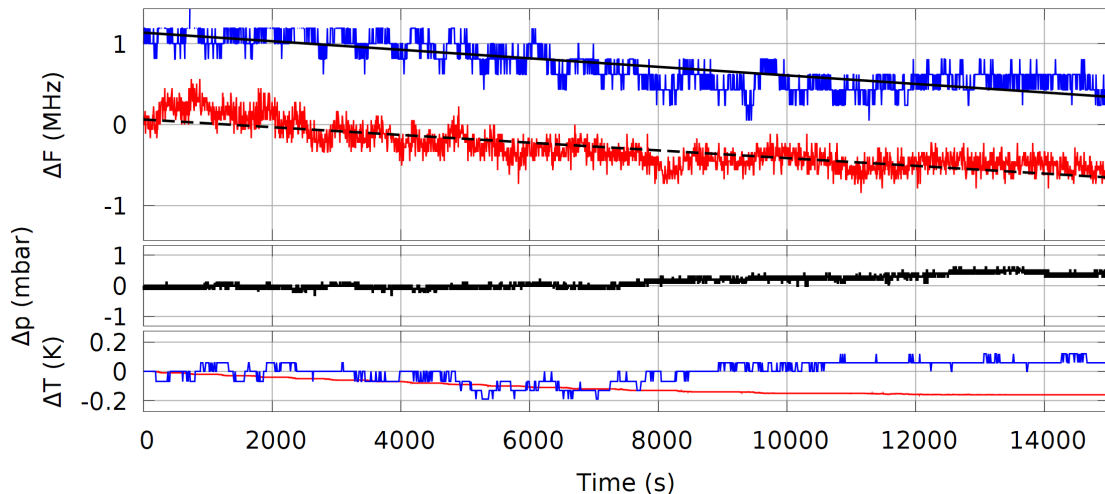


Figure 3.9.: WLM drift characterization. The frequency drift of the 397 and 729 nm laser were recorded while both lasers were frequency stabilized to the ultrastable reference. Top: blue (red): measured 397 nm (729 nm) frequency, black solid (dashed): linear fits. Bottom: pressure and temperature measured by the WLM (red) and on top of the box covering the WLM (blue). All offsets have been removed. The linear fit results in a drift of  $-0.190 \text{ MHz h}^{-1}$  ( $-0.171 \text{ MHz h}^{-1}$ ) for 397 nm (729 nm). From [Hannig et al., 2018b].

To characterize the readout frequency drift of the WLM the frequencies of the 729 and 397 nm laser were recorded while both lasers were frequency-stabilized to a highly stable reference laser at 1542 nm [Scharnhorst et al., 2015], whose typical drift by less than 10 kHz per day can be neglected. All devices were operated in a laboratory environment with  $\pm 0.2 \text{ K}$  temperature stability during the measurement according to the temperature log of the air conditioning system. The WLM was placed on a vibration damped breadboard and covered by a box to prevent intense air flow through the device. The temperature and air pressure were measured by

internal sensors of the WLM and recorded. The results are shown in Fig. 3.9. The measured frequency of the 397 nm (729 nm) laser drifts by  $-0.190 \text{ MHz h}^{-1}$  ( $-0.171 \text{ MHz h}^{-1}$ ). Both measurements fluctuate by approximately 1.0 MHz peak-to-peak on a timescale of one hour. The linear drifts are less than half of the values reported by [Saleh et al., 2015] for a current WLM from the same manufacturer but from another product series, which was thermally shielded. Moreover, the drifts reported here are more than two orders of magnitude smaller than value measured by [Kobtsev et al., 2007] for a prior device.

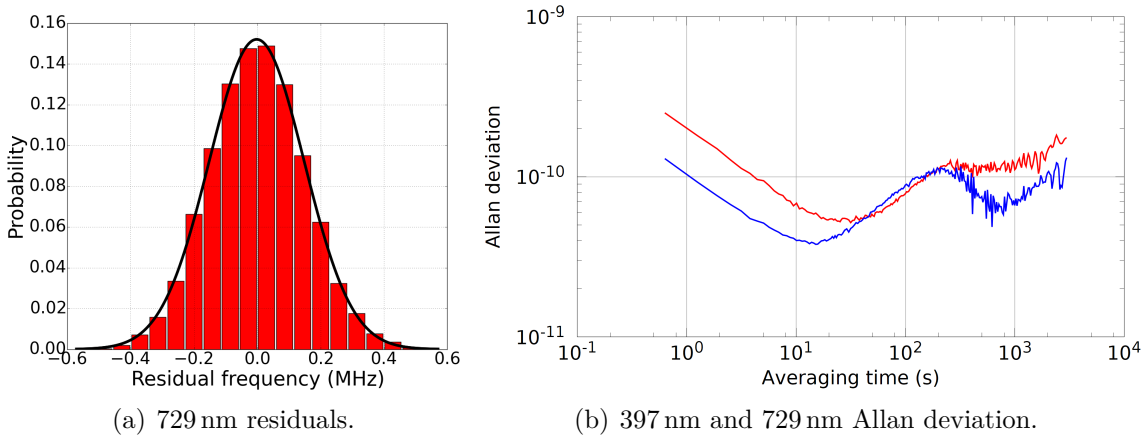


Figure 3.10.: Stability of the WLM frequency readout. a): distribution of the 729 nm frequency residuals after linear drift subtraction (red bars). The black curve is a gaussian fit to the data resulting in a standard deviation of  $\sigma = 0.15 \text{ MHz}$ . b): The curves show the fractional frequency Allan deviation of the wavelength meter measurements at 397 nm (blue) and 729 nm (red). Both lasers were frequency stabilized to the ultrastable reference. The linear drift has been subtracted. The measurements were taken simultaneously over 15 000 s. From [Hannig et al., 2018b].

Fig. 3.10(a) shows the distribution of the residuals of the 729 nm frequency recording after subtraction of the linear drift (red bars). A Gaussian fit to the data results in a standard deviation of  $\sigma = 0.15 \text{ MHz}$  (black curve). Fig. 3.10(b) shows the fractional Allan deviations derived from the frequency recordings after subtraction of the individual linear drifts. In both cases the Allan deviation stays below  $3 \times 10^{-10}$  over the entire range of averaging times, which equals approximately 0.2 MHz in case of the 397 nm laser. This is comparable to the results measured by [Saleh et al., 2015] and about a factor of three lower than the values reported by [Couturier et al., 2018]. Since the frequency drifts and the standard deviation of the residuals

### 3. Transportable aluminum optical clock setup

are small compared to the natural linewidth of the Doppler cooling transition, the WLM is well suited to stabilize the frequencies of the lasers listed above plus the resonant Al ionization laser, which is not actively stabilized yet for technical reasons. This simplifies the setup compared to other solutions like individual reference cavities for all lasers and is more cost-efficient than a frequency comb.

## 3.7. Calcium logic laser system

The  $^{40}\text{Ca}^+$  logic laser system presented in this section is a refined version of the setup built up and presented by [Stepanova, 2017].

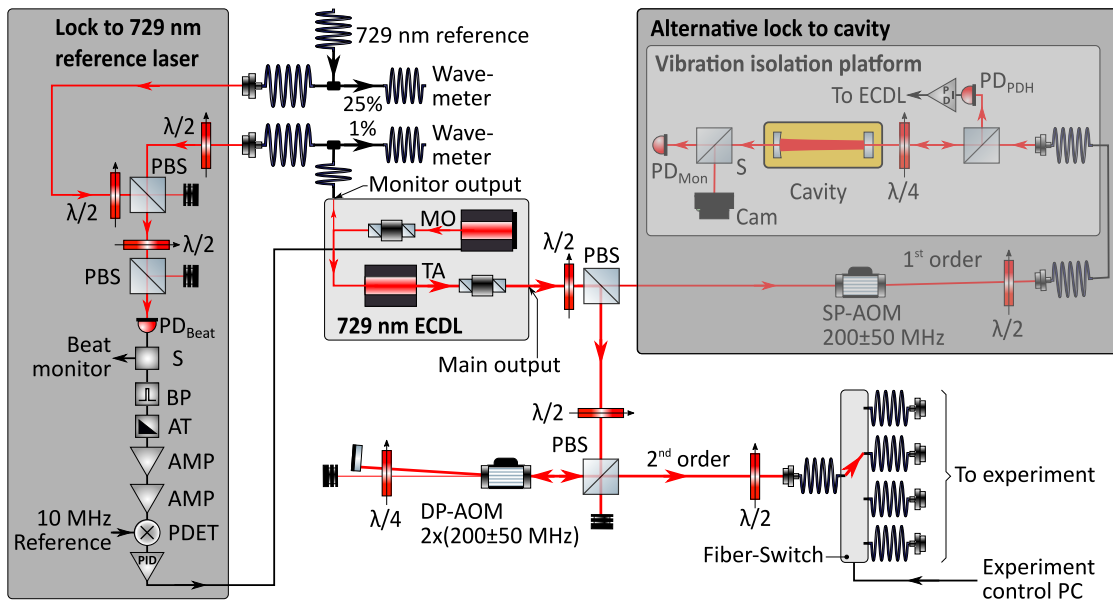


Figure 3.11.:  $^{40}\text{Ca}^+$  logic laser system. 729 nm light is generated by an ECDL system composed of a master oscillator (MO) that seeds a tapered amplifier (TA). The main output power is frequency shifted by an DP-AOM and directed to the experiment via a fiber switch to select the output port and therefore the direction, cf. Fig. 3.12. The laser frequency is either stabilized to an external 729 nm reference (left) or to an ultrastable cavity (right). Details are given in the main text.  $\lambda/n$ : waveplate, PBS: polarizing beam splitter, PD: photodiode, S: splitter, BP: band-pass filter, AT: attenuator, AMP: amplifier, PDET: phase detector, PID: proportional differential integral controller. The setup is a refined version of the one presented in [Stepanova, 2017]. Some components in the figure are adapted from [Franzen, 2009].

In the previous sections the laser systems for photoionization and Doppler cooling and their stabilization to the WLM have been described. Here, the 729 nm laser system required for sideband cooling and spectroscopy will be discussed. For spectroscopy of the narrow  $^{40}\text{Ca}^+$  logic line a linewidth of less than one kHz and sub kHz frequency stability over minutes are required. Moreover, the optical power in front of the vacuum chamber should be well above 10 mW to achieve a high intensity at the ion and therefore Rabi-flopping on few  $\mu\text{s}$  time scales.

The laser system is depicted in Fig. 3.11. To obtain the desired power, a commercial ECDL system<sup>14</sup> in master oscillator power amplifier (MOPA) configuration was chosen, i.e. an narrow linewidth, low power master ECDL that seeds a tapered amplifier. Most of the light emitted from the main output of the system is frequency shifted by  $\pm 50$  MHz in a DP-AOM and then coupled into a pm fiber switch<sup>15</sup> to choose between different beam directions through the trap. The switch is triggered by the experiment control system, cf. Sec. 3.11.

There are two different approaches implemented to narrow the intrinsic linewidth of the laser and to stabilize its frequency. The first alternative is depicted on the left side of Fig. 3.11: a heterodyne beat with the ultra stable reference laser at 729 nm that is also used for the WLM calibration, cf. Sec. 3.6.1. For this purpose, light from the monitor output of the 729 nm ECDL and from the reference laser are overlapped in a PBS. Then the polarizations of the overlapped beams are turned and projected in one plane in a second PBS to make them interfere. This optical beat is transferred to an electric signal in a photodiode, filtered by a band-pass, amplified, and then mixed down to dc with a stable 10 MHz signal from a maser in a phase detector<sup>16</sup>. The resulting error signal is fed in a PID regulator<sup>17</sup> whose output acts on the laser diode current of the master laser. In summary, in this approach the difference frequency of the  $^{40}\text{Ca}^+$  logic laser of the transportable setup and the ultra stable counterpart at the stationary setup is frequency stabilized to a 10 MHz reference maser. The frequency stability is essentially given by the drift of the ultra stable reference laser, which is less than 10 kHz per day. Beside this high performance, the first alternative has one major disadvantage: with the ultra-stable reference cavity, it relies on hardware that is not transportable.

The second alternative presented on the right side of Fig. 3.11 solves the trans-

---

<sup>14</sup>Toptica TA pro

<sup>15</sup>LEONI eol 1x4

<sup>16</sup>Mini Circuits ZRPD-1+

<sup>17</sup>Toptica FALC

### 3. Transportable aluminum optical clock setup

portability issue. A small fraction of the main output light of the ECDL is frequency shifted and modulated by a single pass (SP) AOM and then stabilized to a 100 mm reference cavity using the Pound-Drever-Hall scheme [Drever et al., 1983], which is based on a phase comparison between light directly reflected from the cavity front mirror and frequency averaged light "leaking" through that mirror from the inside of the resonator. The cavity is placed inside a heat-shield within a vacuum chamber to reduce its thermal drift. Moreover, the breadboard carrying the cavity and all the optics required for the frequency stabilization has been installed on an active vibration isolation platform to suppress structure-borne noise. A finesse of  $11013 \pm 22$  was determined from cavity ring-down measurements. Furthermore, a stabilized linewidth of  $(156 \pm 5)$  Hz and a frequency drift of  $21 \text{ Hz s}^{-1}$  were obtained. More details on the technical implementation and the measurements can be found in [Stepanova, 2017]. While the linewidth is well suited for an  $^{27}\text{Al}^+ / ^{40}\text{Ca}^+$  clock, the cavity drift is impractical. Since it is probably caused by a temperature drift of the cavity spacer, a future outer thermal insulation for the cavity vacuum chamber can act as a thermal low-pass filter and thereby suppress the drift. For the measurements presented in this thesis, the first frequency stabilization method has been used.

Up to here, only  $^{40}\text{Ca}^+$  laser systems have been presented. The  $^{27}\text{Al}^+$  laser setup will be presented in the separate chapter 5. Both UV lasers have been build for the stationary  $^{27}\text{Al}^+$  clock, but at the time this thesis was written, preparations to build a second pair of lasers for the transportable clock had started.

## 3.8. Optical setup around the vacuum chamber

Figure 3.12 shows two schematic cross sections of the vacuum chamber and the surrounding optical setup to apply the presented lasers to the ions.

The laser beams for photoionization, cooling and coherent manipulation of  $^{40}\text{Ca}^+$  are delivered through various sm polarization maintaining optical fibers around the vacuum chamber and then focused down to spot diameters between 60 and 180  $\mu\text{m}$  at the trap center. Therefore, all light intensities are approximately constant on length scales of a few  $\mu\text{m}$  defined by the spacing of a two-ion-crystal. In case of the 397 nm and 729 nm beams, the polarization is cleaned by Glan Laser (GL) and Glan Taylor (GT) polarizers, respectively, and then set by half or quarter waveplates ( $\lambda/n$ ). Various photodiodes ( $\text{PD}_i$ ) placed behind backside-polished mirrors allow for



### 3.8. Optical setup around the vacuum chamber

optical power monitoring. The diagonal beams form angles of approximately  $50^\circ$  with the trap axis, to enable high numerical aperture imaging of the ions through one of the inverted viewports, which is subject of the next section.

Pulsed light at 534 nm is used for neutral atom ablation from solid targets. It is generated by a frequency-doubled Q-switched Nd:YAG laser<sup>18</sup> at 1064 nm and focused down to a spot size of approximately  $200\ \mu\text{m}$  on the target. More details are provided in Sec. 3.10.

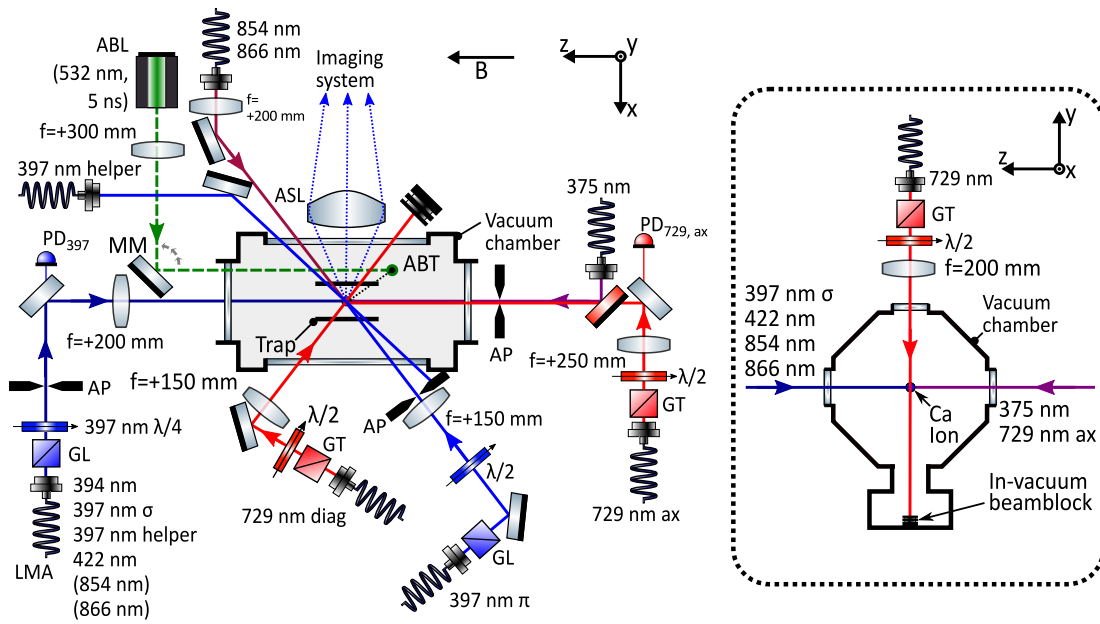


Figure 3.12.: Schematic horizontal cross section of the vacuum chamber and the surrounding optics, not to scale. The ablation laser (ABL) spot on the ablation target (ABT) is aligned via the motorized mirror (MM). Fluorescence light is collected with a biaspheric lens (ASL) through a slightly inverted viewport. All beams required for  $\text{Ca}^+$  loading and coherent manipulation are delivered via various polarization maintaining and large mode area (LMA) glass fibers<sup>19</sup>. The insert shows a vertical cross section with the optics on the top viewport. Three pairs of magnetic field coils surrounding the chamber are not depicted for simplification. GL: Glan Laser polarizer, GT: Glan Taylor polarizer,  $\lambda/n$ : waveplate, AP: aperture. Based on [Hannig et al., 2018b]. Some components in the figure are adapted from [Franzen, 2009].

<sup>18</sup>Continuum Minilite I MD

### 3.9. Imaging system

Fast high-fidelity state detection after electron shelving requires to collect as many fluorescence photons per time as possible, i.e. a large diameter imaging lens placed close to the ion to reach a high numerical aperture. Moreover, for ion-selective state determination in future multi-ion quantum logic optical clocks [Schulte et al., 2016], it is required to resolve single ions in a chain for typical axial trap frequencies of  $\omega_{\text{ax,Ca}} = 1.6$  MHz that result in a two-ion distance of  $4.1 \mu\text{m}$  in the object plane [Wineland et al., 1998]. For a camera pixel size of  $6 \mu\text{m}$  in the image plane, a minimum magnification of factor 15 is required to obtain a clear separation of the images of individual ions by 10 pixels. After optimization, a magnification of 18 was chosen. The imaging system was chosen to be installed outside the vacuum chamber, therefore the minimum distance  $d_{\text{min}} = 36.6$  mm of the first lens surface from the trap center is defined by the apparatus. While a large objective diameter is advantageous in terms of the achievable numerical aperture, it can restrict optical access for diagonal laser beams, cf. Fig. 3.12. As a compromise, an outer lens diameter of  $50.8$  mm was chosen, leading to the aforementioned  $42.6$  mm effective optical diameter and a numerical aperture  $\text{NA} = 0.51$ . A single monochromatic biaspheric lens can be optimized to minimize spherical aberrations below the diffraction limit. Moreover, in contrast to the commonly employed multi-element lenses [Alt, 2002], no high accuracy alignment of multiple optical elements is required. However, with a single lens, a trade-off between diffraction-limited performance and field-of-view needs to be made. Therefore the imaging performance was optimized for a circular field of view with  $100 \mu\text{m}$  radius.

The imaging system was numerically optimized using a commercial ray tracing software<sup>20</sup>, where the spheric coefficients, conic constants, and the curvature of the ASL surface facing the camera were free parameters. The damped least square optimization was carried out for an error function resembling the root mean squared image spotsize for three point sources separated by a maximum of  $0.2$  mm in the object plane. The resulting parameters are listed in Tab. A.3. The simulation indicated a high sensitivity of the lens-to-ion distance to achieve diffraction-limited performance.

Fig. 3.13 shows the imaging system. After passing through the window (W) of the viewport, fluorescence light is collected with a single custom-made<sup>21</sup> biaspheric

---

<sup>20</sup>Lambda Research OSLO

<sup>21</sup>Asphericon

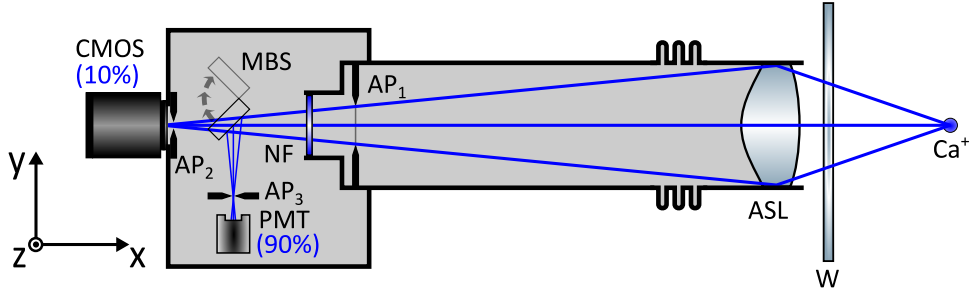


Figure 3.13.: Schematic cross section of the imaging system, not to scale. The fluorescence light is focused on a sCMOS camera and directed to a photomultiplier tube (PMT) with a single aspheric lens (ASL). The splitting is realized with a motorized flippable 90/10 beamsplitter (MBS). Spectral and spatial filtering are implemented using a notch filter (NF) and the apertures  $AP_i$ .

lens (ASL) optimized for diffraction-limited imaging at 397 nm, which is placed at a distance of 36.6 mm from the ion. With its effective diameter of 42.6 mm it covers about 7% solid angle. It is mounted in an 2 inch tube supported by a 3d linear stage used for alignment with respect to the trap center position. A light-tight rubber bellow connects this tube to a second one ending in a light tight box. Inside that box, the fluorescence light is spectrally filtered by a notch filter<sup>22</sup> (NF) to suppress ambient light and split 90:10 between a photo-multiplier tube<sup>23</sup> (PMT) and a sCMOS camera<sup>24</sup>. The beamsplitter can be flipped out of the beam path in order to transmit 100% of the light to the camera. While the PMT is a single photon counter that can be exploited for quantitative analyses of the signal, the camera gives a quick spatially resolved qualitative analyses option of the trap content (i.e. number of bright ions, indication for dark ions, as shown in Fig. 3.25). The image plane of the ASL coincides with the sCMOS chip, an aperture for spatial filtering of 397 nm stray light is placed in the focus in front of the PMT. Since the trap zones are in total  $\approx 8$  mm long it is not possible to image the entire trap on the  $13.3^2 \text{ mm}^2$  CMOS chip. Instead, the entire imaging system is mounted on an optical rail, that can be moved parallel to the trap axis via a motorized 1d translation stage. In conclusion, when a desired ion configuration is loaded, analyzed in one trapping zone, and afterwards shuttled to another, the imaging system can follow the movement of the ions.

<sup>22</sup>Thorlabs FBH400-40

<sup>23</sup>Hamamatsu H10682-210

<sup>24</sup>PCO edge 4.2LT

### 3. Transportable aluminum optical clock setup

Experimentally, with a Doppler-cooled  $\text{Ca}^+$  ion loaded into the trap, the ASL-to-ion distance and the sCMOS to ASL distance were iteratively varied in order to minimize the ion's point spread function (PSF) on the camera. Fig. 3.14(a) shows an Airy function fitted to the count distribution on a straight line through the center of the PSF. The first minimum of the fitted Airy function is found  $(0.793 \pm 0.013) \mu\text{m}$  from the global maximum. The value is given in the object plane, taking the 18-fold magnification of the imaging setup into account, which has been calibrated through an ion-ion distance measurement for known axial trapping frequencies. This result is 67% bigger the minimum resolvable distance of two point sources according to the Rayleigh criterion  $d = 0.61\lambda/NA \approx 475 \text{ nm}$ , where  $\lambda = 397 \text{ nm}$  is the wavelength and  $NA = 0.51$  the numerical aperture of the imaging system. The obtained resolution is similar to that reported by [Picken et al., 2017] for imaging of single caesium ions on a CMOS camera using a single aspheric lens located inside the vacuum chamber. However, here no costly in-vacuum alignment hardware is required and the numerical aperture is about 10% larger, which allows for a higher photon collection efficiency.

The FWHM depth of field is calculated following [Smith, 2000] to be  $DOF = \pm \frac{\lambda}{2NA^2} = \pm 0.765 \mu\text{m}$ .

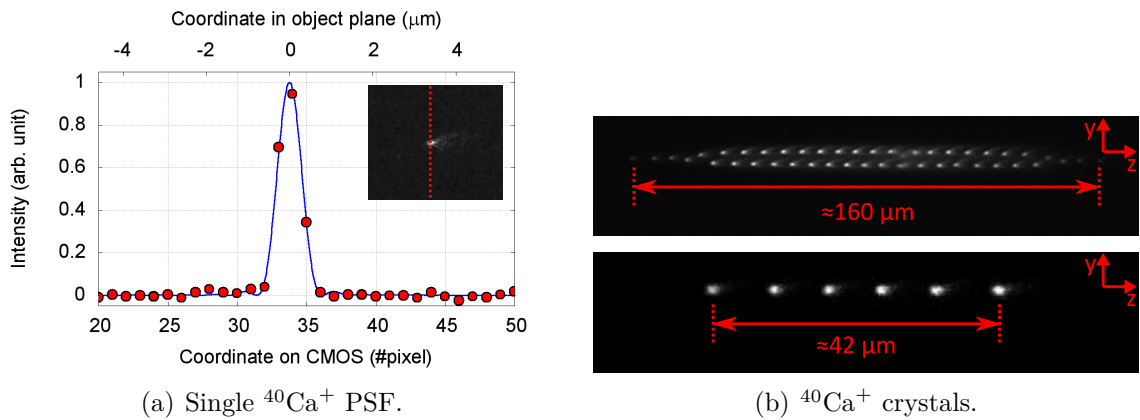


Figure 3.14.: Imaging performance. a): Point spread function of a single  $\text{Ca}^+$  ion on the CMOS chip (lower x-axis), background subtracted. Red: measured data, blue: fit curve. The upper scale gives the corresponding dimensions in the object plane taking into account the magnification of the imaging system. Fitting the function  $f(x) = I \cdot \left( \frac{2J_1(a(x-x_0))}{a(x-x_0)} \right)^2$  to the data resulted in  $I = 1.00 \pm 0.02$ ,  $a = (1.62 \pm 0.03) \text{ pixel}^{-1}$ , and  $x_0 = (33.76 \pm 0.02) \text{ pixel}$ . From [Hannig et al., 2018b]. b): two images of  $^{40}\text{Ca}^+$  crystals.

The Strehl ratio [Mahajan, 1983] (SR) for the biaspheric lens alone is estimated as

$$SR = \exp\left(-\left(\frac{2\pi\sigma}{\lambda}\right)^2\right) = 0.87, \quad (3.1)$$

where  $\sigma$  has been taken to be the total root-mean-squared form deviations of the aspheric surfaces measured by the manufacturer and  $\lambda$  the wavelength.

For a typical 300 ms exposure time of the sCMOS camera, 11477 counts were obtained in a  $10 \times 10$  pixel<sup>2</sup> region of interest (ROI) including the image of a Doppler-cooled  $^{40}\text{Ca}^+$  ion scattering at maximum intensity. For a dark ion (866 nm laser blocked) a background of 99.276 counts per pixel with an rms noise of 1.9 counts was measured, which is in good agreement with the offset of 100 counts per pixel added to the actually measured value by the camera software<sup>25</sup>. The background noise is clearly dominated by the camera electronic, the contribution of scattered light from the cooling laser is negligible. By subtracting the background counts for the ROI from the bright ion counts, an effective signal of 1549 counts for a bright ion is obtained. Subsequent division by the background rms noise yields a signal to noise ratio of 806.

With the PMT a dark count rate of below 0.1 kHz was measured and a count rate of  $(5.1 \pm 2.3)$  kHz due to scattered light at 397 nm. For a single  $^{40}\text{Ca}^+$  ion a bright count rate of  $(351 \pm 9)$  kHz was obtained, which is 55 % of the expected value of 638 kHz at saturation, derived from 22.4 MHz linewidth, 7 % solid angle covered by the biaspheric lens, and a total transmission of 86 % through the optical system including the notch filter, the 90 % beam sampler, and a photon counting efficiency of 0.3 specified by the manufacturer of the PMT. The Strehl ratio was not included into the calculation of expectation value, since the active area of the aperture in front of the PMT is approximately  $1.0 \times 1.0$  mm<sup>2</sup> and therefore much larger than the central feature of the single ion's image. Additionally, the exact position of the aperture relative to the image plane is not known.

For state detection via electron shelving, it is required to distinguish between the ion being in the  $S_{1/2}$  ground state (ion bright) and in the excited  $D_{5/2}$  state (ion dark). Here the threshold technique [Hemmerling et al., 2012] has been chosen, in which a threshold count is set, above which the ion is declared bright. In Fig. 3.15(a) the mean state discrimination error is shown as a function of this thresh-

---

<sup>25</sup>Offset according to W. Tutsch, PCO AG, 2018, private communication.

### 3. Transportable aluminum optical clock setup

old. Fig. 3.15(b) shows the measured photon count distributions for a bright (dark) ion as solid (dashed) curve, which was prepared by applying (blocking) the 866 nm repumper laser during Doppler cooling. For the chosen detection time of 50  $\mu\text{s}$ , the two distributions partially overlap. Therefore, any choice of the discrimination threshold (black dashed line) leads to a mean discrimination error of [Keselman et al., 2011]:

$$\epsilon = \frac{p_b(n \leq n_{\text{th}}) + p_d(n > n_{\text{th}})}{2}, \quad (3.2)$$

where  $n$  is the measured number of photons,  $n_{\text{th}}$  the threshold set, and  $p_b$  ( $p_d$ ) the probability to measure a bright (dark) ion. Thus, the numerator expresses the probability of a wrong state assignment to the measurement result. In the main figure, this error is plotted as function of the discrimination threshold for 25  $\mu\text{s}$  (50  $\mu\text{s}$  / 100  $\mu\text{s}$ ) detection time in red (green/blue). The red curve shows that a mean state discrimination error of below 0.2 % is obtained for 25  $\mu\text{s}$  detection time, which improves to below  $10^{-5}$  for 100  $\mu\text{s}$  detection time.

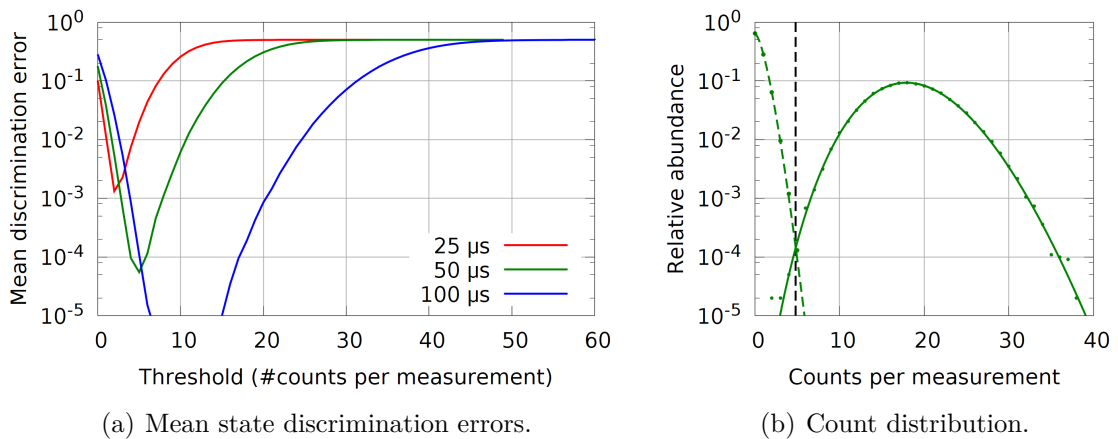


Figure 3.15.: State discrimination error for various detection times. a): the curves show the mean state discrimination error as function of the discrimination threshold for three different detection times. b): photon count distribution measured for 50  $\mu\text{s}$  detection time for a bright (dark) ion as solid (dashed) green curve and a reasonable threshold as dashed black vertical line. Adapted from [Hannig et al., 2018b].

### 3.10. Ablation targets

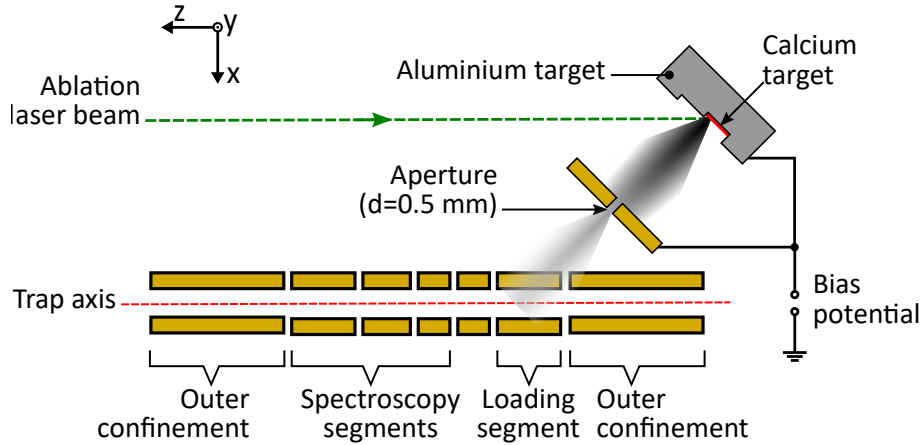


Figure 3.16.: Schematic horizontal cut through the trap center and the ablation target. The ablation laser beam can be tilted between the different targets to select either species to be loaded. An aperture restricts contamination with ablated material to the loading zone. The target-to-trap center distance is 17 mm. All photoionization lasers are aligned along the trap axis. From [Hannig et al., 2018b].

In the setup presented here, the ions are generated via *ablation loading*. Therefore, a Q-switched and frequency doubled Nd:YAG laser<sup>26</sup> (ABL) at 532 nm is focused down to a spot diameter of  $\approx 200 \mu\text{m}$  on a solid target for neutral atom beam generation via evaporation, as demonstrated by [Hendricks et al., 2007]. A schematic cross section of the ablation target used here is shown in Fig. 3.16. It consists of a body of aluminum with a two stepped groove milled in the surface pointing towards the loading zone. Calcium grains were glued<sup>27</sup> in one of the groves (red zone). A pulsed Ca atom beam can be produced by directing the laser on these grains, Al can be ablated from the Al body itself. For reproducible switching between calcium and aluminum ablation, the ABL beam is deflected by a mirror that can be tilted in two directions by two stepper motors. Since the ablated atoms emerge under a certain opening angle, a 0.5 mm diameter aperture is mounted 8 mm in front of the ablation target to reduce the opening angle so that the atom beams only enter the loading zone. This should prevent coatings of evaporated material that might influence micromotion via patch charge formation near the spectroscopy zones. To prevent unwanted ions generated by the ablation pulse from entering the trap, the aperture

<sup>26</sup>Continuum Minilite 1

<sup>27</sup>Thorlabs 353NDPK Epoxy

### 3. Transportable aluminum optical clock setup

is coated with gold and together with the target is connected to a negative dc bias voltage. After loading the desired ion crystal in the loading zone, it can be shuttled to one of the three spectroscopy zones by application of suitable dc potentials to the trap electrodes.

#### 3.10.1. Aluminum ion generation

In the previous section the imaging performance was characterized using a single  $^{40}\text{Ca}^+$  ion. In this section, the results of time of flight (TOF) measurements preparing ablation loading of  $^{27}\text{Al}^+$  are presented. Then the implementation of the latter in the apparatus is demonstrated, including velocity selective photoionization.

When this thesis was written, there were two common approaches for the generation of single ions in rf traps. The first technique is photoionization from a thermally generated atom beam. In this case, a solid state sample of the desired species is placed in an oven construction, e.g. the center hole of a ceramic tube, which is heated via a current through a resistance wire wound through the outer holes of the same tube, as in the stationary  $^{27}\text{Al}^+$  clock experiment [Wübbena, 2014]. While such ovens are rather simple and inexpensive to build, they require a heat-up time which is in the best reported case on the order of 12 s for a calcium oven [Ballance et al., 2018]. Given the lower vapor pressure of aluminum compared to calcium, a higher temperature and therefore a longer heat-up time is required to obtain a sufficient atom flux through the trap for loading. This is inconvenient in the case that a clock ensemble was lost during clock operation i.e. due to a chemical reaction with a background gas particle and therefore has to be replaced. Moreover, a failure in oven current control can cause a massive uncontrolled evaporation of the oven content, which can severely harm the physics package. An additional drawback is that the atom emission cannot be stopped immediately once an ion is trapped, which can complicate the loading process, especially for a clock requiring two ions of different species. Furthermore, the heating wire can reach temperatures sufficient for electron emission. The latter can create patch charges on or close to the ion trap electrodes that sweep off the current micromotion compensation settings. Lastly, an oven not only evaporates atoms of the species inside, but also any deposit layer on its outer surface. This can cause background gas pressure rises by two orders of magnitude, which severely increases the collision rate and therefore the risk of chemical reactions or kick-out loss of the ions just loaded.

The second technique is based on photoionization of neutral atoms, as well. But



here the latter are generated by applying a focused laser pulse on a bulk target of the desired species. This technique termed *ablation loading* has been implemented by multiple groups for different species, including  $^{27}\text{Al}^+$  [Guggemos et al., 2015],<sup>28</sup>. While the required pulsed laser is rather costly, the technique brings along several advantages compared to loading involving an atom oven. First of all, the laser energy per pulse and therefore the number of generated atoms can be set precisely and the pulses can be stopped immediately, once the desired number of ions has been loaded. Due to the power stability of the pulsed laser, there is no risk of generating a massive evaporation. Therefore, the vacuum pressure is almost not affected by loading with this technique. Lastly, for high pulse energies the ablation laser can generate ions of the desired species directly, which can be a backup solution in case an ionization laser is not operational<sup>29</sup>.

An alternative ionization method is electron impact ionization, discussed e.g. in the textbook by [Märk and Dunn, 2013]. In this case, atoms are ionized by collisions with highly energetic electrons from an electron gun. While this solution comes at lower direct financial costs compared to photoionization, it is not isotope-selective and can therefore ionize other species, which are not intended to be loaded. Further disadvantages are the higher risk of patch-charge generation on the trap electrodes and the additional volume in vacuum required in comparison to photoionization.

Weighting these arguments, laser ablation combined with photoionization has been chosen as loading technique for the transportable clock setup, as already presumed in the previous chapter for  $^{40}\text{Ca}^+$  loading. While the latter was directly implemented without any previous studies, some pilot measurements presented in the following subsection 3.10.2 were carried out before  $^{27}\text{Al}^+$  loading was successfully demonstrated, cf. Sec. 3.10.3.

---

<sup>28</sup>D. Hume, NIST, 2018, private communication.

<sup>29</sup>Ablation loading of  $^{40}\text{Ca}^+$  without additional ionization laser light has been demonstrated in the setup several times. The feasibility of this procedure for  $^{27}\text{Al}^+$  has not been investigated here so far. Since this technique has the disadvantage of increased laser power and therefore more ablated particles, it should not be employed in standard operation.

### 3.10.2. Time of flight measurements

From the neutral Al atom beam generated by laser ablation an ion is created by two-step photoionization. Afterwards it is sympathetically cooled until it crystallizes next to the  $^{40}\text{Ca}^+$  ion. The ion's mass is determined from the motional mode frequencies, cf. Eq. (2.15). Here, the goal was to maximize the  $^{27}\text{Al}^+$  loading efficiency in the first place and then to minimize the crystallization time. Firstly, the efficient generation of neutral Al atoms was optimized and their velocity distribution measured by performing TOF experiments in the apparatus depicted in Fig. 3.17(a), employing the sequence sketched in Fig. 3.17(b).

First, the ablation laser flash lamp and its Q-switch are triggered by the experiment control system. The intermediate delay sets the pulse energy. At the rising edge of the Q-switch trigger pulse, the 5 ns long ablation laser pulse is fired (green flash symbol). When this pulse hits the ablation target, atoms are evaporated. The atom beam was exposed to a 394 nm laser beam directed on the trap axis to excite only the first resonant stage of the photo ionization.

To collect as much fluorescence light from neutral atoms as possible, the slit in front of the PMT was opened completely. To obtain the number of neutral atoms reaching the trap volume as function of the TOF after the ABL pulse, the PMT counts were binned in 4  $\mu\text{s}$  time frames and summed upon multiple repetitions of the sequence, cf. Fig. 3.17(a).

The distance traveled by the neutral atoms during the life time of the excited state  $^2\text{S}_{1/2}$  is short compared to the ABT to trap center distance of 17 mm. A delay of 80 ns was measured between the rising edge of the Q-switch trigger and the arrival of the ablation laser pulse on the fast photodiode. Therefore, the delay between the Q-switch trigger pulse and the arrival of the ablation laser pulse at the target is less than 80 ns, which is much shorter than the typical TOF. In conclusion, the histogram practically shows the number of atoms versus their TOF.

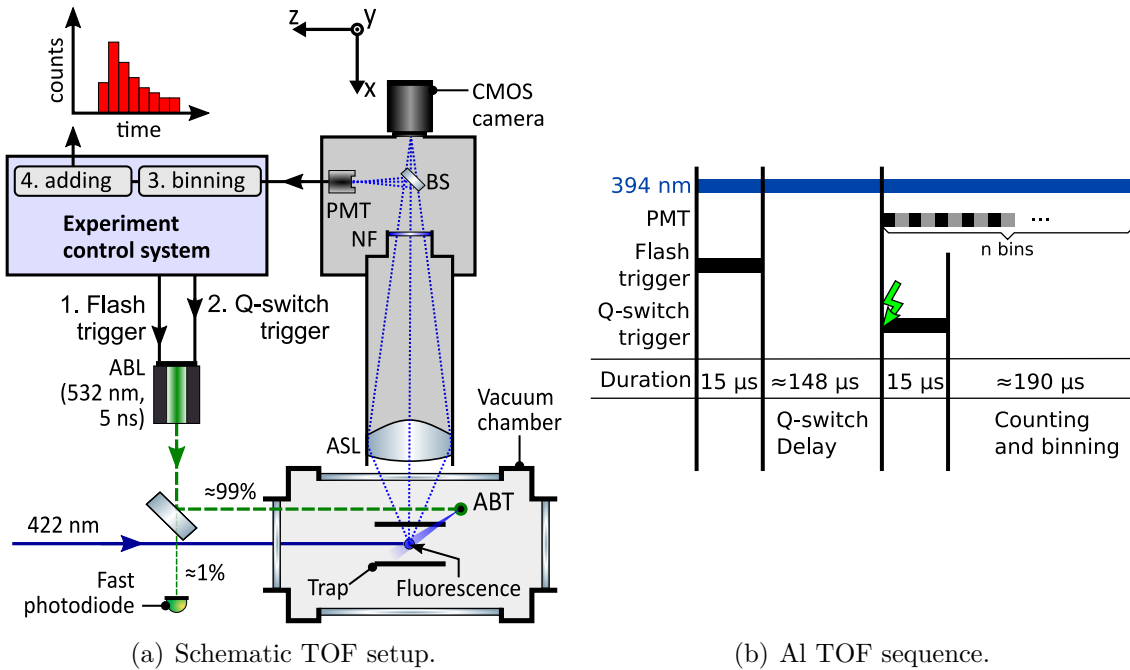


Figure 3.17.: Schematic setup and sequence for a time of flight measurement in the physics package introduced in Fig. 3.7. The experiment control systems triggers the ablation laser (ABL) flash lamp and after a delay the Q-switch, resulting in a laser pulse on the rising edge of the second trigger, marked by the green flash symbol. Then the fluorescence light counts registered by the photon multiplier tube (PMT) are binned in time. The binned counts are added up, while the sequence is repeated several times. ABT: ablation target, ASL: aspheric lens, BS: beam-splitter, NF: notch filter. Some components in the figure are adapted from [Franzen, 2009].

### Scanning the aluminum ionization laser frequency

During the first TOF measurement series, histograms for different aluminum ionization laser frequencies were recorded, while all other parameters of the experiment were kept constant. Fig. 3.18 shows the obtained result. The global maximum in fluorescence was measured at a TOF of approximately  $30\ \mu\text{s}$  for a detuning of 6 GHz, which equals 759.907 THz in absolute frequency with an FWHM of about 5 GHz. The histogram shows a pattern of horizontal stripes which are separated by approximately 2 GHz each. These are probably a result of the hyperfine structure of  $^{27}\text{Al}$ . For a more extensive treatment of this topic, the reader is referred to [Guggemos, 2016]. Moreover, for a detuning of 9.5 GHz, the number of ionized fast atoms starts to drop compared to smaller detunings, while the number of slow atoms at least remains constant. This indicates that a large detuning could increase the probability for loading a rather slow  $^{27}\text{Al}^+$  ion that crystallizes quickly.

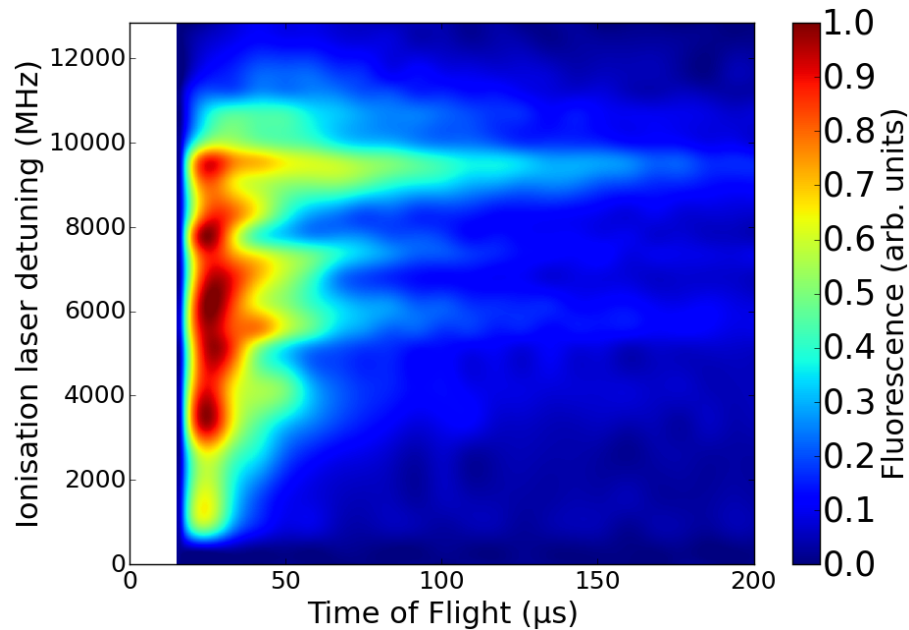


Figure 3.18.: Fluorescence vs TOF and ionization laser frequency.

### Scanning the ablation laser power

During the second measurement series, the ablation laser power was scanned for a constant ionization laser frequency of 759.908 05 THz. All other parameters remained unchanged. Fig. 3.19 shows that the total amount of excited aluminum atoms is pulse energy dependent. To determine the origin of the vertical stripe at about 10  $\mu\text{s}$ , the ionization laser was blocked during TOF measurements on trial. Since the stripe did not vanish, it cannot be caused by fast unexcited neutral atom fluorescence. One possible explanation is light emission from the trap caused by the impact of photoelectrons generated by the ablation laser. The first atoms are detected for a Q-switch delay of about 102  $\mu\text{s}$ , and the total histogram does not change for Q-switch delays of more than 125  $\mu\text{s}$ . At about 130  $\mu\text{s}$  Q-switch delay the number of atoms arriving at a TOF of more than 100  $\mu\text{s}$  has reached its maximum, while the fast atoms have not. Therefore, this setting could be favorable to increase the probability of loading a slow atom.

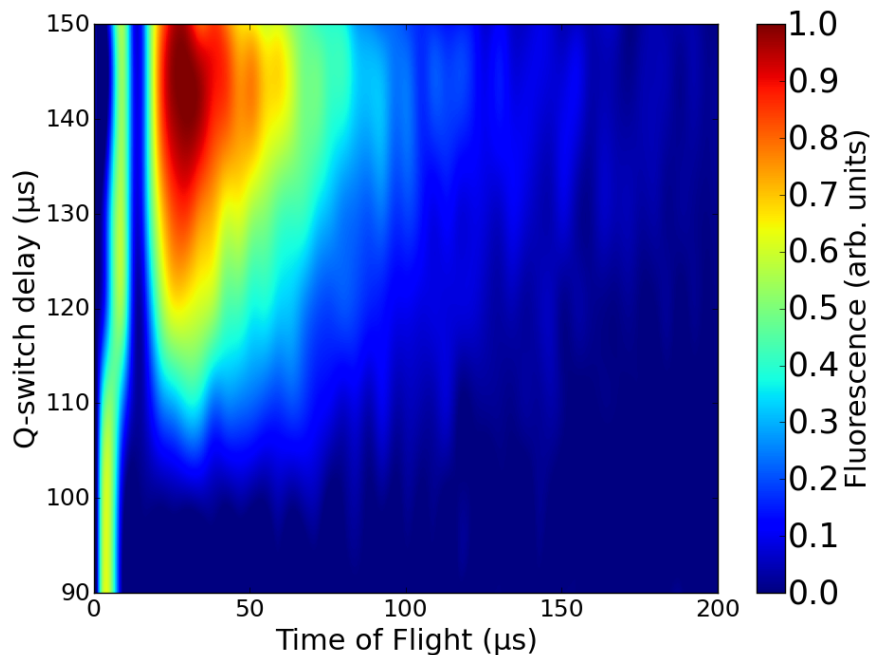


Figure 3.19.: Fluorescence vs TOF and ablation laser power (set via Q-switch delay).

#### Scanning the ablation target bias voltage

To avoid the capture of fast  $^{27}\text{Al}^+$  ions or ions of other species that are generated directly at the target by the ablation laser pulse, a negative bias voltage can be applied to the ablation target and its aperture. To test the effect of this measure a variable bias voltage is applied to the ablation target, which was grounded during the measurements previously described. Fig. 3.20 shows the measured fluorescence versus TOF for different bias voltages between  $-8\text{ V}$  and  $120\text{ V}$ , while all other parameters were kept constant. The distribution of fluorescence counts as function of the TOF does not change significantly when the target bias voltage is varied. This demonstrates that at least the vast majority of the aluminum atoms is excited by the photoionization light and not by electrons or ions that could be emitted from the ABL during ablation. This is important, because otherwise it would not be possible to select a certain velocity class of aluminum atoms by pulsing the ionization light synchronous to the ablation laser, which will be discussed in Sec. 3.10.3.

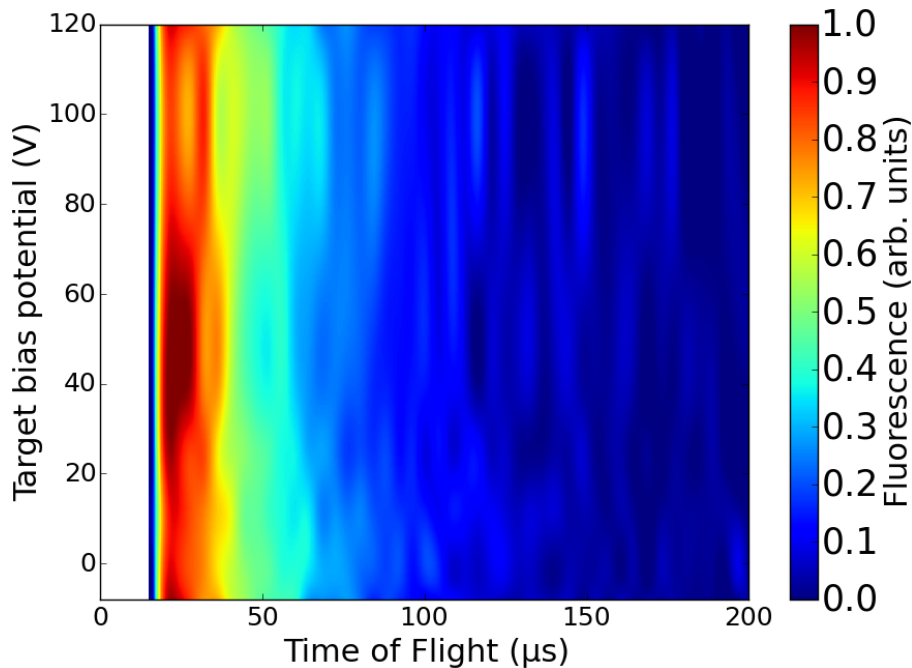


Figure 3.20.: Fluorescence vs. TOF and target bias potential, scaled to the global maximum value. For technical reasons, no fluorescence counts were recorded during the first  $15\text{ }\mu\text{s}$  TOF.

### Scanning across the ablation target

Up to here, the ablation laser spot position on the target has been kept constant. But is conceivable that the atom flux through the trap center also depends on it. The vertical coordinate of the ideal ablation laser spot position on target is defined by the apparatus via the aperture hole and the trap chips, which form a horizontal slit. Therefore, only the horizontal position will be altered here. Fig. 3.21(a) shows TOF spectra obtained for different ABL spot positions, which are depicted in Fig. 3.21(b). The measurements shows a gain in fluorescence, when the aluminum is ablated relatively far from the calcium target. Moreover, a drop by about 50% is observed for position 0.25, which coincidences with the edge of the groove.

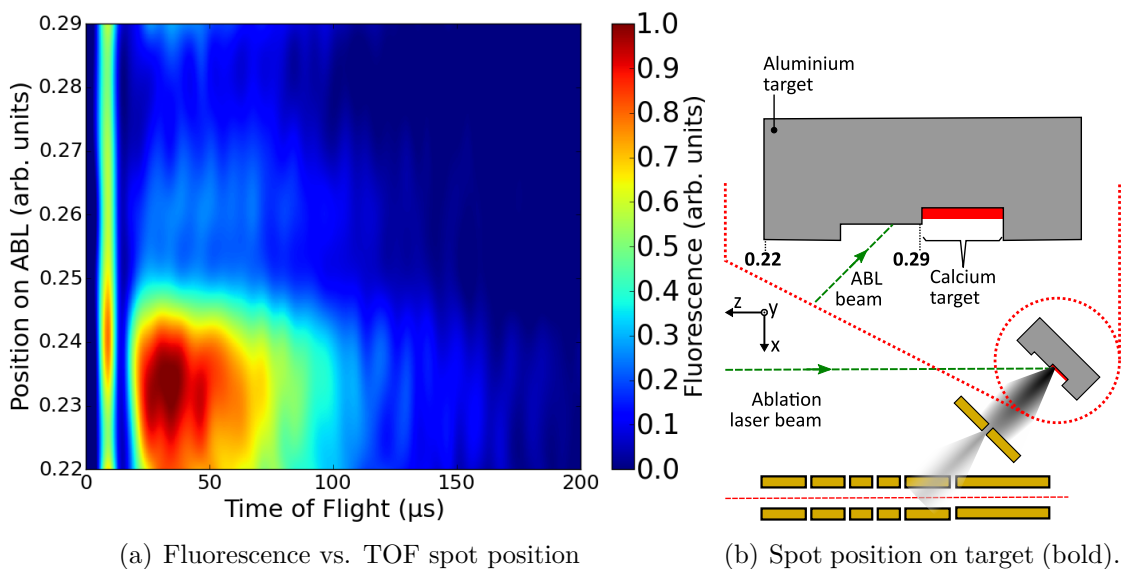


Figure 3.21.: Neutral Al atom fluorescence counts vs. TOF and horizontal ablation laser spot position on the target. a.) shows the result, while the two most extreme positions of the ABL spot on the aluminum target are depicted in b.)

### Conclusion of the aluminum TOF measurements

For reliable generation of a small number of neutral Al atoms, the 394 nm aluminum ionization laser frequency was set to 759.908 05 THz and the Q-switch delay of the ionization laser to 105 μs. As mentioned before, the ablation laser is capable of ionizing calcium atoms. Due to the low repetition rate compared to the atoms' flight time from the ABT to the trap center, this process has to take place at the

### 3. Transportable aluminum optical clock setup

ABT. This implies that the ablation laser can potentially create ions of elements that are either part of the target alloy or deposit on the target. To prevent trapping of such ions, a  $-8\text{ V}$  bias potential is applied to the ablation target<sup>30</sup>. Fig. 3.22(a) shows the aluminum TOF spectrum measured at the center of the loading zone for these settings and Fig. 3.22(b) the corresponding velocity distribution. The initial peak in the TOF spectrum seems to resemble the velocity distribution measured by Guggemos et al.[Guggemos et al., 2015] with a peak at  $4500\text{ m s}^{-1}$ , while the majority of the Al atoms observed here is found in a second peak and reaches only approximately  $485\text{ m s}^{-1}$  [Hannig et al., 2018b].

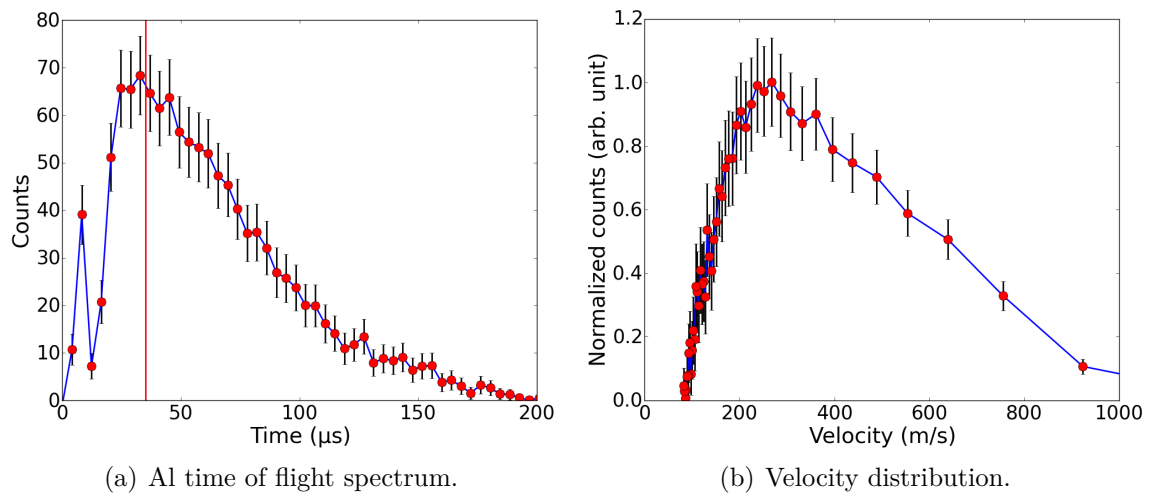


Figure 3.22.: (a): neutral Al atom time of flight spectrum measured at the center of the loading zone. The counts are binned in  $2\text{ }\mu\text{s}$  time frames and the errorbars show the statistical error per bin. The blue line links the data points as guide to the eye and red vertical line marks the chosen start time of the photoionization pulse at  $35\text{ }\mu\text{s}$  for  $^{27}\text{Al}^+$  loading. From [Hannig et al., 2018b]. (b): derived velocity distribution of the large second peak in (a).

<sup>30</sup>The value of the bias potential is restricted to an interval of  $(-8, +120)\text{ V}$ , since it is provided by the dc voltage source presented in Sec. 3.3. In principle higher absolute values are possible without changing the physics package.



### 3.10.3. Aluminum ion trapping

Most of the content presented in this subsection has been part of a publication by the author of this thesis [Hannig et al., 2018b]. For simplicity, individual citations in the main text are omitted.

While ablation loading of  $\text{Ca}^+$  is relatively straight forward due to the comparatively low neutral atom velocities and direct laser cooling right after ionization, ablated Al atoms are much faster and have to be cooled sympathetically which can take on average 600 s until crystallisation occurs [Guggemos et al., 2015]. One way to possibly reduce the crystallization time of an ion is to lower its initial kinetic energy, i.e. by velocity selective ionization of neutral atoms.

For  $\text{Al}^+$  loading, the 394 nm beam is shuttered with a single pass AOM synchronized to the ablation laser pulse to select a slow velocity class of neutral atoms via TOF selection in order to reduce the crystallization time. The loading sequence is depicted in Fig. 3.23, starting from a Doppler-cooled and crystallized  $\text{Ca}^+$  ion in the

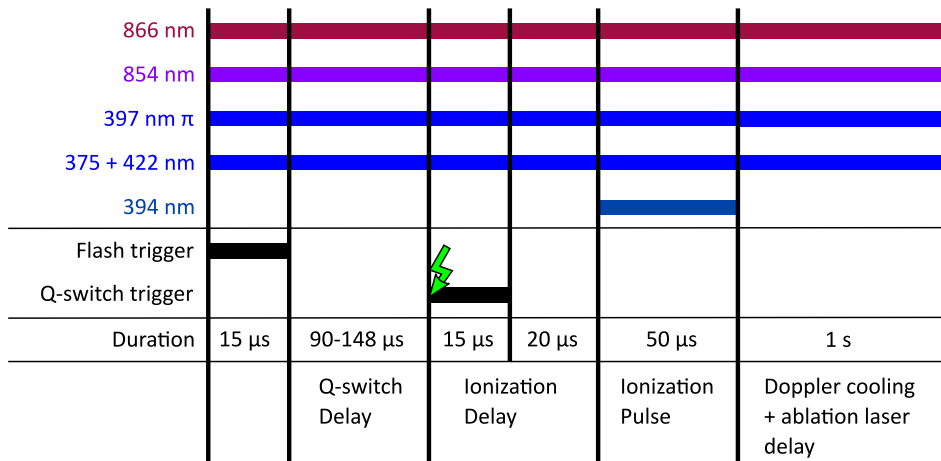


Figure 3.23.:  $^{27}\text{Al}^+$  loading sequence. The  $^{40}\text{Ca}^+$  ion is Doppler cooled during the entire sequence. First, the ablation laser flash lamp and its Q-switch are triggered by the experiment control system. The intermediate delay sets the maximum instantaneous power. At the rising edge of the Q-switch trigger pulse, the 5 ns long ablation laser pulse is fired (green flash symbol). After a second delay, the resonant Al ionization laser is unblocked to selectively ionize relatively slow atoms. Synchronously, the cooling laser power is ramped up to increase the probability of driving the non-resonant second ionization step. For this purpose, the Ca ionization lasers are manually switched on during the entire loading sequence. The sequence concludes with a waiting time for the next available pulse of the ablation laser. From [Hannig et al., 2018b].

### 3. Transportable aluminum optical clock setup

loading zone of the trap. First, the ablation laser flash lamp is triggered and after a delay, which can be adjusted to set the maximum instantaneous power of the pulse, a second trigger activates the Q-switch and therefore fires the ablation laser pulse (green flash symbol). After an additional delay starting with that pulse, the 394 nm laser is switched on for velocity selective Al ionization. A 1 s long Doppler cooling pulse follows to prevent exceeding the maximum repetition rate of the ablation laser in case multiple ablation shots are going to be fired. In order to increase the probability of successfully driving the non-resonant second step of the Al photoionization, both  $\text{Ca}^+$  ionization lasers are applied during the entire loading sequence.

The total kinetic energy of an Al atom before and right after ionisation consists of different contributions, whose calculated dependencies from the position of ionization inside the trap are shown in Fig. 3.24. The initial kinetic energy of a neutral atom arriving 35  $\mu\text{s}$  (10  $\mu\text{s}$ ) after the ablation laser pulse is shown by the solid (dashed) blue curve. Comparing the latter yields that setting a photoionization delay of 35  $\mu\text{s}$  reduces the maximum kinetic energy of the neutral atoms by more than one order of magnitude to 0.033 eV, while still more than 70% of the atoms are selected for ionisation, cf. Fig. 3.22. The volume in the loading zone, where the photoionization of a neutral Al atom takes place, is defined by the spatial overlap of the axial Al ionization lasers, as depicted in the insert. Its extent defines the maximum potential energy the atom gains by ionization displaced from the trapping potential minimum. The main figure shows the position dependence of the potential energy in axial direction as solid (dashed) red curve for  $\omega_{z,\text{Ca}^+} = 2\pi \times 0.25 \text{ MHz}$  ( $\omega_{z,\text{Ca}^+} = 2\pi \times 1.5 \text{ MHz}$ ) and for a radial displacement as the solid (dashed) green curve for  $\omega_{\text{rad},\text{Ca}^+} \approx 2\pi \times 0.52 \text{ MHz}$  ( $\omega_{\text{rad},\text{Ca}^+} \approx 2\pi \times 2 \text{ MHz}$ ). The potential energy gained due to a displacement from the trap center of less than 50  $\mu\text{m}$  in standard trapping configuration (dashed red and green curve) is already higher than the neutral atom kinetic energy. But for the relaxed trap, the potential energy as a function of the radial displacement remains below the initial kinetic energy for the entire ionization laser beam cross section, as illustrated by the vertical dashed black line indicating the waist of this beam. Therefore, the total energy of  $^{27}\text{Al}^+$  right after ionization is dominated by the axial displacement of ionization from the trap center.

Before each loading attempt, the trap was emptied and a single  $^{40}\text{Ca}^+$  ion was loaded. The latter was verified not only by the sCMOS camera image, but also by measuring the axial motional mode frequency via parametric excitation by applying

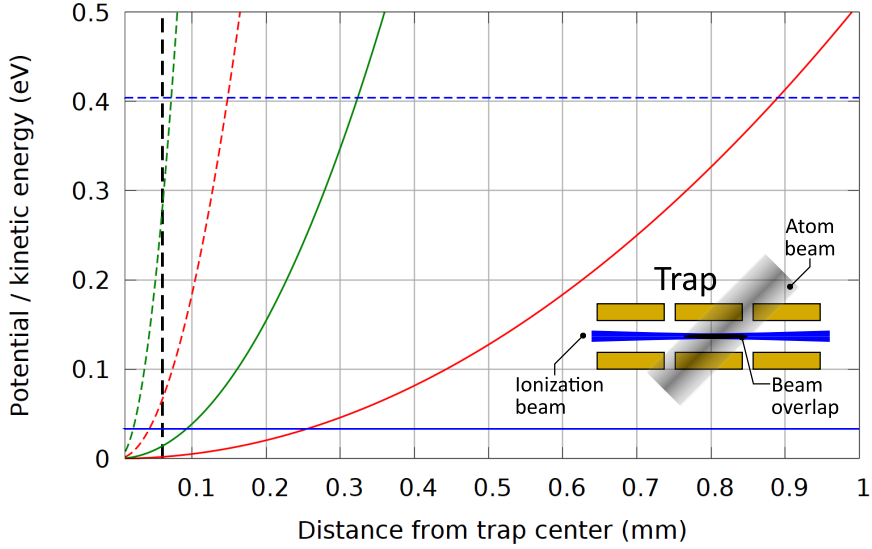


Figure 3.24.: Calculated energy of a  $^{27}\text{Al}^+$  ion as function of the ionisation position in the trap. The horizontal solid (dashed) blue line indicates the kinetic energy of a neutral atom arriving  $35\ \mu\text{s}$  ( $10\ \mu\text{s}$ ) after the ablation laser pulse. The solid (dashed) red curve shows the potential energy of  $^{27}\text{Al}^+$  as function of the axial displacement for  $\omega_{z,\text{Ca}^+} = 2\pi \times 0.25\ \text{MHz}$  ( $\omega_{z,\text{Ca}^+} = 2\pi \times 1.5\ \text{MHz}$ ) and the solid (dashed) green curve for  $\omega_{\text{rad},\text{Ca}^+} \approx 2\pi \times 0.52\ \text{MHz}$  ( $\omega_{\text{rad},\text{Ca}^+} \approx 2\pi \times 2\ \text{MHz}$ ). The vertical dashed black line indicates the waist of the ionisation light beam from the LMA fiber, which restricts the volume where ionisation takes place, cf. the trap cross section in the inset. From [Hannig et al., 2018b].

a resonant ac potential to an axially neighboring electrode of the loading zone. For each of the loading attempts, a video of the  $^{40}\text{Ca}^+$  ion was taken using the sCMOS camera to determine the crystallization time of  $^{27}\text{Al}^+ / ^{40}\text{Ca}^+$ , i.e. the time between the ABL pulse and the crystallization of the crystal. After a dark ion appeared such as shown in Fig. 3.25(a), the axial frequencies of the two ion crystal were measured using the resonant excitation method to verify that  $^{27}\text{Al}^+ / ^{40}\text{Ca}^+$  was trapped, cf. Equ. (2.15). Fig. 3.25(b) shows the results.

For the relaxed trap an average crystallization time of  $(231 \pm 102)\ \text{s}$  between the ablation laser pulse on the Al target and the formation of an  $^{27}\text{Al}^+ / ^{40}\text{Ca}^+$  crystal was measured, where the uncertainty is given under the assumption of normally distributed loading times. This is roughly a factor of 2.5 shorter than the value reported for the same combination of species by [Guggemos et al., 2015], who worked at higher trap frequencies of  $\omega_{\text{rad},\text{Ca}^+} \approx 2\pi \times 2\ \text{MHz}$  and  $\omega_{z,\text{Ca}^+} \approx 2\pi \times 0.4\ \text{MHz}$ .

### 3. Transportable aluminum optical clock setup

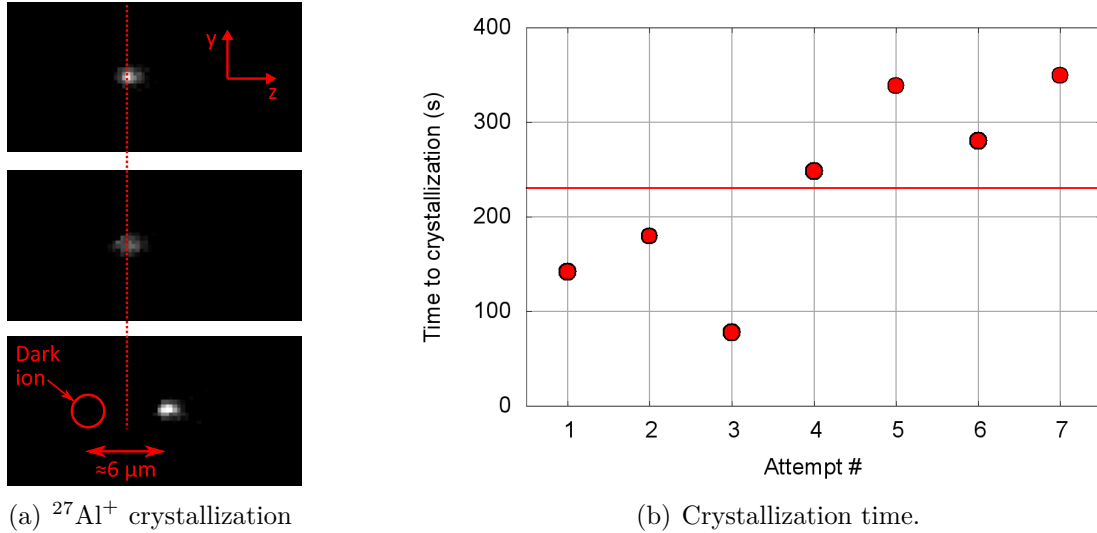


Figure 3.25.:  $^{27}\text{Al}^+$  loading. (a): Crystallization of  $^{27}\text{Al}^+ / ^{40}\text{Ca}^+$ . Top image: single  $^{40}\text{Ca}^+$ , middle: hot  $^{40}\text{Ca}^+$  about 1 s before crystallization of  $^{27}\text{Al}^+ / ^{40}\text{Ca}^+$ , bottom: crystallized  $^{27}\text{Al}^+ / ^{40}\text{Ca}^+$ . (b): Crystallization times for  $^{27}\text{Al}^+$ . The measurement errors are too small to be depicted.

## 3.11. Experimental control system

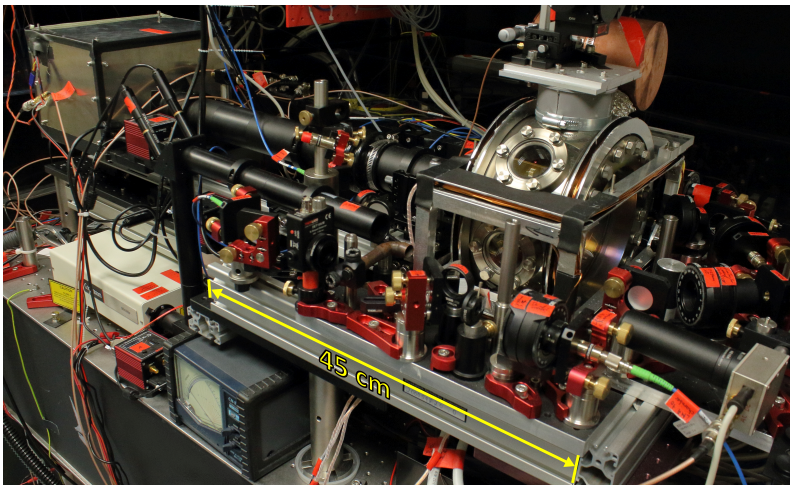
The operation of an optical clock requires the synchronized application of well-defined laser pulses in terms of frequency, power, start time, and stop time. The latter requirements also hold for processing of fluorescence count signals. Here, the experimental sequences are written as python script on a control computer. On the same machine parameters like pulse durations are set in a Labview<sup>31</sup> program that originally stems from the Innsbruck group and has been refined and adapted by the PTB group. The python scripts are compiled to machine code, including the parameters set in the Labview program and then sent to and executed on a FPGA system, developed by [Pham, 2005], that generates rf signals via direct digital synthesizer (DDS), implemented by [Schindler, 2008]. Both, the 100 MHz FPGA clock and the 800 MHz DDS clock are referenced to a 10 MHz maser. The amplified outputs of the DDS boards drive the aforementioned AOMs that shutter the lasers, adjust their power and shift their frequencies. Input signals are digitized using ADC cards<sup>32</sup>. The same cards also provide TTL outputs that e.g. control the motorized shutters.

<sup>31</sup>National Instruments®

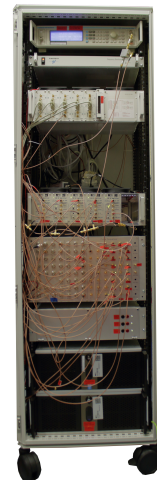
<sup>32</sup>National Instruments 6703 and 6733

## 3.12. Transportability

To enable frequency comparison campaigns outside the laboratory and chronometric leveling in the field, the entire optical setup explained up to this point plus the  $^{27}\text{Al}^+$  laser systems have to be integrated into a transportable unit. Therefore, the complete  $^{40}\text{Ca}^+$  laser system has been set up on three rigid  $0.9 \times 0.6 \text{ m}^2$  breadboards with honeycomb core, which are interconnected via optical fibers and therefore form a modular system. Together with up to three breadboards containing the aluminum laser systems similar to that described in Chap. 5, these will form a stack of approximately  $1.3 \times 0.9 \times 1.0 \text{ m}^3$  size. A  $1.3 \times 0.6 \text{ m}^2$  table-top breadboard holding the physics package shown in Fig. 3.26(a) will be installed on top of the stack. A standard 19"-rack shown in Fig. 3.26(b) contains the experiment control PCs, FPGA-System, dc voltage source, rf amplifiers and frequency generator in a volume of  $0.7 \times 0.6 \times 1.9 \text{ m}^3$ . All the controllers for the various lasers fit in a second rack of that size. These three units will be installed in a standardized cooled 20 foot container, which is depicted in Fig. 3.27. It will also contain the reference cavities for the  $^{40}\text{Ca}^+$  logic and  $^{27}\text{Al}^+$  clock laser on a vibration-isolation platform, two computer workstations for the system operators, and storage space for lab equipment.



(a) Physics package.



(b) Rack.

Figure 3.26.: (a): Photo of the physics package showing the vacuum vessel on the right and the imaging system on the left. The footprint of the system is  $1.3 \times 0.6 \text{ m}^2$ . From [Hannig et al., 2018b]. (b): 19"-rack with (top to bottom): rf frequency generator, frequency distribution amplifier, dc voltage source, rf amplifiers, experiment control system (2 units), and two PCs.

### 3. Transportable aluminum optical clock setup

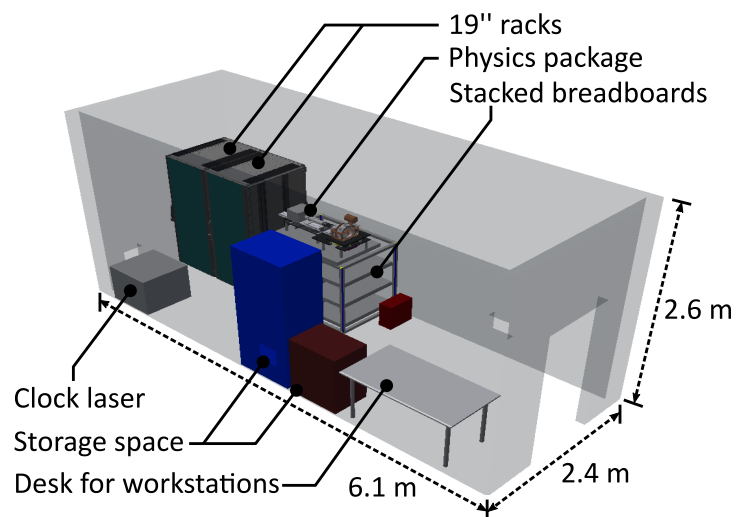


Figure 3.27.: Schematic inner layout of the clock-container. Adapted by kind permission of L. Pelzer.







## 4. Measurements

*A major fraction of the content presented in this chapter is part of a publication by the author of this thesis [Hannig et al., 2018a]. For simplicity, individual citations in the main text are omitted.*

In the previous chapter, the components of the clock setup were presented and their individual performance was evaluated. Here, the complete system is characterized, starting with the heating rates and the mean motional quantum numbers after pulsed sideband cooling to the ground state. Afterwards, excess micromotion is minimized and the apparatus-related partial error budget of an  $^{27}\text{Al}^+$  ion quantum logic optical clock operated in the setup is estimated.

The following experiments on a single  $^{40}\text{Ca}^+$  ion were conducted with approximately 2.2 W rf drive power, which yields radial secular frequencies  $\omega_{\text{rad},1} = 2\pi \times 2.65$  MHz and  $\omega_{\text{rad},2} = 2\pi \times 2.42$  MHz. The axial confinement in the 1 mm long experiment zone resulted in a secular frequency of  $\omega_{\text{ax}} = 2\pi \times 1.64$  MHz.

### 4.1. Laser cooling

An ion confined in a rf trap is subject to thermal secular motion inside the pseudo potential, cf. Eq. (2.11). Since the second order Doppler shift on the  $^{27}\text{Al}^+$  clock transition is a significant contribution to the error budget, as will be discussed in Sec. 4.3, cooling of the ion's motion is necessary. In the first cooling stage, Doppler cooling is required to reach the Lamb-Dicke regime, where the recoil of scattered photons is absorbed by the trap and therefore does not lead to a random walk of the ion. For the  $^{40}\text{Ca}^+$  Doppler temperature of approximately 0.5 mK, the resulting fractional second order Doppler shift on  $^{27}\text{Al}^+$  is larger than  $1 \times 10^{-17}$  and therefore would be the dominating shift, as will be shown in this chapter. Ground state cooling severely reduces the ion's kinetic energy and therefore the second order Doppler shift. Moreover, quantum logic spectroscopy requires ground state cooling of the motional mode used to transfer the internal state of the clock ion to that of

## 4. Measurements

the logic ion [Schmidt et al., 2005]. In the experiments presented in this thesis, a combination of techniques has been employed to cool the ion down to the motional ground state, i.e.  $\bar{n} \ll 1$ . In the next subsections, Doppler cooling on a transition much broader than the secular frequencies ( $\gamma \gg \omega$ ) will be explained, followed by sideband cooling in the opposite regime. Afterwards, the experimental results of pulsed sideband cooling are presented.

### 4.1.1. First stage: Doppler cooling

Doppler cooling is a commonly used method for laser cooling of trapped ions. It is based on the well-known Doppler effect: if a receiver moves relative to the emitter of a periodic signal, the period measured by the receiver differs from that measured in the emitter's reference frame. This can be employed for laser cooling as proposed by [Wineland and Dehmelt, 1975, Hänsch and Schawlow, 1975] and demonstrated by [Wineland et al., 1978], when the cooling laser is red detuned from a sufficiently broad atomic transition. If an ion in the internal ground state moves antiparallel to the  $k$ -vector of the laser, the laser is blue detuned in its reference frame and therefore can be on resonance with the transition, resulting in photon absorption and therefore momentum transfer against the direction of motion. When the excited ion decays back to the ground state, it emits a photon. Since the direction of the emitted photons follows a dipole emission pattern, a net momentum transfer against the momentary direction of motion is achieved for a large number of scattering events. This reduces the kinetic energy of the ion and therefore  $\bar{n}$ . In order to achieve cooling of all motional normal modes, the projection of the cooling laser's  $k$ -vector on the corresponding directions has to be non-zero. Moreover, the mode frequencies must not to be degenerate, since otherwise motion perpendicular to the cooling laser could evolve. In practice, compensation voltages are applied to alter the radial mode splitting to achieve this goal, cf. Fig. 3.4.

However, the minimum temperature achievable with Doppler cooling is limited, since the emission of photons results in a random walk of the ion with non-zero average velocity. The lowest temperature achievable with pure Doppler cooling  $T_{\text{Doppler}}$  at the equilibrium of this heating process and the corresponding Doppler cooling rate is [Wineland and Itano, 1979]:

$$T_{\text{Doppler}} = \frac{\hbar\gamma}{2k_B}, \quad (4.1)$$

with the reduced Planck's constant  $\hbar$ , the linewidth of the cooling transition  $\gamma$ , and Boltzmann's constant  $k_B$ . For  $^{40}\text{Ca}^+$  and its 22.4 MHz broad 397 nm cooling transition, this yields a theory value of  $T_{\text{Doppler}} = 0.57 \text{ mK}$ , which equals  $\bar{n} \approx 12$  for a secular frequency  $\omega = 2\pi \times 1 \text{ MHz}$ . It has to be stressed that selecting a much narrower transition for Doppler cooling on the one hand reduces the reachable  $T_{\text{Doppler}}$ , but on the other hand also reduces the scattering rate and therefore increases the cooling time required to reach a certain temperature.

### 4.1.2. Second stage: Sideband cooling

With Doppler cooling described in the previous section high cooling rates are achievable by employing a broad cooling transition, which obviates preparing the ion in its motional ground state. The latter is reached by subsequent cooling with the sideband technique presented here. The implementation of ground state cooling requires to operate the system in the Lamb-Dicke regime, cf. Sec. 2.3, and resolved sideband regime ( $\omega \gg \gamma$ ), where the linewidth of the cooling transition is much smaller than the frequency of the motional mode to be cooled. In this case, the transition splits up into a carrier (CAR), on which photon scattering does not alter the motional quantum number, and a red (blue) sideband (RSB/BSB), where it is reduced (increased) by one. A narrow cooling laser can exclusively drive the RSB and therefore extract phonons from the system, as depicted in Fig. 4.1(a). Although the motional ground state is reachable, the cooling rate is very low due to the long lifetime of the upper state, cf. Fig. 2.8. To circumvent this drawback, the upper state is usually pumped to a short-lived auxiliary state  $|\text{aux}\rangle$ , which virtually broadens the cooling transition  $|\downarrow, n\rangle \rightarrow |\uparrow, n-1\rangle$ . This technique is called *quenching* (QU in Fig. 4.1(b)) and can increase the cooling rate by orders of magnitudes.

Beside the key advantage of reaching the ground state, sideband cooling has the disadvantages of lower cooling rates than Doppler cooling, even when quenching is employed. Moreover, every motional mode requires individual sideband cooling settings, which prolongates the cooling time compared to other state of the art ground state cooling techniques such as double bright EIT cooling, which allows for simultaneous cooling of several motional modes of an  $^{27}\text{Al}^+ / ^{40}\text{Ca}^+$  crystal [Scharnhorst et al., 2017]. However, it requires phase coherence between lasers at different wavelengths and therefore a frequency comb or stable reference cavities, which is not part of the transportable clock setup presented in this thesis. But single EIT cooling employing only the 397 nm laser does not require a frequency comb. It allows for

#### 4. Measurements

cooling of both two radial modes with the same laser settings and therefore promises a reduced cooling time compared to sideband cooling.

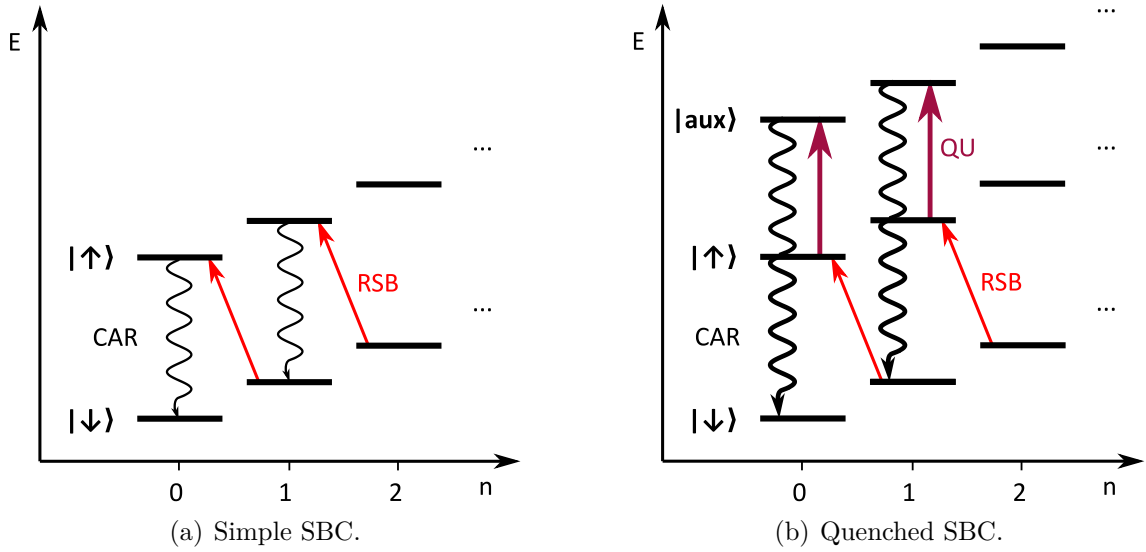


Figure 4.1.: Sideband cooling scheme, energies not to scale. a): In the resolved sideband regime the secular frequencies are much larger than the linewidth of the cooling transition ( $\omega \gg \gamma$ ). Therefore, the red sideband (RSB) can be resolved. Since the excited state most likely decays on the carrier (CAR), cooling is achieved (b). The cooling rate is increased by pumping the long-lived excited state to a short-lived auxiliary state  $|\text{aux}\rangle$  with a quench-laser (QU).

#### 4.1.3. Experimental implementation of ground state cooling

Following the approach by [Roos et al., 1999], who implemented sideband cooling on the 729 nm transition of  $^{40}\text{Ca}^+$  for the first time, typical radial (axial) trap frequencies of  $\omega_{\text{rad,Ca}^+} \approx 2\pi \times 2.5 \text{ MHz}$  ( $\omega_{\text{ax,Ca}^+} \approx 2\pi \times 1.5 \text{ MHz}$ ) and an angle of  $60^\circ$  ( $45^\circ$ ) between the motional mode to be cooled and the 729 nm beam yield Lamb-Dicke factors  $\eta_{\text{rad}} \approx 0.04$  and  $\eta_{\text{ax}} \approx 0.06$ . Fig. 4.2 shows the substructure of the 729 nm line due to Zeeman splitting and motional sidebands as function of the magnetic field at the ion position. In order to avoid accidental heating during sideband cooling due to overlapping of RSBs and BSBs that belong to different carriers, the  $|S_{1/2}, m_j = -1/2\rangle \leftrightarrow |D_{5/2}, m_j = -5/2\rangle$  transition has been chosen for cooling and a field strength between 180 and 250  $\mu\text{T}$  has been applied (yellow square). Moreover, the  $|D_{5/2}, m_j = -5/2\rangle$  state is repumped via  $|P_{3/2}, m_j = -3/2\rangle$ , which

only populates the initial state  $|S_{1/2}, m_j = -1/2\rangle$  and therefore ensures a closed cooling cycle, cf. Fig. 2.8.

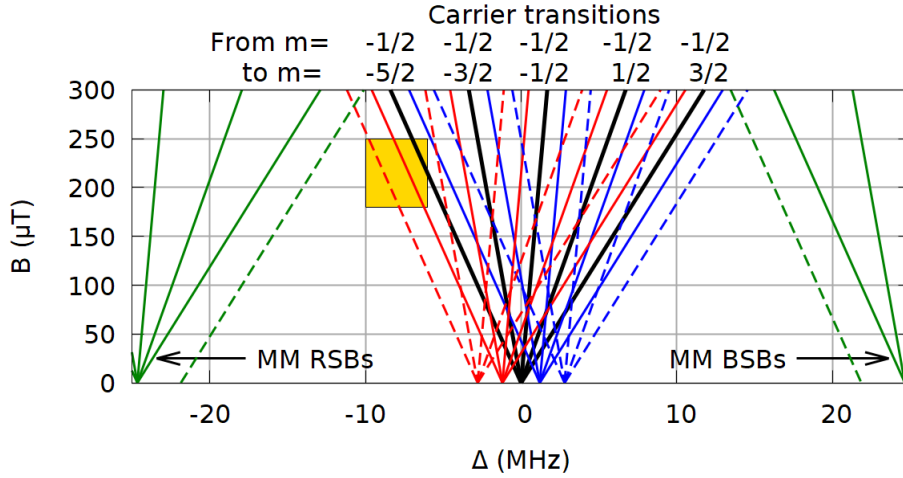


Figure 4.2.: Substructure of the 729 nm line due to Zeeman splitting in an external magnetic field  $B$  including the micromotion sidebands (green) and the sidebands due to secular motion (red/blue). Line overlapping can be avoided by selecting the  $|S_{1/2}, m_j = -1/2\rangle \leftrightarrow |D_{5/2}, m_j = -5/2\rangle$  transition and a field strength between 180 and 250  $\mu\text{T}$  for sideband cooling (yellow square).

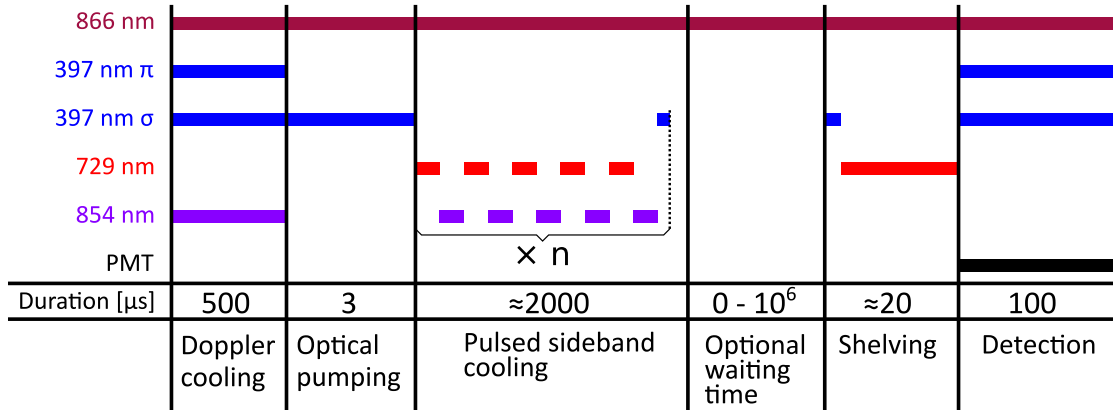


Figure 4.3.: Sideband cooling sequence. Colored lines represent active lasers. The optional waiting time is required for heating rate measurements. From [Hannig et al., 2018b].

Fig. 4.3 shows the experimental sequence starting with a 500  $\mu\text{s}$  long Doppler cooling pulse 10 MHz red detuned from the carrier, followed by 3  $\mu\text{s}$  optical pumping to the  $|^2S_{1/2}, m_g = -1/2\rangle$  ground state. Then a series of interleaved 729 nm RSB and 854 nm clearout pulses cools the ion near the motional ground state. The 729 nm

#### 4. Measurements

pulses are approximate RSB  $\pi$ -pulses for  $n = 1$  to  $n = 0$  on the  $\Delta m = -2$  transition. A  $3\ \mu\text{s}$  long optical pumping pulse after every fifth clearout pulse restores the preparation to the internal ground state  $|^2S_{1/2}, m_g = -1/2\rangle$ . An optional waiting time for heating rate measurements, electron shelving on the 729 nm transition, and a final state detection phase conclude the sequence.

Under the assumption of a thermal distribution of the motional states, the mean occupation number  $\bar{n}$  is determined from the excitation  $I_{\text{RSB}}$  ( $I_{\text{BSB}}$ ) of the first order red (blue) sideband [Monroe et al., 1995, Keller et al., 2015], both probed with the  $\pi$ -time of the blue sideband:

$$\bar{n} = \frac{1}{\frac{I_{\text{BSB}}}{I_{\text{RSB}}} - 1} \quad (4.2)$$

The motional quantum number was measured as a function of the number of sideband cooling pulses to reduce the latter to the minimum number necessary to reach a steady state of typically  $\bar{n} \approx 0.05$ .

For the heating rate measurements the waiting time  $t$  in the sideband cooling sequence was varied between 0 and 200 ms. A linear function was fit to the obtained  $\bar{n}(t)$  as shown in Fig. 4.4 for the axial mode. Tab. 4.1 summarizes the heating rates and separately measured obtained temperatures for all three motional modes. These results are the same order of magnitude as those presented by [Keller, 2015] measured in the same trap geometry with a single  $\text{Yb}^+$  ion.

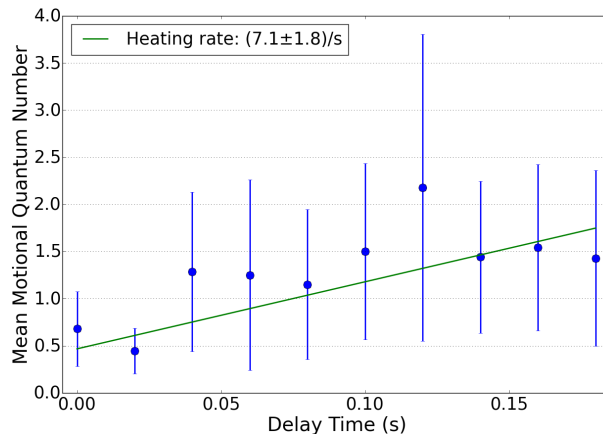


Figure 4.4.: Example for a heating rate measurement in axial direction. Shown is the average motional quantum number as a function of the waiting time in the sideband cooling sequence, cf. Fig. 4.3, and a linear fit to the data (green). The errorbars are derived from the statistical errors of the sideband excitation measurements. From [Hannig et al., 2018b].

Table 4.1.: Average motional quantum numbers and heating rates measured on a single  $\text{Ca}^+$  ion after pulsed sideband cooling to the ground state and micromotion compensation.

<b>Direction</b>	$\omega/2\pi$ (MHz)	$\bar{n}$	$\dot{n}$ ( $\text{s}^{-1}$ )
axial:	1.64	$0.06 \pm 0.02$	$7.1 \pm 1.8$
radial I:	2.42	$0.04 \pm 0.03$	$5.7 \pm 0.9$
radial II:	2.65	$0.13 \pm 0.08$	$7.1 \pm 3.2$

## 4.2. Excess micromotion compensation

Micromotion of ions induced by the confining rf-field causes second order Doppler shifts whose uncertainties can significantly contribute to the error budget of an optical clock, cf. Sec. 4.3.

In Sec. 2.2 it has been assumed that the trap was operated in an environment completely free of any other electromagnetic field. In practice, however, there is always some residual dc electric field  $\vec{E}_{\text{dc}}$  inside the trap, e.g. caused by patch charges on isolating parts of the trap structure. This dc field displaces the ion relative to the minimum of the pseudo potential as depicted in Fig. 4.5 (left). Therefore, the ion is exposed to the rf electric field, which exerts an periodic force on it and thereby adds *excess micromotion* (EMM) [Berkeland et al., 1998] to the aforementioned intrinsic micromotion, cf. Eq.(2.11):

$$\tilde{x}(t) \approx \left[ \underbrace{\tilde{x}_{\text{EMM}}}_{\text{EMM}} + \underbrace{2AC_0 \cos\left(\beta_x \frac{\Omega_{rf} t}{2}\right)}_{\text{secular motion}} \right] \left[ \underbrace{1 - \frac{q_x}{2} \cos(\Omega_{rf} t)}_{\text{micromotion}} \right], \quad (4.3)$$

with the new summand representing the excess micromotion [Berkeland et al., 1998]

$$\tilde{x}_{\text{EMM}} \approx \frac{Q\vec{E}_{\text{dc}}\vec{e}_{\tilde{x}}}{m\beta_x}, \quad (4.4)$$

where  $\vec{e}_{\tilde{x}}$  is the unit vector in  $\tilde{x}$ -direction. Since EMM is a driven motion, it cannot be cooled efficiently.

While intrinsic micromotion is an unavoidable feature of rf traps, EMM can be suppressed by design, i.e. a large ion-to-electrode distance reduces the electric field

#### 4. Measurements

contribution of patch charges at the trap center. To obtain less than  $1 \times 10^{-18}$  fractional second order Doppler shift due to EMM for an  $^{27}\text{Al}^+$  ion clock, the residual micromotion fields have to be kept below  $66 \text{ V m}^{-1}$  over an axial distance equal to the spatial extent of an  $^{27}\text{Al}^+ / ^{40}\text{Ca}^+$  crystal under typical operating conditions. Therefore, the trap wavers of the multi-layer trap have to be aligned on the  $10 \mu\text{m}$  and  $0.1 \text{ mrad}$  level [Herschbach et al., 2012]. Other crucial aspects of the trap assembly are the design of the rf electrodes and the rf wiring. The conductors for the trapping rf potentials have to be length- and capacity-matched to avoid a phase shift between the electrodes, which results in an rf potential without global constant minimum. Following [Berkeland et al., 1998], a required length-matching of  $\pm 0.1 \text{ mm}$  is estimated to keep the additional fractional second order Doppler shift below  $1 \times 10^{-18}$ .

When an ion trap has been built considering these aspects, the dominant source for EMM is an external electric field that displaces the ion from the minimum of the rf potential, as depicted in Fig. 4.5(a). A second pair of dc trap electrodes (Fig. 4.5(b), green) allows for full compensation of the external dc electric field in the radial plain by applying independent dc potentials on both electrode pairs. For micromotion compensation in the axial direction, the dc potentials for the axial confinement (cf. Fig. 2.3, dark red segments) need to be varied independently from each other to move the ions axially.

EMM compensation by applying dc fields requires either dc-field- or EMM measurements. Here, three techniques will be briefly discussed. A thorough treatment can be found in [Berkeland et al., 1998, Keller et al., 2015]. The first and most simple technique called *displacement monitoring* is based on the observation of the ion's position and focusing on the camera while the power of the trap drive and therefore the amplitude of the ac electric field is changed. It can be divided into the following steps:

1. Identification the position of the ion's image for a strong radial confinement and optimized focusing.
2. Reduction of the rf power.
3. Changing of the dc voltages while observing the position and focusing of the ion in a way that the initial parameters are restored.
4. Iteration of the three previous steps.



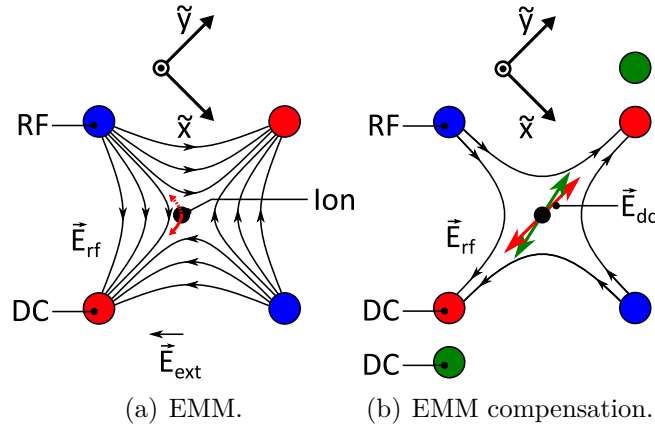


Figure 4.5.: Micromotion and its compensation in the radial plane of a linear Paul trap. If an external dc electric field  $\vec{E}_{\text{ext}}$  displaces the ion from the trap center defined by the rf drive field, excess micromotion occurs (a). The ion is shifted back to the trap center by adding a second pair of dc rods (green) and applying suitable voltages to the two dc electrode pairs (b), causing the excess micromotion to vanish.

While the technique is fast, addresses all three dimensions simultaneously, and can be implemented using standard components of the setup, it is not unambiguous and also inaccurate in the direction of the optical axis of the imaging system. Moreover, the finite resolution of the camera chip limits the accuracy in the plane parallel to it.

The second technique referred to as *photon correlation* is schematically depicted in Fig. 4.6(a). The ion is cooled close to the Doppler limit, cf. Eq. (4.1), employing a cooling laser with a linewidth much narrower than the linewidth of the cooling transition. The laser frequency is chosen such that it is on the red slope of the ionic line (blue). Any motion of the ion with a component parallel to the cooling laser results in a frequency modulation  $\Delta$  in its reference frame, which leads to a modulation of the absorption rate of cooling laser photons. Therefore, also the emission rate of fluorescence photons is modulated by  $(\Delta I)$ . In the case of EMM, which is periodic with the trap drive frequency, the fluorescence modulation can be detected by binning the fluorescence photon counts relative to the phase of the trap drive signal, cf. Fig. 3.3. EMM is reduced by alternating adjustments of the dc potentials and measurements of the modulation depth  $\Delta I$ . While the photon correlation method is an accurate quantitative method for a calibrated detection system, it only measures the EMM in the direction of the Doppler cooling laser beam

#### 4. Measurements

and therefore requires additional beams with linearly independent wave vectors for three dimensional micromotion compensation.

The third technique called *sideband spectroscopy* is schematically depicted in Fig. 4.6(b). The motion of the ion also modulates the logic laser frequency. Therefore, micromotion sidebands are imprinted on the logic transition.

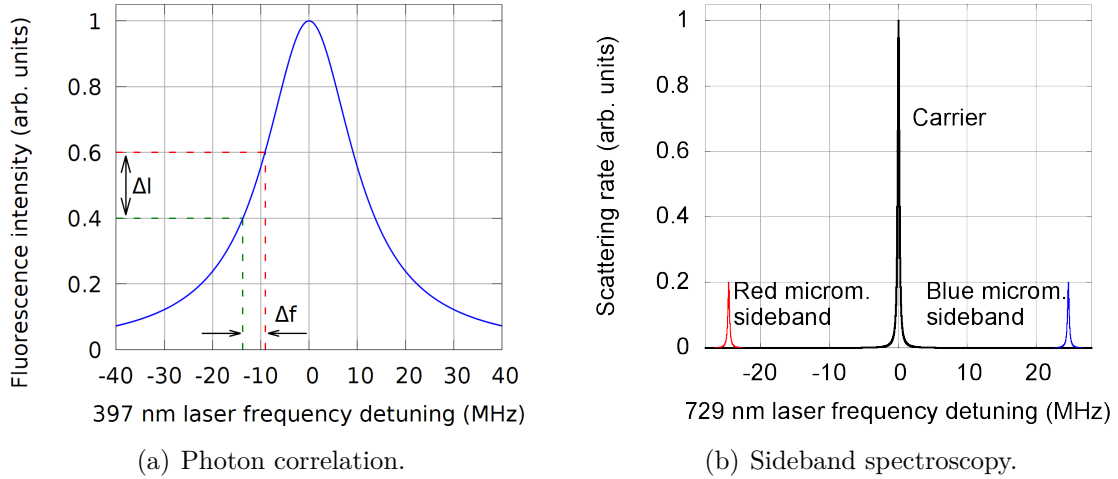


Figure 4.6.: Micromotion compensation methods. In the reference frame of the ion, micromotion results in a frequency modulation  $\Delta f$  of the cooling laser, which translates into a intensity modulation  $\Delta I$  of the fluorescence light, if the cooling laser is narrow and its frequency on the slope of the resonance curve (left). The frequency modulation in the ion's reference frame causes sidebands in the spectrum (right).

Here, the resolved-sideband method is employed for micromotion compensation, i.e. the ratio of the photon scattering rate on a micromotion sideband  $r_{\text{mmsb}}$  and carrier  $r_{\text{car}}$  is reduced. It is quantified by the *sideband modulation index* [Berkeland et al., 1998]

$$\beta_i \approx 2\sqrt{\frac{r_{\text{mmsb}}}{r_{\text{car}}}}, \quad (4.5)$$

which has to be minimized for three non-collinear 729 nm beams in direction  $i = x, y, z$ , cf. Fig. 3.12, because with every single beam only micromotion in the propagation direction of that beam can be detected. Firstly, a coarse minimization of the axial micromotion was performed by varying the voltages applied to the electrodes of the neighboring trap zones to reduce the excitation on the axial micromotion sideband. Subsequently, the voltages on the compensation electrodes in the 1.0 mm

long experiment zone were scanned during measurements of the modulation index for the vertical (y) and diagonal (xz) 729 nm beam. For each of the three 729 nm beams the rf field experienced by the ion in the corresponding direction has been derived from  $\beta$ , the ion mass  $m$ , the wavenumber  $k$  and the charge  $Q$  [Berkeland et al., 1998]:

$$E_{\text{rf},i} = \beta_i \frac{m\Omega_{\text{rf}}^2}{Qk}. \quad (4.6)$$

Fig. 4.7, a.) shows the assignment of the compensation voltages to the electrodes in the experiment zone. The measured fields are represented by filled dots in Subfig. b.) and c.). The background color depicts the result of fitting a v-shaped profile to the data. Since the two compensation directions are not orthogonal, cf. Fig. 4.5(b), a crossed line fit is required to find the point of lowest micromotion in the plane spanned by the vertical and diagonal 729 nm laser. In Subfig. d.) it is determined to be  $U_{ec} = (0.070 \pm 0.003) \text{ V}$ ,  $U_{tc} = (1.311 \pm 0.002) \text{ V}$  by intersecting the two resulting lines of minimum micromotion for the two directions. In the last step the axial compensation was repeated while the radial compensation voltages were kept constant, which yielded the field distribution shown in Fig. 4.8.

The residual rf fields at the trap center after micromotion compensation are listed in Tab. 4.2. An upper limit for the field in x-direction was inferred from the results in z and xz direction by assuming a phase of  $\pi$  between the two fields, the geometric sum of the fields in the trap center is  $(20.9 \pm 4.8) \text{ V m}^{-1}$ . Possible reasons for the non-vanishing rf-field are a finite phase between the two rf electrodes due to a length difference of the rf conductors or trap asymmetries arising from the limited alignment accuracy achieved during the assembly.

These findings agree within the uncertainties with the results obtained by [Pyka et al., 2014] for a single  $^{172}\text{Yb}^+$  ion in a trap of the same type, measured using the same technique.

For typical trap parameters, the two ions of an  $^{27}\text{Al}^+ / ^{40}\text{Ca}^+$  crystal are spaced  $4.3 \mu\text{m}$  apart from each other symmetrically around the minimum of the axial dc potential, cf. Eq. (2.17). When the dc potential minimum and the rf potential minimum do not coincide, the  $^{27}\text{Al}^+$  ion is exposed to a stronger rf field than in the rf minimum. However, Fig. 4.8 shows that the difference is smaller than  $10 \text{ V m}^{-1}$  and therefore does not substantially change the total rf field of  $(23.5 \pm 5.3) \text{ V m}^{-1}$  at the ion position, cf. Tab. 4.2.

#### 4. Measurements

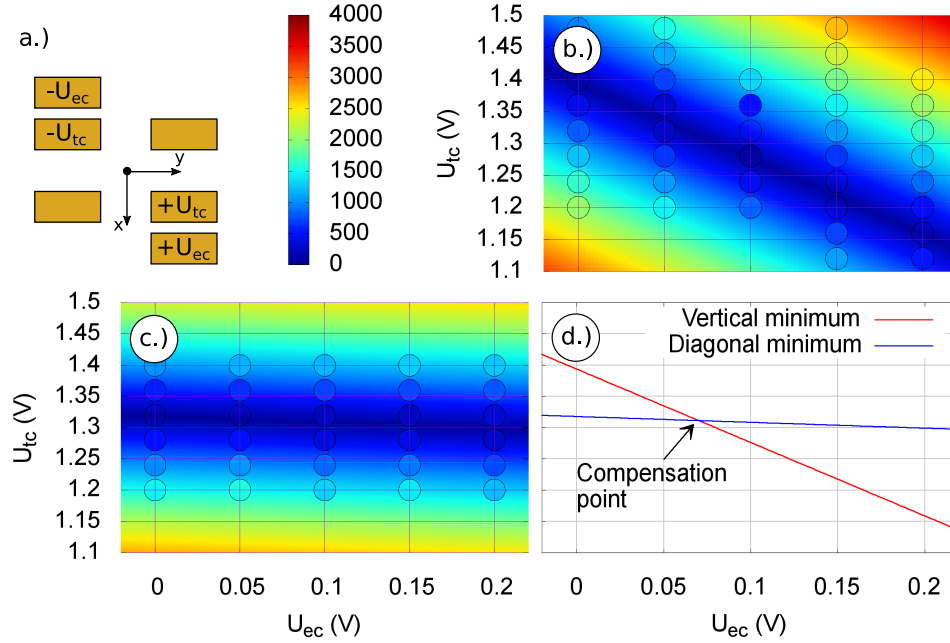


Figure 4.7.: Excess micromotion compensation in the plane defined by the vertical and diagonal 729 nm beam. a.) Schematic cross section of the trap showing the assignment of the voltages to the electrodes in the experiment zone. b.)/c.) vertical/diagonal rf field in  $\text{V m}^{-1}$  at the ion position as a function of the two compensation voltages. Filled dots represent the measured fields, the background depicts a v-shaped profile fit to the data. d.) Determination of the micromotion compensation point at the intersection of the two lines with minimum micromotion per direction. From [Hannig et al., 2018b].

Table 4.2.: Residual rf field at the trap center measured with a single  $\text{Ca}^+$  ion after excess micromotion compensation. The ion is sideband-cooled to the motional ground employing the same 729 nm beam as used for micromotion sideband spectroscopy.

Direction	$E_{\text{rf}}(\text{V m}^{-1})$
trap axis (z):	$7.1 \pm 1.6$
vertical (y):	$7.9 \pm 1.7$
diagonal (xz):	$9.8 \pm 3.0$
optical axis (x, calculated maximum):	$20.9 \pm 4.8$
geometric sum (from x, y, z):	$23.5 \pm 5.3$

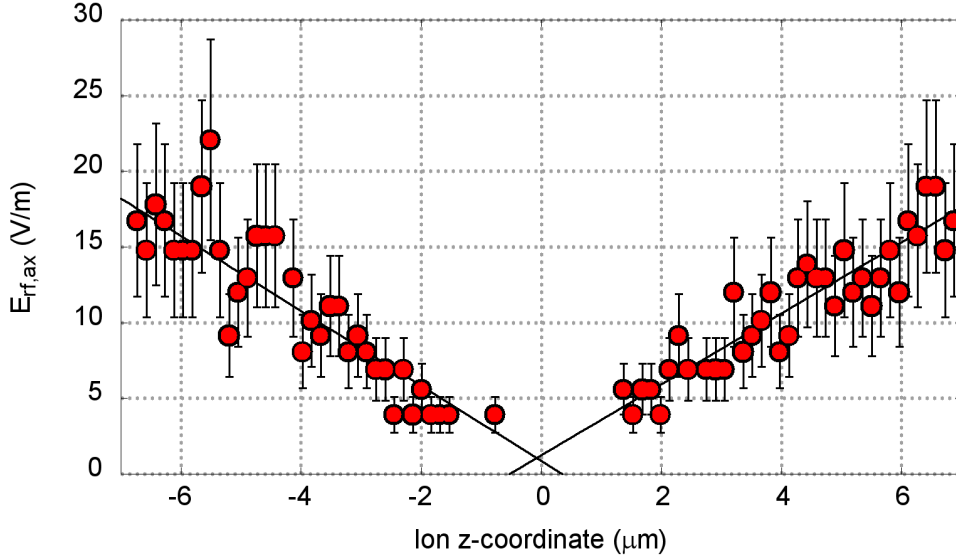


Figure 4.8.: Rf field along the axial direction. Shown is the axial component of the amplitude of the trap drive rf electric field as function of the ion position along the trap axis. From [Hannig et al., 2018b].

For illustrative purposes, Fig. 4.9 shows carrier Rabi oscillations on the  $|S_{1/2}, m_j = -1/2\rangle \leftrightarrow |D_{5/2}, m_j = -5/2\rangle$  transition after micromotion compensation. A fit results in a Rabi frequency of 19.9 kHz and a maximum contrast  $C = 0.962$ . The decay behavior is likely to be dominated by external magnetic field fluctuations, which are not suppressed in the current setup.

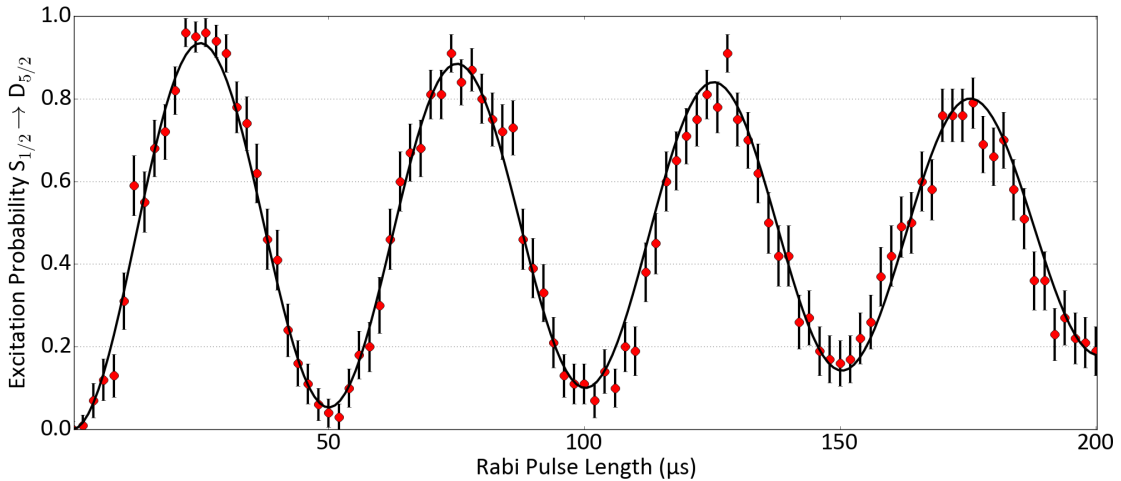


Figure 4.9.: Carrier Rabi excitation on the  $|S_{1/2}, m_j = -1/2\rangle \leftrightarrow |D_{5/2}, m_j = -5/2\rangle$  transition. Blue: measured excitation probability with statistical errors. Green: fit resulting in a Rabi frequency of 19.9 kHz, a quality factor  $Q = 53.8$  and a maximum contrast  $C = 0.962$ .

### 4.3. Error budget

From the heating rate and micromotion measurements presented in the previous sections a partial error budget for an  $^{27}\text{Al}^+ / ^{40}\text{Ca}^+$  clock operated inside the same setup can be estimated, as shown in Tab. 4.4. For this purpose, the mass dependent shifts are scaled with the mass ratio of  $^{27}\text{Al}^+$  and  $^{40}\text{Ca}^+$ .

$$\frac{\delta\nu_{\text{sec}}}{\nu} = -\frac{E_{\text{kin}}}{mc^2}. \quad (4.7)$$

During clock interrogation with a probe time  $T_p$ , electric field noise causes motional heating of the ion in the trap, which increases its kinetic energy. Therefore, the average kinetic energy of a motional mode  $j$  with corresponding secular frequency  $\omega_j$  can be calculated from the average motional quantum number in the ground state and the heating rate:

$$E_j = \hbar\omega_j \left( \bar{n}_j + \frac{1}{2} + \frac{T_p}{2} \dot{n}_j \right). \quad (4.8)$$

In case the static contribution to the radial trap potential is negligible ( $a_i \ll q_i$ ), cf. Eq. (2.10), intrinsic micromotion approximately doubles the ion's kinetic energy associated with secular motion [Wübbena et al., 2012, Berkeland et al., 1998]. Therefore, the secular motion second order Doppler shift is calculated from the measured average motional quantum numbers and heating rates [Scharnhorst, 2018]

$$\frac{\delta\nu_{\text{sec}}}{\nu} = -\frac{\hbar}{2m_{\text{Al}}c^2} \sum_j \omega_j \left( \bar{n}_j + \frac{1}{2} + \frac{T_p}{2} \dot{n}_j \right) (s_j^* + s_j) \quad (4.9)$$

with the sum over the modes  $j$ .  $s_j^* = 1$  for radial modes and  $s_j^* = 0$  for axial modes represents the intrinsic micromotion. The  $s_j$  are scaling factors of order of magnitude 1 derived by [Wübbena et al., 2012] for a mixed species two-ion crystal. Since the individual  $\bar{n}_j$  and  $\dot{n}_j$  were not measured for all six modes of the crystal yet,  $\bar{n}_j + \frac{1}{2} + \frac{T_p}{2} \dot{n}_j \approx 1 \pm 0.1$  is assumed for all six modes averaged over 200 ms interrogation time without cooling, based on the results for a single  $^{40}\text{Ca}^+$  ion shown in Tab. 4.1. For the same trap strength that resulted in  $\omega_{\text{rad,Ca}^+} \approx 2\pi \times 2.5$  MHz and  $\omega_{\text{ax,Ca}^+} \approx 2\pi \times 1.5$  MHz, the six motional mode frequencies and  $s_i$  listed in Tab. 4.3 are obtained. When inserted in Eq. (4.9), this yields  $\frac{\delta\nu_{\text{sec}}}{\nu} = (-4.2 \pm 0.3) \times 10^{-18}$ .

In the NIST  $\text{Al}^+ / \text{Mg}^+$  clock experiment, a double thermal distribution of motional

states was observed after groundstate cooling [Chen et al., 2017]. In order to assess the effect of such a distribution in the setup presented here, it is assumed that 10% of the motional states are thermally distributed around the individual Doppler temperatures of the modes listed in Tab. 4.3. For these 10%,  $\frac{\delta\nu_{\text{sec}}}{\nu} = (1.3 \pm 0.1) \times 10^{-17}$  is obtained, which results in a total shift of  $\frac{\delta\nu_{\text{sec}}}{\nu} = (-5.1 \pm 0.3) \times 10^{-18}$  for the double thermal distribution. Since the actual distribution is unknown, the value  $\frac{\delta\nu_{\text{sec}}}{\nu} = (-4.7 \pm 0.8) \times 10^{-18}$  is taken as conservative estimate for fractional second order Doppler shift caused by secular motion, given in Tab. 4.4.

Table 4.3.: Mode frequencies and scaling factors for the  $^{27}\text{Al}^+ / ^{40}\text{Ca}^+$  crystal.

Mode $j$	$\omega_i$	$s_j$
Axial in-phase	1.62	0.97
Axial out-of-phase	2.92	0.97
Radial I in-phase	1.88	1.19
Radial I out-of-phase	3.29	2.29
Radial II in-phase	1.88	1.19
Radial II out-of-phase	3.29	2.29

In Sec. 4.2 the reason for excess micromotion and its compensation via dc electric fields have been explained. However, after MM compensation a non-compensatable part of the EMM can remain, e.g. caused by a phase difference between the rf electrodes, cf. Sec. 4.2. This residual EMM results in a fractional second order Doppler shift  $\delta\nu_{\text{EMM}}/\nu$ . Following [Berkeland et al., 1998] it is given by

$$\frac{\delta\nu_{\text{EMM}}}{\nu} = -\frac{1}{2c^2} \sum_{i=x,y,z} \langle v_i^2 \rangle, \quad (4.10)$$

where  $c$  is the vacuum speed of light and  $v_i$  are the components of the velocity vector derived from the trap drive E-field measurements:

$$\langle v_i^2 \rangle = \left( \frac{QE_{\text{rf},i}}{\sqrt{2}\Omega_{\text{rf}}m_{\text{Al}}} \right)^2. \quad (4.11)$$

Inserting Eq. (4.5), (4.6), and (4.11) in Eq. (4.10) yields the overall fractional second order Doppler shift due to residual EMM. In Fig. 4.10 it is shown as function of the  $^{27}\text{Al}^+$  ion position along the trap axis (blue curve). Its uncertainty (solid red curve) is dominated by the determination of the micromotion sideband Rabi frequency. When the  $^{27}\text{Al}^+ / ^{40}\text{Ca}^+$  crystal is placed symmetrically around the trap center as

#### 4. Measurements

indicated by the vertical black lines, the fractional second order Doppler shift due to residual EMM  $\frac{\delta\nu_{\text{EMM}}}{\nu} = (-8.1 \pm 3.0) \times 10^{-19}$  is independent of the order of the ions in the crystal. The spacing of  $6 \mu\text{m}$  used here corresponds to a single  $^{40}\text{Ca}^+$  ion axial trap frequency of only  $\omega_{\text{ax,Ca}^+} \approx 2\pi \times 0.9 \text{ MHz}$  and therefore yields a conservative estimate of the shift, given the actual  $\omega_{\text{ax,Ca}^+} \approx 2\pi \times 1.5 \text{ MHz}$ .

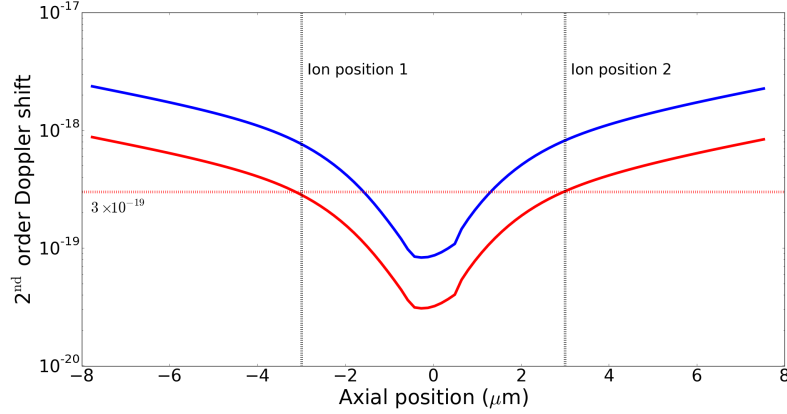


Figure 4.10.: Overall fractional second order Doppler shift due to residual EMM as function of the  $^{27}\text{Al}^+$  ion position along the trap axis. The solid blue line represents the shift and the solid red line its uncertainty, which is dominated by the determination of the micromotion sideband rabi frequency. Two vertical lines indicate the possible positions of an  $^{27}\text{Al}^+$  ion in a two ion crystal placed symmetrically around the trap center for a relatively weak axial confinement of  $\omega_{\text{ax,Ca}^+} \approx 2\pi \times 0.9 \text{ MHz}$ .

Another contribution to the error budget is the ac Stark shift due to blackbody radiation (BBR) given by [Rosenband et al., 2006]:

$$\frac{\delta\nu_{\text{BBR}}}{\nu} = -\frac{\pi (k_B T_{\text{env}})^4 \Delta\alpha(0)}{60\epsilon_0 \hbar^4 c^3} \quad (4.12)$$

$$= -3.8 \times 10^{-18} \left( \frac{T_{\text{env}}}{300 \text{ K}} \right)^4 \quad (4.13)$$

where  $\Delta\alpha(0) = (0.82 \pm 0.08) \times 10^{-41} \text{ Jm}^2 \text{V}^{-2}$  is the calculated static differential polarizability of the Al clock transition calculated by [Safronova et al., 2011],  $\epsilon_0$  the vacuum permittivity, and  $T_{\text{env}}$  the temperature of the ion's thermal environment. About 40% of the solid angle "seen" by the ion is covered by the vacuum chamber and the viewports, which are assumed to be at room temperature (300 K). The other 60% are covered by the trap, which is heated due to dielectric rf loss to a maximum



temperature of about 5 K above its environment<sup>1</sup>. As a conservative estimate, an averaged environmental temperature of  $T_{\text{env}} = (302.5 \pm 2.5)$  K was assumed. This results in  $\delta\nu_{\text{BBR}}/\nu = (-4.0 \pm 0.4) \times 10^{-18}$ , where the uncertainty is dominated by  $\Delta\alpha$ .

The last contribution treated here is the shift caused by phase distortions due to background gas particle collisions during clock interrogation. Only Langevin collisions lead to a shift large enough to be considered in current optical clocks. The frequency shift  $\Delta\nu_c$  can be calculated by multiplying the collision rate  $\Gamma_c$  with a scaling factor [Vutha et al., 2017] of 0.16. Since this estimate assumes a worst case phase shift of  $\frac{\pi}{2}$  for every collision event [Rosenband et al., 2008], it provides an upper limit to the uncertainty of the shift rather than the shift itself. The collision rate was measured by observing 21 reorderings of a  $^{27}\text{Al}^+ / ^{40}\text{Ca}^+$  crystal during a total observation time of 3892.5 s. Assuming that a reordering takes place for every second collision event, a collision rate of  $\Gamma_c \approx 0.0108 \text{ s}^{-1}$  and a fractional frequency uncertainty of  $1.5 \times 10^{-18}$  are obtained. The uncertainty of the collision shift could be further reduced by detecting collision events through reduced fluorescence of the hot  $\text{Ca}^+$  ion [Wübbena et al., 2012] and discarding the corresponding data points.

First order Doppler shifts due to drifts causing relative motion of the ion to the clock laser [Rosenband et al., 2008], originating from thermal effects or charging correlated with the probe-pulse, can be mitigated in the future by setting up an interferometer using the mirrors on the trap wafers shown in Fig. 3.2 to phase stabilize the clock laser to the position of the trap.

Tab. 4.4 summarizes the apparatus-related partial error budget for a single  $^{27}\text{Al}^+$  ion quantum logic clock derived in this section. The combined systematic fractional frequency uncertainty is  $1.7 \times 10^{-18}$ , which is equivalent to a height resolution of approximately 2 cm, under the assumption that all other shifts are negligible. The dominant contribution to the estimated uncertainty is the collisional shift. Therefore, background gas particle collision detection and data post-selection is an approach to reduce the total uncertainty in the current system. In the future, a similar trap design made of AlN [Keller, 2015] could be employed, since this ceramic material facilitates lower outgassing rates than the Rogers<sup>TM</sup> PCB boards. Additionally, a longer baking of the trap assembly could reduce the outgassing, especially of the epoxy glue employed to secure the dc wires on the carrier board, cf. Fig. 3.2.

---

<sup>1</sup>The trap chip temperature measurement was performed by the Czech metrology institute (CMI).

#### 4. Measurements

Table 4.4.: Estimated apparatus-related partial error budget in fractional units.

Shift	value ( $10^{-18}$ )	Uncertainty ( $10^{-18}$ )
Black body radiation:	-4.0	0.4
Excess micromotion		
second order Doppler:	-0.8	0.3
Secular motion		
second order Doppler:	-4.7	0.8
Background gas		
Langevin collisions:	0.0	1.5





## 5. Aluminum logic laser system

In the previous section, the transportable clock setup has been characterized using a single  $^{40}\text{Ca}^+$  ion. To operate the setup as an  $^{27}\text{Al}^+$  optical clock, two lasers driving the 267 nm logic and 267.4 nm clock transition introduced in Sec. 2.5 are required. Direct laser sources such as ECDLs or fiber lasers cover a broad wavelength range [Toptica Photonics AG, 2018], but to the knowledge of the author, there were no lasers directly emitting at the  $^{27}\text{Al}^+$  wavelengths commercially available when the laser system described here was set up.

"Custom" laser wavelengths can be generated by non-linear processes in specific crystalline materials, for instance Beta-Barium-Borate ( $\beta$ -BaB<sub>2</sub>O<sub>4</sub>, BBO), Lithium Triborate (LBO), Potassium Titanyl Phosphate (KTP) or Potassium Dihydrogen Phosphate (KDP) [Nikogosyan, 2005]. Important techniques are the sum- and difference frequency of two lasers and higher harmonic generation of a single wavelength [Wakui et al., 2014, Hu et al., 2013, Sherstov et al., 2010, Scheid et al., 2007, Wen et al., 2014, Eismann et al., 2012, Wilson et al., 2011, Vasilyev et al., 2011, Carollo et al., 2017]. In case of single-pass SHG pump light passes through a nonlinear crystal once, thereby generating light at twice the frequency. For instance, periodically-poled waveguide doublers, e.g. based on Lithium Tantalate or Lithium Niobate crystals for conversion into the blue and green spectral range are commercially available [NTT Electronics Corporation, 2017] and allow for compact SHG setups, like the first doubling stage of the  $^{27}\text{Al}^+$  laser system presented here, shown in Sec. 5.7. However, no such modules are available for the generation of the UV wavelengths required for quantum logic spectroscopy on  $^{27}\text{Al}^+$ , due to the lack of periodically poled non-linear crystals in this wavelength regime. The same applies for single-crystal monolithic ring cavities which enhance the pump laser light in an optical resonator to generate blue light down to wavelengths of 429 nm [Kozlovsky et al., 1994, Hemmerich et al., 1994, Skoczowsky et al., 2010]. Due to the lack of the aforementioned solutions in the UV, SHG by a nonlinear BBO crystal placed in an optical enhancement resonator [Zimmermann et al., 1990] that increases the

## 5. Aluminum logic laser system

pump light power was chosen.

In summary, for each of the two  $^{27}\text{Al}^+$  wavelengths an individual setup for frequency quadrupling of a commercial IR laser in two subsequent SHG stages has been built, including a self-developed enhancement cavity for the second SHG step to the UV, which is based on the bow-tie cavity concept for critically phase-matched SHG.

### 5.1. Higher harmonic generation theory

Here the fundamental concept of higher harmonic generation is briefly recapped following the textbook [Nikogosyan, 2005], where more details are provided.

When an uncharged particle or bulk material is exposed to an electric field  $\vec{E}$ , elementary charges inside can be displaced from their equilibrium position leading to a macroscopic dielectric polarization density  $\vec{P}$  which is linked to the field by the relation

$$\vec{P}(\vec{E}) = \kappa_0 \vec{E} + \underbrace{\chi^{(2)} \vec{E}^2}_{=: \vec{P}^{(2)}(\vec{E})} + \chi^{(3)} \vec{E}^3 + o(\vec{E}^4), \quad (5.1)$$

where  $\kappa_0$  is the linear dielectric susceptibility, the corresponding contribution of the polarization is proportional and collinear to the electric field, causing a second antiparallel field. This effect is practically employed in capacitors, where high- $\kappa_0$  materials attenuate the internal field for a given voltage and therefore allow for high volumetric energy densities. The  $\chi^{(i)}$  are the higher order nonlinear dielectric susceptibilities, which are tensors of the  $i^{\text{th}}$  ranks, and required for higher harmonic generation. Following the convention  $\chi_{ij(k)} = 2d_{ij(k)}$  common in literature, the second term of Eq. (5.1) in matrix form can be written as:

$$\vec{P}^{(2)}(\vec{E}) = \chi^{(2)} \vec{E}^2 = \begin{bmatrix} d_{11} & d_{12} & d_{13} & d_{14} & d_{15} & d_{16} \\ d_{21} & d_{22} & d_{23} & d_{24} & d_{25} & d_{26} \\ d_{31} & d_{32} & d_{33} & d_{34} & d_{35} & d_{36} \end{bmatrix} \cdot \begin{bmatrix} E_X^2 \\ \dots \\ 2E_X E_Y \end{bmatrix}, \quad (5.2)$$

where X, Y, and Z are the components in the directions of the crystal coordinate system shown in Fig. 5.1(b). The latter is defined by the optical properties of the crystal. For an uniaxial crystal such as BBO the following nomenclature inside the crystal applies. The wave vector  $\vec{k}$  of the light wave and the z-axis span the *principal*

*plane*. Light beams are named according to the orientation of their polarization to the principal plane. Normally polarized beams are called *ordinary* or o-beams, beams polarized in the principal plane *extraordinary* or e-beams. For o-beams the refractive index depends on their propagation direction, for e-beams it does not.

Considering PL that is purely polarized in X-direction one obtains

$$\vec{P}^{(2)}(\vec{E}(t)) = \begin{pmatrix} d_{11} \cdot (E_X \sin(\omega t))^2 \\ d_{21} \cdot (E_X \sin(\omega t))^2 \\ d_{31} \cdot (E_X \sin(\omega t))^2 \end{pmatrix} = \begin{pmatrix} d_{11} \\ d_{21} \\ d_{31} \end{pmatrix} \cdot E_X^2 \cdot \left( \frac{1}{2} + \underbrace{\sin(2\omega t)}_{\text{SHG}} \right) \quad (5.3)$$

In conclusion, materials with non-zero second order nonlinear dielectric susceptibilities that are exposed to an oscillating E-field can exhibit polarization oscillations with twice the frequency of the field. Moreover, the polarization is proportional to the square of the pump field amplitude. Since moving electric charges create proportional electric fields, SHG occurs.

In the low conversion efficiency regime the PL remains undepleted and the SHG power  $P_{\text{SHG}}$  scales with the square of the pump light power  $P_{\text{PL}}$ :

$$P_{\text{SHG}} = \kappa P_{\text{PL}}^2, \quad (5.4)$$

where  $\kappa$  is the conversion coefficient.

Referring to Eq. (5.2), it has to be noted that non-zero  $d_{ij}$  only occur in non-centrosymmetrical crystals [Neumann and Meyer, 1885]. Additionally, the Kleinman symmetry condition [Kleinman, 1962] applies in most of the relevant cases, reducing the number of independent entries. Further simplification arises from the crystal's symmetry properties. In the case of BBO used in the SHG cavities presented in this thesis, the following effective second-order nonlinear coefficient for ooe processes is obtained:

$$d_{\text{eff}} = d_{31} \sin(\theta) - d_{22} \cos(\theta) \sin(3\varphi), \quad (5.5)$$

where  $\theta$  is the angle between the optic axis (z) of the crystal and  $\varphi$  the angle between the x-axis of the crystal and the projection of the pump light (PL) k-vector on the xy-plane. For efficient SHG,  $d_{\text{eff}}$  has to be maximized. However, the result would only be valid for an infinitesimal small crystal volume. In macroscopic crystals, SHG light has to interfere constructively with the SHG generated earlier for power

## 5. Aluminum logic laser system

buildup. This leads to the phasematching condition for the wavevectors of the pump light  $\vec{k}_{\text{PL}}$  and the SHG  $\vec{k}_{\text{SHG}}$

$$\vec{k}_{\text{SHG}} \stackrel{!}{=} 2\vec{k}_{\text{PL}}, \quad (5.6)$$

which can be fulfilled by taking advantage of the crystal's birefringence, i.e. polarization dependent refractive indices  $n_o$  and  $n_e$ . By choosing the appropriate phase-matching angle  $\theta_{\text{pm}}$ ,  $n_{\text{SHG}} = n_{\text{PL}}$  can be achieved [Nikogosyan, 2005]. Since the refractive indices depend on the wavelength as described by the Sellmeier equations [Sellmeier, 1871], the  $\theta_{\text{pm}}$  is wavelength dependent, as shown in Fig. 5.1(a) for BBO. For SHG of 534 nm as it is required to obtain the  $^{27}\text{Al}^+$  wavelengths in BBO the resulting phase-matching angle is  $\theta_{\text{pm}} = 47.4^\circ$ .

All vector- and angle definitions relevant for ooe critically phase matched SHG in BBO are summarized in Fig. 5.1(b). The choice of the angle between the crystal facets and the principal plane is arbitrary. In the later discussed cavity, Brewster's angle will be chosen in order to avoid PL loss at the facets.



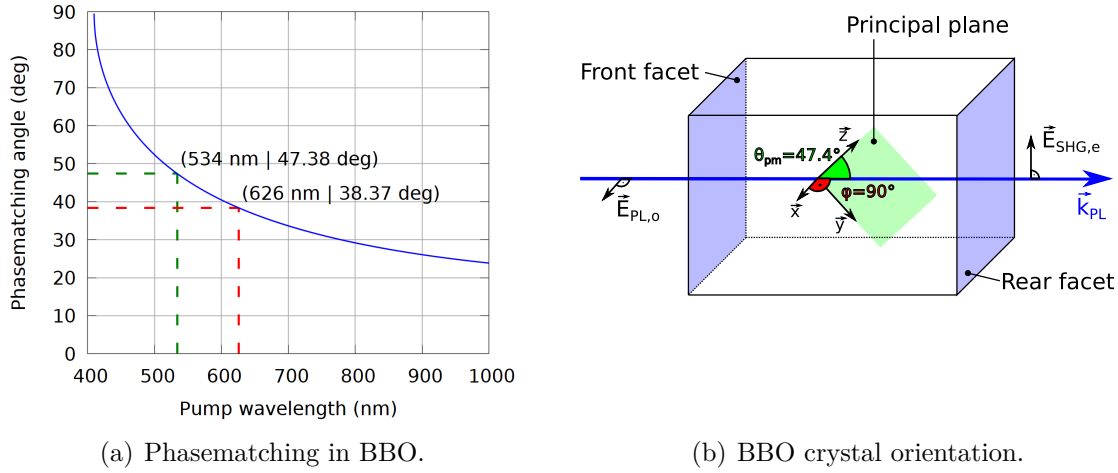


Figure 5.1.: SHG in BBO. Phasematching angle as function of the PL wavelength (blue) for BBO (a). Dashed lines indicate the two cases relevant in this thesis: 534 nm PL to generate the  $^{27}\text{Al}^+$  logic laser (green) and 626 nm for  $\text{Be}^+$  cooling, employed in the first generation cavity under test, cf. Sec. 5.5). The minimum PL wavelength is 409.6 nm, resulting in 204.8 nm SHG [Kato, 1986]. The optical properties of the crystal provide an internal coordinate system (b) with the orthonormal vectors  $\vec{X}$ ,  $\vec{Y}$ , and  $\vec{Z}$ , where  $\vec{Z}$  is the crystal axis, spanning the principal plane with the PL wave vector  $\vec{k}$ . For efficient SHG, the  $\vec{k}$  and  $\vec{Z}$  form the phasematching angle  $\theta_{\text{pm}}$ .  $\varphi$  is chosen such that the effective second-order nonlinear coefficient  $d_{\text{eff}}$  is maximized.

## 5.2. A setup for second harmonic generation to the UV

*A substantial fraction of the content presented in Sec. 5.2 up to including Sec. 5.5 has been part of a publication by the author of this thesis [Hannig et al., 2018a]. For simplicity, individual citations in the main text are omitted.*

*The geometry of the SHG setup presented here is suitable for a broad range of wavelengths in the UV. The first cavity built is part of a  $^9\text{Be}^+$  laser system generating UV light at 313 nm. Therefore, the following subsections refer to that wavelength and SHG to 267 nm is treated starting from Sec. 5.5.1.*

### SHG power optimization

The single-pass conversion efficiency of cw light in a BBO crystal of a few mm length in general is rather low (on the order of  $\kappa \sim 10^{-4}$  1/W). Therefore, an enhancement cavity for the PL is built around the nonlinear crystal [Franken et al., 1961, Armstrong et al., 1962, Ashkin et al., 1966]. The optimization of the cavity SHG output power can be divided into two steps: first the optimization of the power generated per single pass of the PL through the crystal [Boyd and Kleinman, 1968] and second the optimization of the power enhancement [Jurdik et al., 2002].

### Single pass optimization

As mentioned above, the SHG power generated per infinitesimal crystal volume is proportional to the square of the PL intensity. Tighter focusing of the PL enhances the intensity at the focus, at the expense of lower intensity away from the focus. This tradeoff for a given crystal length  $l$  has been investigated for the propagation of a circular Gaussian beam with minimum waist  $w_0$  by Boyd and Kleinman [Boyd and Kleinman, 1968], who derived an optimum focusing ratio of  $l/b = 2.84$  in the absence of birefringence, where  $l$  is the crystal length and  $b = w_0^2 k$  the confocal parameter with  $k = 2\pi/\lambda$ . However, in the presence of birefringence, the phase vector  $\vec{k}$  and Poynting vector  $\vec{S}$  of the extraordinary SHG wave are in general not parallel, which results in a walk-off angle  $\varrho$  between SHG and PL beam of

$$\varrho = 4.6^\circ \tag{5.7}$$

## 5.2. A setup for second harmonic generation to the UV

for SHG of 626 nm in BBO. This effect is quantified by the walk-off parameter  $B$  [Boyd and Kleinman, 1968]:

$$B = \varrho\sqrt{lk}/2 \quad (5.8)$$

For a 10 mm long BBO crystal the walk-off angle leads to a displacement of 0.8 mm between the SHG light generated right behind the front facet and that generated close to the rear facet. Given the comparatively small pump waist size of about 30  $\mu\text{m}$ , which initially defines the vertical spread of the SHG beam, the walk-off results in a strong ellipticity of the SHG beam. This effect can be partially compensated by a reduced pump light focusing to increase the overlap of the PL and SHG spatial mode.

Furthermore, a focused Gaussian beam exhibits a phase deviation  $\Delta k$  from an ideal plane wave that changes along the propagation direction, known as Gouy effect [Gouy, 1890]. It is typically quantified by the parameter  $\sigma = \frac{1}{2}b\Delta k$ . For the SHG considered here, this means that the degree to which the phasematching condition is fulfilled changes over the crystal length. Taking all these effects into account through integration over infinitesimal contributions of the PL to the SHG light when propagating through the crystal, the Boyd-Kleinman theory provides optimum parameters  $l/b$  and  $\sigma$  for single-pass SHG output power. For SHG from 626 nm to 313 nm in a 10 mm long BBO crystal, one obtains  $l/b = 1.42$ ,  $\sigma = 0.75$ , and  $\omega_0 = 19 \mu\text{m}$  with a single-pass conversion efficiency of  $\kappa = 1.1 \cdot 10^{-4}$ . A similar analysis can be performed in case of an elliptical focus inside the crystal [Freearde et al., 1997], as is the case for astigmatic cavities and/or Brewster-cut crystals.

### Cavity geometry

A nonlinear medium with low conversion efficiency placed in an optical cavity in which the PL power is enhanced by a factor on the order of 50, can provide up to 2500 times more SHG output power than is possible in single pass configuration.

The probably most simple possible cavity design are two coaxial mirrors separated by a distance  $d$  as shown in Fig. 5.2(a) (a). Their radii  $r_I$  and  $r_{II}$  have to fulfill the stability criterion for optical resonators:

$$0 \leq \left(1 - \frac{d}{r_I}\right) \left(1 - \frac{d}{r_{II}}\right) \leq 1. \quad (5.9)$$

## 5. Aluminum logic laser system

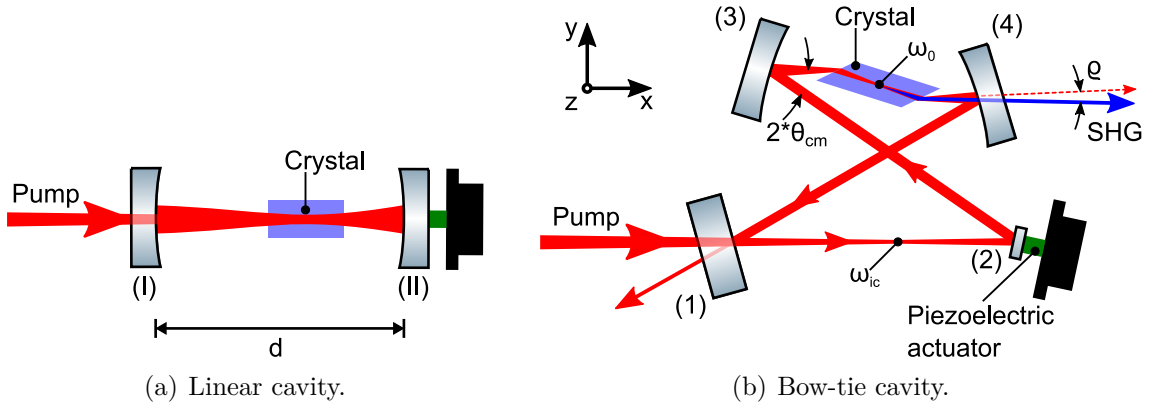


Figure 5.2.: Schematic SHG cavity layouts. a): A linear cavity is composed of two mirrors and a nonlinear crystal placed in the beam waist  $\omega_0$ . For length stabilization, one mirror is attached to a piezoelectric actuator. b): the bow-tie cavity is pumped through mirror (1) with light focused on the incoupling waist  $\omega_{ic}$ . A lightweight mirror (2) on a piezoelectric actuator is used to lock the length of the cavity. (3) and (4) focus the light to the waist  $\omega_0$  inside the nonlinear crystal and modematch the beam for the next roundtrip. Adapted from [Hannig et al., 2018a]. Some components in the figure are adapted from [Franzen, 2009].

However, in this case standing wave formation of the PL occurs when the cavity is locked. Per definition, the antinodes of this wave stay at fixed positions inside the cavity. Therefore, some parts of the bulk material are always exposed to the strong electric field of the antinodes, while the crystal material at the nodes is not exposed to any field. Therefore, the material at the antinodes is prone to photorefractive damage. Compared to the antinodes of a standing wave, the average electric field of a moving wave of the same intensity is smaller by a factor of two. For this reason, ring cavities made of at least three mirrors have been developed. But three mirrors have the drawback of large angles of incidence that can potentially cause severe astigmatism when curved mirrors are involved. A common design for an optical enhancement cavity, referred to as "bow-tie", consists of four mirrors and is schematically shown in Fig. 5.2(b). Here, the angle of incidence on the curved mirrors can be chosen freely, which allows for astigmatism compensation of Brewster-cut crystals by choosing a suitable distance between the two mirror pairs involved (see below). Moreover, the folded beam path enables relatively compact setups for a given round trip length.

The reflectivity of the incoupling mirror (1) fulfills the impedance matching con-

dition (see below). Mirror (2) is mounted on a piezoelectric actuator with a maximum stroke sufficient to change the cavity length by more than one free spectral range (FSR) to enable length stabilization of the cavity to the PL wavelength. It is lightweight to achieve high mechanical resonance frequencies and thus a high feedback bandwidth. Mirrors (3) and (4) are concave, and their distance is chosen to provide a focus of the appropriate size at the center of the crystal. The fourth mirror also acts as outcoupler for the SHG light. A fully monolithic bow-tie cavity design similar to the Nd:YAG NPRO design [Kane and Byer, 1985] would suffer from detrimental PL loss due to the high linear absorption of  $\alpha_{PL} \sim 0.01 \text{ cm}^{-1}$  for  $\lambda = 626 \text{ nm}$  in BBO [Watanabe et al., 1991].

### Crystal shape

For maximum PL power enhancement and therefore a high SHG output power (cf. Eq. (5.4)), low PL loss inside the cavity from absorption or scattering is required. One major source of loss in circulating PL is reflection at the interfaces of the nonlinear medium and the surrounding gas. For example, by inserting the refractive indices for BBO and air in the Fresnel equations, which can be found in textbooks like [Hecht, 2001], it can be shown that in the case of an uncoated BBO crystal in air 6.3% of the in plane polarized PL would be reflected on each of the crystal facet for  $0^\circ$  angle of incidence. These losses would restrict the PL power build up factor inside the cavity to around 7. The reflections at the interfaces can either be avoided by the application of an anti-reflective coating on the surfaces or by cutting and mounting the crystal under Brewster's angle to the incident beam. While anti-reflective (AR) coatings protect hygroscopic crystals like BBO against moisture in the environment, they are prone to damage induced by UV or pump light. Considering a cavity pumped with 500 mW at 626 nm enhanced by a factor of 100 focused to a  $30 \mu\text{m}$  waist in the middle of an 10 mm long crystal, the resulting average PL intensity in the spots on the facets is  $\approx 5 \text{ kW/mm}^2$ , which is challenging in terms of thermal damage of the coating. Furthermore, residual reflections on surfaces orthogonal to the PL beam can cause a backward traveling PL wave. Since the wave is traveling counterpropagating to the pump beam, also the generated SHG is traveling in the opposite direction, leaves the cavity through mirror (3) in Fig. 5.2(b), and therefore is practically lost. Moreover, backwards traveling PL can leave the cavity through the incoupling mirror (1) coaxially to the incoming PL and therefore potentially cause non-desired feedback on the seed laser. Weighting these properties and given

## 5. Aluminum logic laser system

the option to operate the crystal in a dry environment, it seems advantageous to choose a crystal cut under Brewster's angle  $\theta_B$  for the PL. For SHG of 626 nm in BBO the resulting angle is

$$\theta_B = \arctan(n_{\text{PL}}) = 59.0^\circ, \quad (5.10)$$

where  $n_{\text{PL}}$  is the index of refraction for the PL. Since PL and SHG have orthogonal polarization in ooe SHG, the Brewster condition can only be fulfilled for the pump light. The corresponding fractional internal reflection of the SHG at the crystal-gas-interface is given by Fresnel's equations for s-polarized light that simplify to

$$R_{\text{SHG}} = (\sin(\pi/2 - 2\theta_B))^2 \approx 22\%. \quad (5.11)$$

### Impedance matching

Assuming ideal mirrors and input beam mode matching, the entire pump light can be coupled into the cavity, if the incoupling mirror transmission is chosen in such a way that coupled pump light compensates all losses inside the cavity during a round trip. In the case of a SHG cavity, the latter is composed of two parts: PL loss due to conversion and parasitic loss due to imperfect reflection inside the resonator and linear absorption in the nonlinear crystal and surrounding gas with absorption coefficient  $\alpha_{\text{PL}}$ .

The total round trip transmission of the cavity as a function of the single cavity mirror reflectivity  $R_M$  and the crystal facet transmission  $T_C$  without considering conversion into SHG is

$$t = R_M^3 T_C^2 (1 - 2l\alpha_{\text{PL}}). \quad (5.12)$$

Taking into account the loss through conversion with a factor  $\kappa P_{\text{PL}}^2$ , the optimal incoupling mirror reflectivity  $R_{\text{in}}$  for impedance matching is [Polzik and Kimble, 1991]

$$R_{\text{in}} = 1 - \left( \frac{1-t}{2} + \sqrt{\frac{(1-t)^2}{4} + t\kappa P_{\text{PL}}} \right), \quad (5.13)$$

where the small correction factor  $t$  from the incoupling mirror has been applied.

### Cavity parameters

Both, the non-normal incidence of the cavity mode on the curved mirrors and crystal facets cut under Brewster's angle, introduce astigmatism in the cavity which needs to be accounted for in the design. The system forms two effective cavities in the  $xy$  (sagittal) and  $xz$  (tangential) planes which both need to be stable. Optimizing for simultaneous stability and conversion efficiency [Wilson et al., 2011, Freearde et al., 1997] for a 10 mm BBO crystal and a 50 mm radius of curvature of the mirrors yields a mechanical cavity footprint which is inconveniently large to realize experimentally in a compact way. Instead, the cavity parameters outlined in Tab. 5.1 were chosen.  $w_{0,xy}$  and  $w_{0,xz}$  are the sagittal and tangential waist, respectively, which are larger than the optimum waist  $\omega_0$  from Boyd-Kleinmann. This has the added advantage of reducing crystal damage from high intensities at the crystal surfaces. In the end the actual cavity geometry is defined by  $l$ ,  $\theta_B$ , the mirror to crystal distance  $d_{mc}$ ,  $\theta_{cm}$ , and the geometric round-trip length  $l_{geo}$ .

Table 5.1.: Geometric parameters of the doubling cavity using a 10 mm BBO-crystal pumped with  $P_{PL} = 0.5 \text{ W}$  at  $\lambda_{PL} = 626 \text{ nm}$  and  $r = 50 \text{ mm}$  mirrors

Phasematching angle	$\theta_{pm} = 38.4^\circ$
Waist sagittal	$\omega_{0,xy} = 25.3 \mu\text{m}$
Waist tangential	$\omega_{0,xz} = 39.6 \mu\text{m}$
Brewster angle	$\theta_B = 59.0^\circ$
Angle on curved mirrors	$\theta_{cm} = 15.7^\circ$
Distance mirror to crystal	$d_{mc} = 25.1 \text{ mm}$
Geometric round trip length	$l_{geo} = 304.8 \text{ mm}$
Input coupling waist	$\omega_{ic} = 166 \mu\text{m}$

For this choice of parameters, both the sagittal and tangential cavity are stable simultaneously and the input coupling waist (between the two flat mirrors) is nearly circular with a waist of  $166 \mu\text{m}$ . Compared to the geometry for optimal efficiency [Wilson et al., 2011, Freearde et al., 1997], the expected loss in conversion efficiency is only about 12%. This moderate loss is outweighed by the gain in mechanical stability and ruggedness due to the smaller footprint. The waists and Brewster's angle have been calculated for SHG of  $\lambda = 626 \text{ nm}$ , but their dependence on the PL wavelength is rather weak. For  $\lambda = 534 \text{ nm}$  PL for instance, the waists change by  $-1.9 \mu\text{m}$  and  $-2.9 \mu\text{m}$ . Brewster's angle increases by  $0.1^\circ$ . Therefore, the cavity geometry is practically suitable for frequency doubling of a spectral range of several

## 5. Aluminum logic laser system

hundred nm accessible with BBO in SHG ooe-processes, where the pump beam is polarized normal (ordinary, o) to the principal plane of the crystal and the SHG beam in the plane (extraordinary, e), starting at 204.8 nm [Kato, 1986], as long as a 10 mm long BBO-crystal cut under the corresponding phasematching angle is used. In conclusion, the shape of the monolithic housing (see below) is universal for SHG to the UV.

### 5.2.1. Length stabilization and its limit

During operation, the length of the cavity is stabilized to the PL wavelength via a voltage applied to the piezoelectric actuator using a PI controller. The required error signal is generated using the Hänsch-Couillaud (HC) locking scheme [Hänsch and Couillaud, 1980] that generates a dispersion-shaped error signal from the phase shift upon reflection of light from the cavity. P-polarized light is coupled into the cavity and experiences a varying phase shift near the cavity resonance, while s-polarized light does not couple into the cavity and thus obtains a constant  $\pi$  phase shift upon reflection. Compared to the Pound-Drever-Hall [Drever et al., 1983] locking scheme, no sidebands are imprinted on the PL and thus are also absent in the SHG, which is an advantage for certain applications.

The locking bandwidth is fundamentally limited by the mechanical resonance frequency  $f^*$  of the piezoelectric actuator and the attached mirror. It is given as [Thorlabs Inc., 2017]

$$f^* = f_0 \sqrt{\frac{\frac{m}{3}}{\frac{m}{3} + M}}, \quad (5.14)$$

where  $f_0$  is the mechanical resonance frequency of the piezoelectric actuator,  $m$  its mass and  $M$  the mass of the attached mirror.

For the monolithic cavity design presented here, only relatively small changes of the round-trip length are expected. Therefore a short piezoelectric actuator with low weight and high resonance frequency seems to be sufficient to keep the cavity length stabilized under moderate environmental perturbations.



### 5.3. Cavity design

Since the  $^{27}\text{Al}^+$  clock is intended to be transportable, "turn-key" operation after being exposed to mechanical environmental conditions typical for long distance truck and plane transportation is the an important design goal, namely to avoid the necessity of time-costly optics realignments. Along these lines, also robust operation inside the climatized container housing the  $^{27}\text{Al}^+$  clock in the future is required to guarantee that the effective measurement time is not limited by the availability of the  $^{27}\text{Al}^+$  laser systems. Also, the overall footprint should be reduced as far as possible given the previous requirements. Moreover, commercial systems should be surpassed in terms of flexibility, i.e. providing access to the pump light reflected from the crystal front facet and to the internal reflection of the SHG light in the crystal.

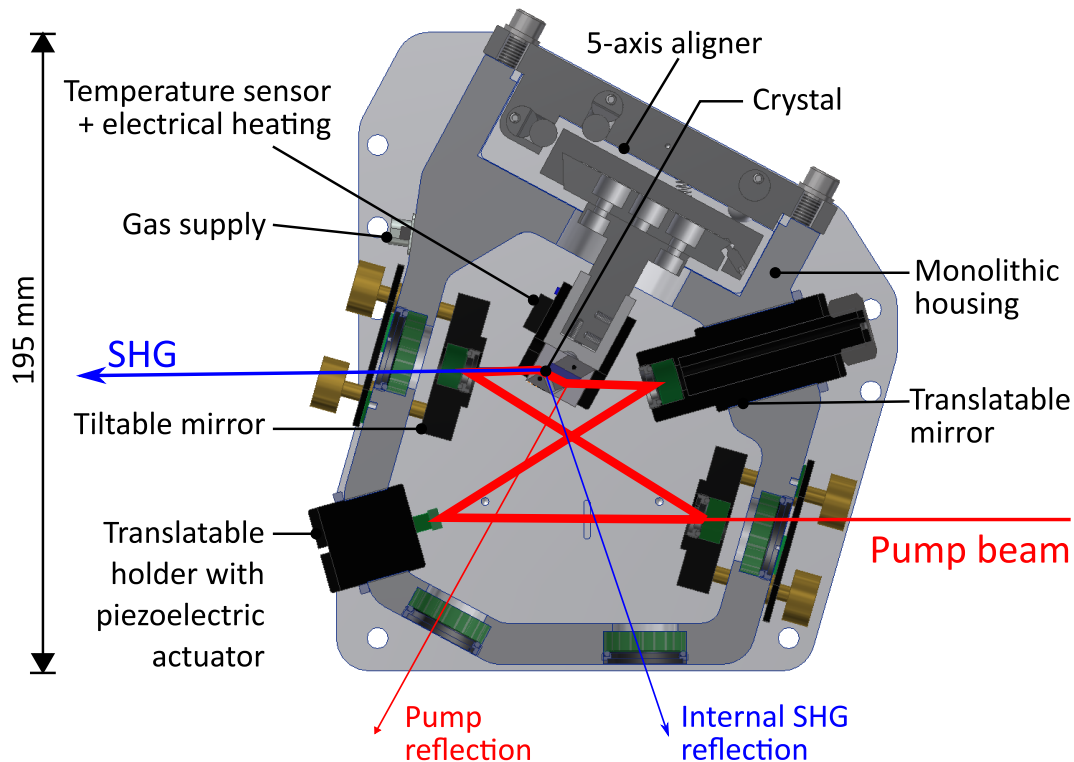


Figure 5.3.: Schematic cross section of the first generation SHG cavity. All mechanical components are mounted directly to the monolithic housing. The incoupling and outcoupling mirror are tiltable using micrometer screws while the other mirrors can be translated only. The temperature-stabilized BBO crystal is mounted on a 5-axis aligner. Ar-coated windows allow for optical access to the sealed cavity. From [Hannig et al., 2018a].

## 5. Aluminum logic laser system

Given the aforementioned requirements, the main body is milled from a single Al block as shown in Fig. 5.3. Two mirror holder front plates mounted via three micrometer screws (150  $\mu\text{m}$  displacement per turn) and two springs each, all mounted directly on the main body, feature the four degrees of freedom (DOF) required to close the beam path. In combination with the two other mirrors that are mounted on fine-threaded aluminum cylinders, the cavity round trip length can be adjusted on the few mm-scale while keeping the angles between the beams and therefore the astigmatism compensation constant. The mirrors are mounted using stress-free retaining rings to avoid birefringence caused by mechanical stress. This does not apply for the mirror behind the incoupler which is glued<sup>1</sup> on a piezoelectric actuator<sup>2</sup> to enable cavity length stabilization. In crystals used for SHG into the UV, crystal inhomogeneities and degradation effects have been observed. Compensation of these effects requires two translational DOF parallel to the front surface of the crystal. With a third DOF the waist position in the crystal along the direction of the PL propagation is adjusted. Two additional rotational DOF allow the fine adjustment of the phasematching and Brewster's angle. All these DOF are provided by a commercially available 5-axis-aligner<sup>3</sup> that is mounted directly in the main body. The crystal is mounted in two shells that are mounted to a lever connected to the aligner. These shells and the lever are equipped with channels that lead dry high purity oxygen from a supply connected to the main body directly to the two facets of the crystal to prevent moisture-induced fogging and light-induced damage [Sandberg, 1993] of the crystal. Additionally, the tip of the lever can be actively temperature stabilized using a thick-film resistor<sup>4</sup> and a sensor<sup>5</sup> connected via a standard D-sub feedthrough to a suitable PI controller to prevent condensate formation on the crystal facets that would likely cause degradation of hygroscopic crystals like BBO. To prevent gas exchange with the environment, the cavity is fitted with four windows that provide optical access for the PL and SHG and their reflections on the crystal's facets. Finally, the cavity is sealed with FKM gaskets to prevent unwanted substances from entering the enhancement cavity and cause degradation of the crystal and/or mirrors. Therefore, a gas outlet in the main body ensures a moderate gas exchange rate and overpressure inside the housing. The oxygen concentration can

---

<sup>1</sup>Thorlabs 353NDPK Epoxy

<sup>2</sup>Thorlabs AE0505D08F

<sup>3</sup>NEWPORT 9081-M

<sup>4</sup>Vishay Sfernice RTO 20

<sup>5</sup>TDK B57861S

be measured by a sensor<sup>6</sup> located in the lid of the main body.

## 5.4. Setup

Fig. 5.4 shows a schematic overview of the complete setup for SHG at 313 nm. It is composed of a sum frequency generation (SFG) setup for the 626 nm pumplight, the SHG cavity setup, the locking electronics, and a computer for power recording. The general approach is similar to [Wilson et al., 2011].

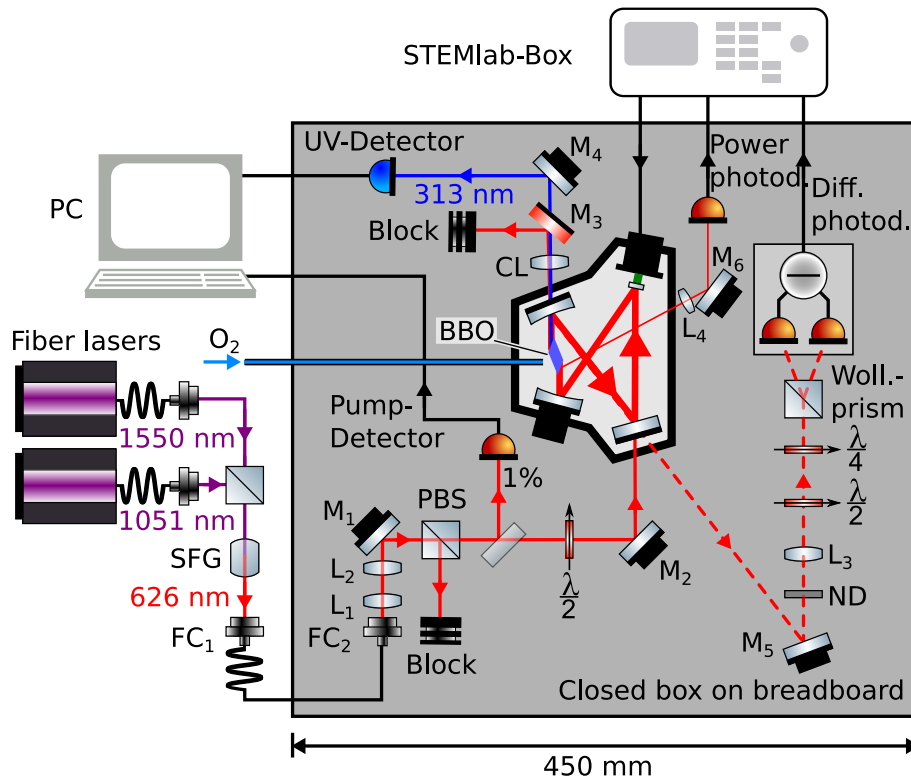


Figure 5.4.: Schematic overview of the complete setup for 313 nm generation.  $FC_i$  : fiber coupler,  $L_i$  : lens,  $M_i$  : mirror, PBS : polarizing beam splitter cube,  $\frac{\lambda}{2}/\frac{\lambda}{4}$  half/quarter wave plate, ND: neutral density filter. Left: pump light generation at 626 nm by SFG of two IR fiber lasers. Center: 313 nm generation in the resonant enhancement bow-tie cavity locked by the Hänsch-Coulliaud locking scheme (dashed beam path and digital multi purpose PI controller STEMLab-Box). For output power stability monitoring, a fraction of the pump and SHG light is picked off and measured via photo diodes. From [Hannig et al., 2018a], modified. Some components in the figure are adapted from [Franzen, 2009].

<sup>6</sup>Greisinger GOX 10

### Pumplight setup

Up to 1.1 W pump light (PL) at 626 nm are generated by sum frequency generation (SFG) of two fiber lasers at 1550 nm and 1051 nm in a periodically poled lithium niobate (PPLN) crystal described in [Idel, 2016] and coupled into a polarization maintaining fiber at FC1. This fiber leads to a 12.7 mm thick (450 mm)<sup>2</sup> aluminum breadboard with all the optical components for the 313 nm SHG. While this breadboard size has been chosen for convenience, it seems possible to reduce the overall footprint of the setup by a factor of three by optimizing the beam path layout. The breadboard as well as the aforementioned SFG are covered by two boxes made of aluminum. Both are mounted on a standard air damped optical table in a laboratory temperature stabilized at the 1 K level. The breadboard holding the cavity is placed on 5 mm thick viscoelastic damping rubber<sup>7</sup>.

### SHG setup

Behind the PL fiber coupler FC2 a telescope composed of two lenses L1 and L2 with focal lengths  $f = +50$  mm and  $f = +30$  mm, respectively, mounted on single axis translation stages is used for the modematching, i.e. overlapping of the spatial modes of the pump light beam and the circulating beam inside the cavity. A 1% pickup beam is used to monitor the PL power. The two highly stable mirrors M1 and M2 provide the four DOF required for the coupling the PL into the cavity. Both mirrors are mounted using retaining rings to avoid birefringence due to mechanical stress. A polarizing beamsplitter cube (PBS) cleans the polarization of the PL and a subsequent  $\lambda/2$  waveplate rotates it into the plane required for the SHG. Behind the outcoupling mirror of the SHG cavity a cylindrical lens CL with focal length  $f = +100$  mm is employed for correcting the astigmatism arising from the walk-off of the SHG light generated inside the BBO crystal (s. 5.2). A second mirror (M3) of the same type as the outcoupler is used to filter the transmitted PL from the SHG beam to simplify diagnostics on the optical setup downstream the SHG cavity. For the test presented here, a thermal powermeter measurement head is used to collect the SHG light. When the cavity is not locked, the major fraction of the incident PL is reflected at the incoupling mirror. Therefore, a neutral density filter (ND) is installed inside that beam path to reduce the optical power by a factor of 1000. The remaining reflected pump light is focussed by lens L3 with focal length  $f = +250$  mm

---

<sup>7</sup>Sorbothane<sup>®</sup>

and sent through a polarization analyzer composed of a half-wave plate, a quarter-wave plate, and a Wollaston prism to generate two orthogonally polarized beams of similar intensity carrying the information about the phase relation of the PL entering the cavity [Hänsch and Couillaud, 1980]. These two beams hit a differential photodiode. The resulting signal is the error signal. In its nearly linear section, it is about proportional to the deviation of the cavity length from an integer multiple of the PL wavelength.

Due to scatter and non-perfect PL polarization in the xy-plane of the cavity, a fraction of the PL is reflected on the front surface of the crystal. This effect on the one hand reduces the maximum obtainable SHG power. On the other hand, assuming a constant PL polarization due to a polarizer installed in front of the cavity, it can be directed on a photodiode to generate a signal proportional to the PL power circulating inside the cavity, which is exploited by the locking electronics described in the next paragraph.

### Digital PI controller

To achieve resonant enhancement of the PL inside the cavity, its optical path length has to be kept interferometrically stable to an integer multiple of the PL wavelength. The length adjustment is implemented via a piezoelectric actuator that displaces one of the cavity mirrors (mirror (2) in Fig. 5.2(b)). Given the error signal explained in the previous paragraph, a feedback loop acting on the piezo is required, that comprises a fast contribution proportional (P) to the error signal and a comparatively slow contribution generated by integrating (I) the error signal in time. Traditionally such proportional-integral (PI) controllers were implemented using analog electronics. The integration of these in state of the art digital experiment control systems is rather involved. Therefore, here a digital PI controller based on a modified STEMLab 125-14 (formerly: Red Pitaya) system was chosen. While the development and implementation of the controller are described in detail by [Fenske, 2015] and [Hannig et al., 2018a], here only the key features and properties will be given. The system comprises a field programmable gate array (FPGA) with attached microcontroller and provides two fast analog input and output channels, operating at sampling rate of 125 MS/s with 14-bit nominal resolution. The output channels of the STEMLab are connected to amplifiers to obtain 16 V<sub>pp</sub> outputs. One of these is connected to the piezoelectric actuator inside the cavity. Since high frequency electronic noise can excite oscillations of the control loop, a 10  $\Omega$  resistor has been installed in series with

## 5. Aluminum logic laser system

the capacitance of the actuator to form a low-pass filter with a cut-off frequency of 21.2 kHz.

Ideally the enhancement cavity is resonant only for a single PL mode which is correlated to efficient SHG. However, in practice multiple resonances can occur. To discriminate between these, the system provides an auxiliary input port to connect a photodiode monitoring the circulating power ("power photodiode" in Fig. 5.4). Moreover, the controller is equipped with an automatic integrator reset.

## 5.5. Experiment

### Gas supply

To prevent contamination of the crystal facets the cavity was flushed with 99.95% pure oxygen at a rate of 22 mL/min. For a transportable system, it is required to bring a gas supply along with the rest of the setup that is capable of feeding ideally multiple cavities for the duration of the transport itself and also the measurement campaign. Since a standard 50 L 300 bar gas bottle can maintain the given flow rate through a single cavity for more 400 days, gas purging of the crystal is no practical limitation for the operation of a transportable optical clock housed in a container.

### Finesse

A finesse  $F_{\text{meas}} = 317$  was measured with the Brewster-cut BBO crystal in place and mirrors with reflectivities of  $R_1 = 98.5\%$  and  $R_2 = R_3 = R_4 = 99.95\%$ .

### Long term stability

For many applications in quantum optics a powerstable UV source is required that reliably stays in lock over many hours. For instance, an ion clock achieving  $1 \times 10^{-16} \tau^{-1/2}$  statistical frequency uncertainty requires 10 000 s averaging time to reach  $1 \times 10^{-18}$ . In order to demonstrate that our setup fulfills those requirements, it has been locked over 130 h during which the PL power and SHG Power have been recorded every 1 s using two power meters<sup>8</sup>, cf. Fig. 5.4. Fig. 5.5 shows the measured SHG output power scaled to the average SHG power (red) and to the instantaneous PL power (blue). The SHG power stayed on a level of about 186 mW, while the cavity

---

<sup>8</sup>Thorlabs PM100D with S130VC Sensor and Ophir Vega with PD300-UV Sensor

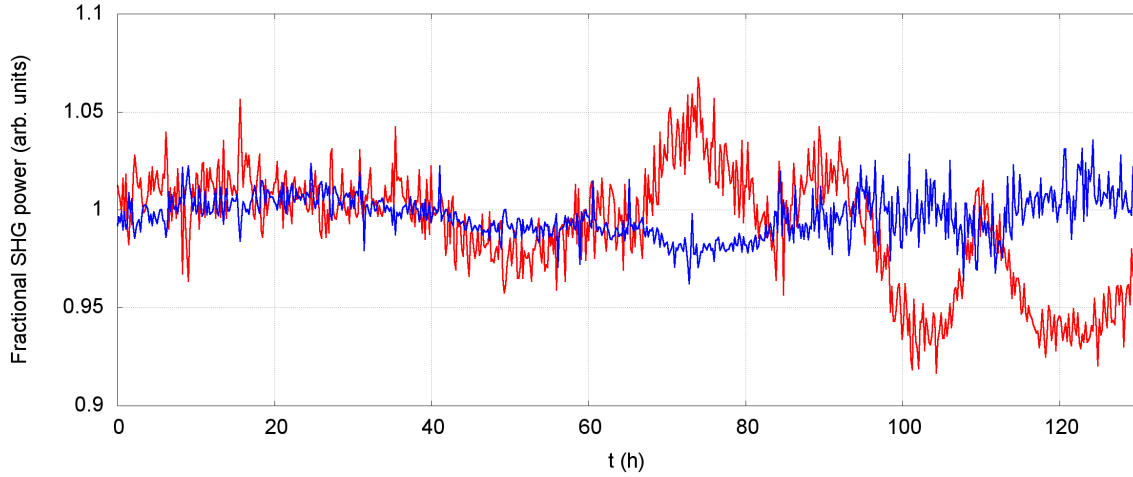


Figure 5.5.: Long term SHG output power measurement at 313 nm. Red: measured SHG power, a power of "1" equals 186 mW. Blue: SHG normalized to the PL power squared as a measure of the conversion efficiency. From [Hannig et al., 2018a].

was pumped with about 530 mW PL. The SHG power fluctuates by about 7% peak-to-peak (3% rms) around its mean value on a few hour timescale, while the SHG power rescaled to the PL varies only by 3% peak-to-peak (1% rms). This suggests that the SHG power fluctuations were mainly caused by pump power fluctuations, indicating that the alignment of the cavity did not change on relevant length or angular scales over the duration of the measurement.

To the knowledge of the author, this is the longest published in-lock operation of a resonant SHG ring cavity. The output power of the SHG cavity fully agrees with the corresponding measurement and calculation presented by [Wilson et al., 2011].

### Lock performance

A broad resonance at about 17 kHz sets the upper limit for the locking bandwidth in this setup. This frequency is likely to be the first mechanical resonance of the small mirror, the piezoelectric actuator, and its holder. In a future setup, it could possibly be improved by applying the mount design presented in [Jitschin and Meisel, 1979, Briles et al., 2010, Goldovsky et al., 2016], since Equ. 5.14 results in an upper limit of  $f^* \approx 120$  kHz for the piezo electric actuator and mirror used here.

### Acceleration sensitivity tests

In order to prove the suitability of the doubling cavity for such an application, the entire breadboard was accelerated in vertical direction while the cavity length was locked to the pump laser wavelength. For the acceleration measurement a MEMS sensor<sup>9</sup> was glued on the top lid of the cavity, providing an analog output voltage proportional to the momentary acceleration. A photodiode<sup>10</sup> was employed to measure the SHG power. Both signals were recorded simultaneously at a rate of 600 Hz using a 14bit/10 V analog to digital conversion system<sup>11</sup>, achieving sub-mg resolution. Fig. 5.6 shows the output power and vertical acceleration versus time. The measurement shows temporary SHG power drops of about 10 % synchronous with the acceleration acting on the system. While an absolute acceleration of up to 1 g was obtained, the cavity stayed in lock and fully recovered the initial SHG power after the acceleration stopped.

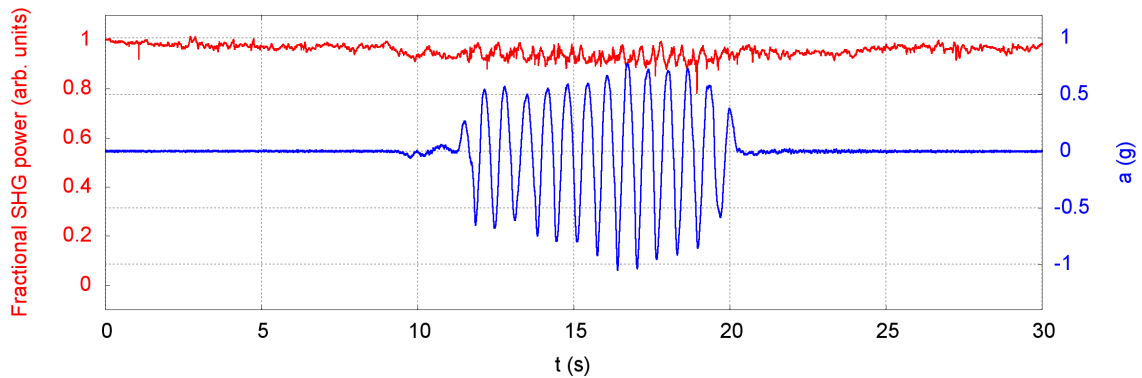


Figure 5.6.: Cavity SHG output power and acceleration versus time during acceleration excitation in vertical direction. Red: SHG power, blue: vertical acceleration. For accelerations up to 1 g (gravity subtracted) the SHG output power fluctuates on the 10 % level while the cavity stays in lock. From [Hannig et al., 2018a].

In order to demonstrate the reliable operation of the system after transport, it was exposed to an acceleration profile typical for on road transportation. Therefore, the system was optimized first and then the SHG breadboard was placed on a multi-component acceleration exciter [PTB Working Group 1.71, 2017] and exposed to a vibration power spectrum in the vertical direction according to ISO 13355:2016 with a total acceleration of  $0.604 g_{\text{rms}}$  for 30 minutes. Afterwards, the SHG breadboard

<sup>9</sup>ADXL345

<sup>10</sup>Thorlabs XYZ

<sup>11</sup>DT98824 USB Data Acquisition Modul



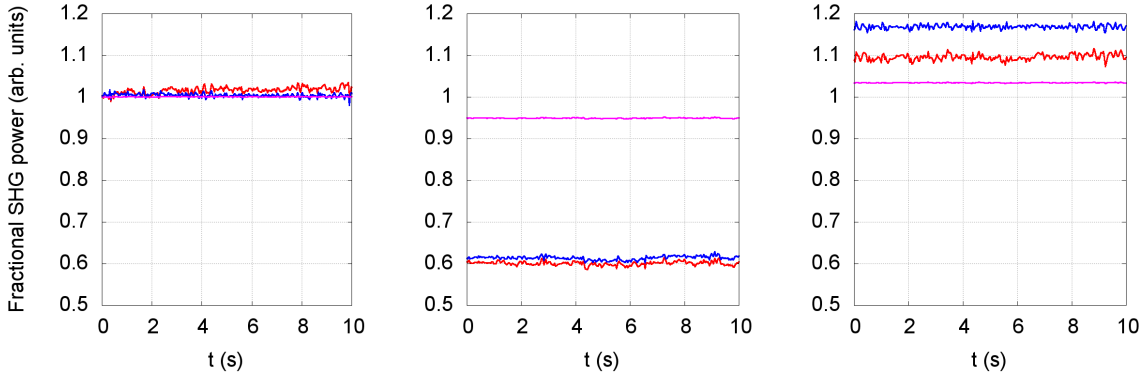


Figure 5.7.: SHG power before (left) and right after (middle) being exposed to a 30 min ISO 13355:2016 shaker test. Right: following optimization of the incoupling beam after the shakertest. Red: measured SHG power, blue: SHG normalized to the PL power squared, pink: SHG normalized to the circulating PL power as a measure of the conversion efficiency. From [Hannig et al., 2018a].

was reconnected to the rest of the system and locked without further realignment or optimization. The results are shown in Fig. 5.7. The obtained SHG power normalized to the pump power dropped to about 60 %, while the SHG power normalized to the squared pump power circulating in the cavity remained almost constant. Since this indicates a drop in incoupling efficiency, the alignment of the mirrors M1 and M2 in Fig. 5.2(b) was optimized, resulting in approximately the same SHG power as before the acceleration exposure test. This strongly indicates that the alignment of the cavity itself was not substantially affected by the shaking test. Therefore, the same test was repeated with five times the original acceleration ( $3.020 g_{\text{rms}}$ ), also resulting in the same SHG output power after shaking and alignment correction of the mirrors M1 and M2. From these measurements was concluded that the optical alignment of the cavity itself can withstand typical on road transport situations without any deterioration, while the mechanical stability of the input coupling optics and/or fiber connector for the PL needs to be improved.

### 5.5.1. SHG to 267 nm in the first generation cavity

The SHG cavity design presented up to here provided constant output power over 130 h at a wavelength of 313 nm. For  $^{27}\text{Al}^+$  logic light generation, the same type of cavity was set up for 267 nm by using mirrors with suitable coatings and a BBO crystal cut under the phasematching angle for that wavelength. When the first

## 5. Aluminum logic laser system

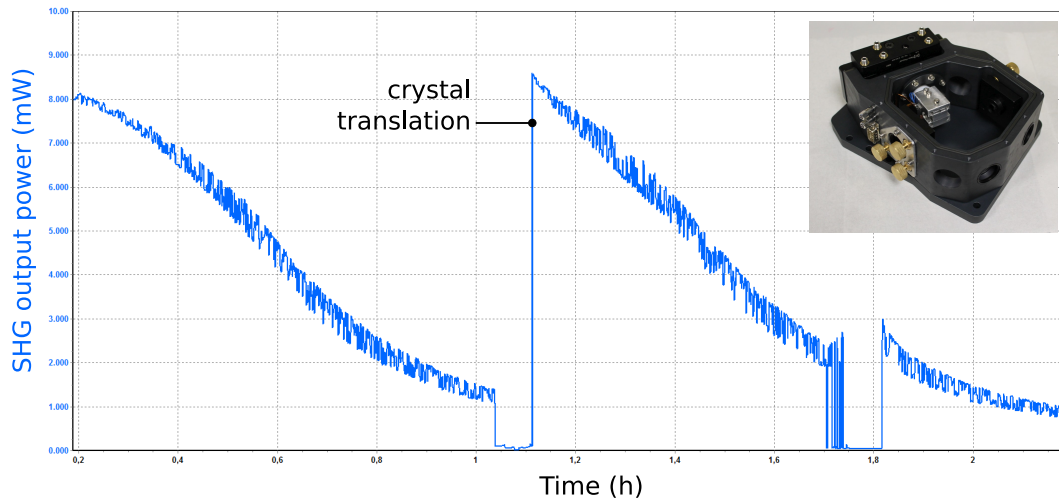


Figure 5.8.: 267 nm output power of the first generation SHG cavity versus time for about 300 mW pump power. After about 1 h, the crystal was translated parallel to the front facet, changing the crystal surface and volume interacting with the pump beam. The inset shows the first generation SHG cavity.

output power stability tests were performed, SHG power decayed by about 85% on a timescale of one hour, cf. Fig. 5.8. The output power was repeatedly fully recovered to the initial value by translating the BBO crystal orthogonal to the pump beam. This output power decay was observed for several individual crystals from different fabrication batches. It was correlated to spot formation on the crystal entrance facets as shown in Fig. 5.9.

In some cases the crystals' front and rear facet had been cleaned by wiping with spectral grade diethyl ether and/or spectral grade ethanol in order to remove possible contamination from these surfaces, as suggested by crystal manufacturers<sup>12</sup>. Moreover, the cavity was flushed with oxygen providing an over-pressure inside and therefore preventing potentially harmful substances from entering the cavity. Since both measures did not prevent the decay in output power the hypothesis was proposed that at least one substance that leads to crystal degradation could be part of the cavity itself. As degradation was also observed for crystals with protective coatings, such substances could even be embedded the BBO bulk material surface. In conclusion, further investigations on the exact reasons of the decay are required. This includes an extensive search for so called *sweet spots* on the crystal surface,

<sup>12</sup>Wet cleaning of BBO crystals using ether and ethanol is recommended by <http://www.unitedcrystals.com/faq.html> and [http://www.foctek.net/products/crystals/-NLO\\_Crystals.htm](http://www.foctek.net/products/crystals/-NLO_Crystals.htm)

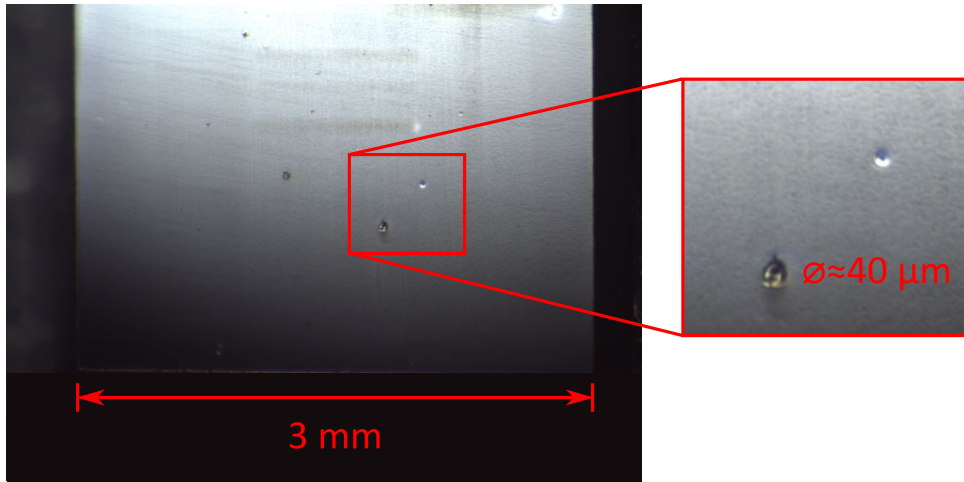


Figure 5.9.: Optical microscope photo of a BBO crystal front facet used for SHG at 267 nm in the first generation SHG cavity. The crystal has been translated parallel to the facet several times, see also Fig. 5.8. Several surface defects of a few 10  $\mu\text{m}$  size can be identified.

where no degradation takes place. If such spots were found, this would indicate that the degradation behavior depends on properties of the crystal facets.

### 5.5.2. Summary of the first generation SHG cavity

A mechanically stable monolithic enhancement cavity for SHG in the UV was demonstrated, including in-lock SHG power measurements during acceleration excitation. Less than 10% SHG power reduction during exposure of up to 1 g were observed with full recovery of the initial SHG power after acceleration stopped. It was shown that the cavity optical alignment can withstand 30 minutes of acceleration excitation with 3.020  $g_{\text{rms}}$ . This is five times the acceleration amplitude as specified in the corresponding ISO13355:2016 norm, demonstrating the suitability for transportable experiments. 130 h uninterrupted operation without decay in output power at 313 nm was demonstrated. During this time the SHG power scaled to the pump power fluctuated by 1% rms. Moreover, the oxygen flow rate of 22 mL/min applied during these tests can be maintained by a standard gas bottle for longer than a year and therefore does not limit the in-field operation of the SHG setup.

However, the first generation SHG cavity is not capable of generating output power at 267 nm that is stable on timescales that are relevant for quantum optics experiments. Therefore, an improved version has been developed which is presented in the next section.

## 5.6. Second generation UV SHG cavity

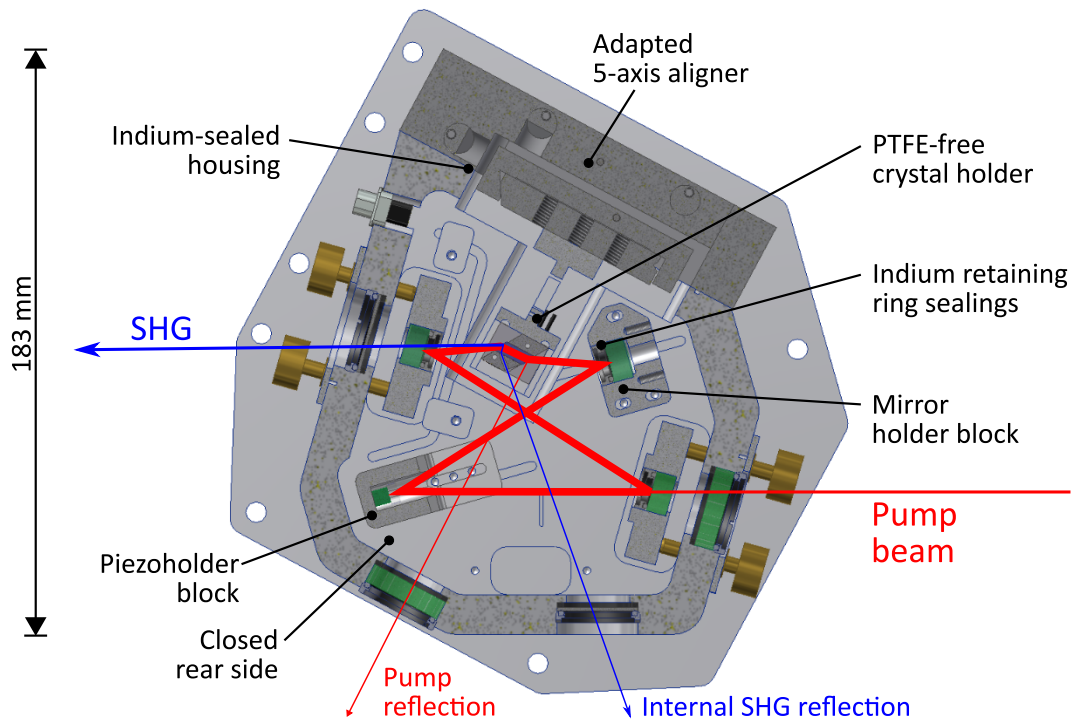


Figure 5.10.: Horizontal cross section of the second generation UV SHG cavity. Changes compared to the first generation shown in Fig. 5.3 are labeled in black. These aim to provide a interior free of any potentially out-gassing material at increased mechanical robustness.

Fig. 5.10 shows a cross section of the second generation UV SHG cavity with all changes compared to the first generation, cf. Fig. 5.3. The cavity housing and all interior parts have been left unanodized in order to prevent outgassing from any substances deposited in the anodization layer. For the same reason indium has been used instead of rubber for all sealing purposes and also as soft part of the stress free retaining rings which hold the cavity mirrors in place. As precaution also the thermal insulation made of PTFE between the crystal holder and the aligner was removed. Moreover, the holder for the piezo-actuated mirror and the curved mirror in front of the crystal were implemented as rigid blocks attached directly to the monolithic frame. Its rear side is now closed to avoid one sealing and provide more mechanical stability than in the first generation. Moreover, the 5-axis aligner was changed against a self build version that is simpler to seal. Additionally, now the

lubricant<sup>13</sup> of the aligner was chosen to be the same as for the fine-threaded screws actuating the mirror holders.

The second generation SHG cavity became part of the  $^{27}\text{Al}^+$  logic laser system at IQLOC1 which is described and characterized in the next section.

## 5.7. Aluminum logic laser setup

Fig. 5.11 shows a schematic overview of the  $^{27}\text{Al}^+$  logic laser system. 40 mW light at 1068 nm are emitted from an ECDL<sup>14</sup>. Behind an optical isolator, 10 % of the light are split to a WLM for frequency monitoring and a transfer beat [Scharnhorst et al., 2015] to generate an error signal to lock the 1068 nm ECDL to the aforementioned highly stable reference laser at 1542 nm. The remaining 90 % of the laser power seed a fiber laser amplifier<sup>15</sup>; its characteristic curve is given in Fig. A.2 in the appendix. The output power is coupled in a fiberized single pass SHG module (SP-SHG) based on a waveguide in quasi-phasematched periodically poled lithium niobate (PPLN), which is temperature stabilized for maximum conversion efficiency. Fig. A.3 in the appendix shows the output versus input power of the module. The output power was measured behind a dichroic beam splitter which separates the remaining IR light transmitted through the output fiber from the SHG light. For the maximum specified input power of 1 W at 1068 nm, the module produces approximately 320 mW at 534 nm.

The second doubling stage from 534 nm to 267 nm is similar to the already presented setup for SHG of 626 nm, but here the second generation doubling cavity introduced in Sec. 5.6 is employed. Again, the cavity length is stabilized to the pump light wavelength via the HC-lock using the digital PI controller implemented in the STEMLab-box. The BBO crystal inside the SHG cavity was uninterruptedly purged with  $\text{O}_2$ . Fig. A.4 in the appendix shows the results of a first test. Approximately 10 mW output power were obtained for 300 mW pump power. This power level remained constant for almost one hour. For standard operation, the pump power was reduced to about 170 mW and the alignment of the cavity was optimized. The SHG power remained at a level of  $(5.2 \pm 0.4)$  mW over two months<sup>16</sup>, when the laser system was operated for a few hours per day.

---

<sup>13</sup>DuPond Krytox™

<sup>14</sup>Toptica DL Pro

<sup>15</sup>NKT Boostik

<sup>16</sup>Power stability according to J. Kramer, PTB, 2018, private communication.

## 5. Aluminum logic laser system

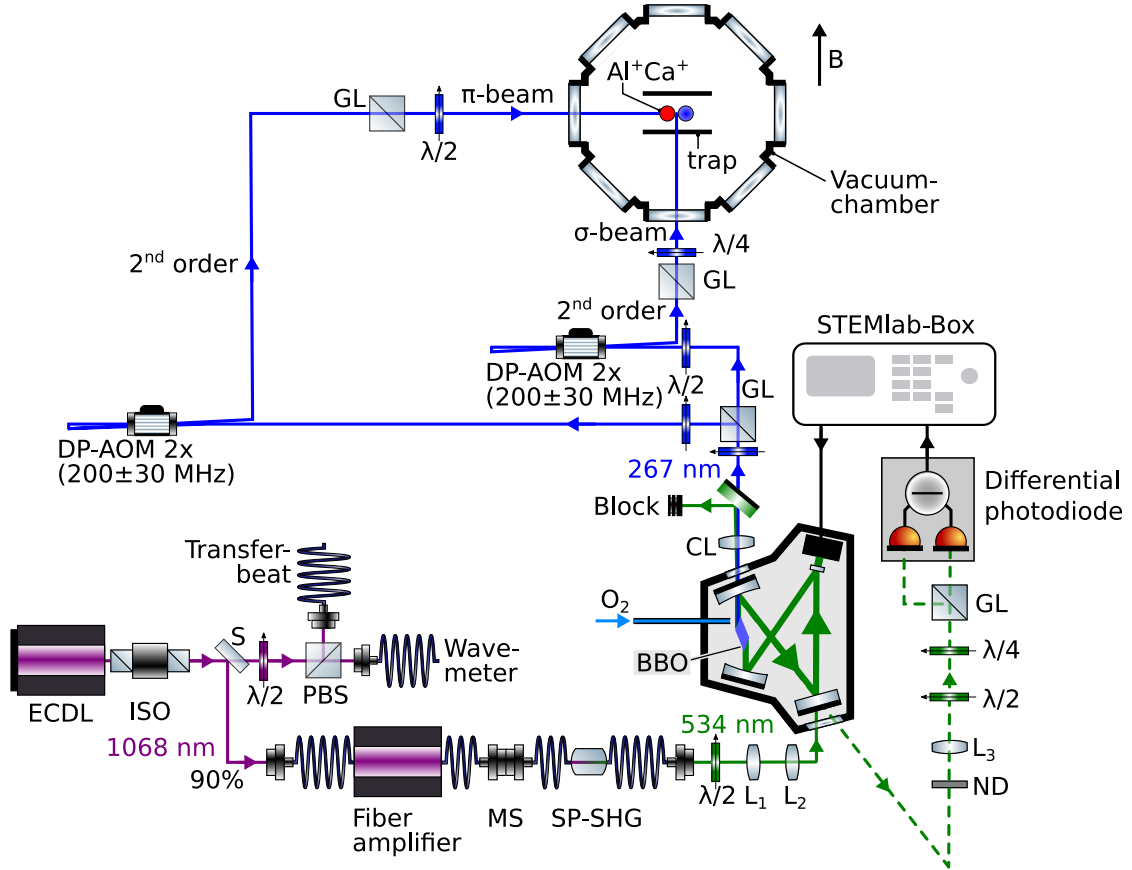


Figure 5.11.: Schematic overview of the 267 nm  $^{27}\text{Al}^+$  logic laser system at the stationary  $^{27}\text{Al}^+$  clock setup. An amplified 1068 nm ECDL is frequency doubled in a single-pass PPLN waveguide SHG module (SP-SHG). Afterwards, the resulting light is power-enhanced and frequency-doubled in a resonant bowtie-cavity, that is locked to the pump wavelength via the HC-lock. The generated light at 267 nm is split into two beams which are frequency shifted by individual DP-AOMs, polarization cleaned and then circular/linear polarized ( $\sigma/\pi$ -beam). For simplification some lenses, mirrors, and all laser beams at other wavelengths are not depicted. CL: cylindrical lens, GL: Glan Laser, ISO: optical isolator,  $L_i$ : lens, MS: mating sleeve, PBS: polarizing beam splitter, S: beamsplitter,  $\lambda/n$ : waveplate. Some components in the figure are adapted from [Franzen, 2009].

Behind the SHG cavity, a dichroic mirror separates residual pump light from the SHG which is then split into two beams with individual DP-AOMs for frequency tuning in the range of  $\pm 50$  MHz. Afterwards, both beams are directed towards the vacuum chamber, where their polarization is cleaned in GL polarizers. A quarter-wave-plate in one of the beams generates circular polarized for  $^{27}\text{Al}^+$  state prepara-

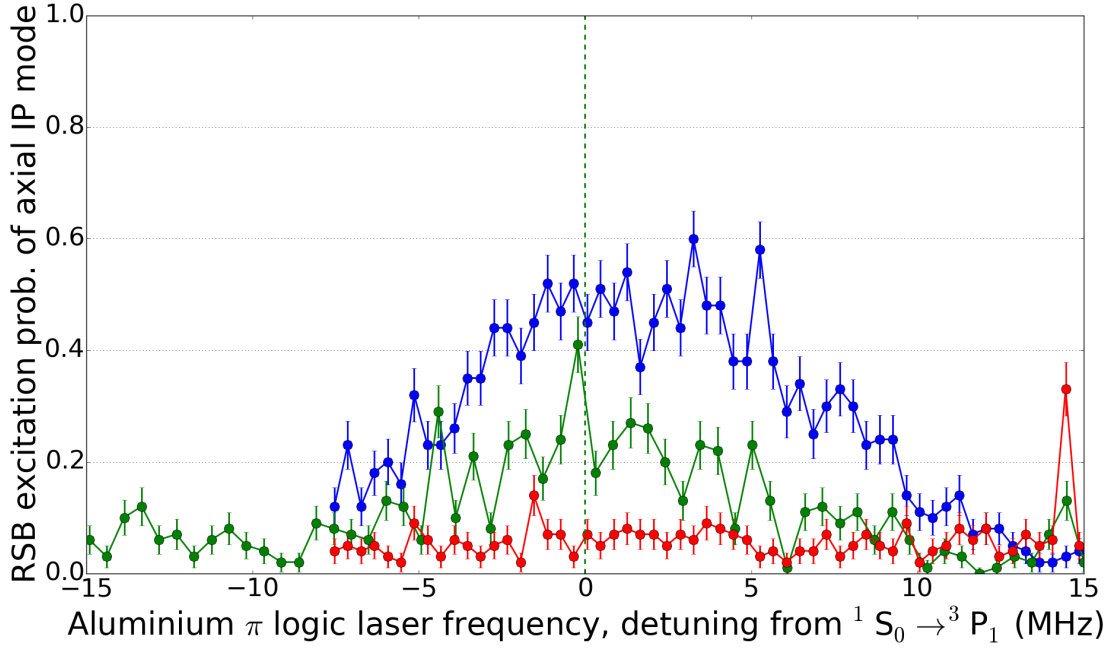


Figure 5.12.: Spectroscopy on the  $^1S_0 \rightarrow ^3P_1$  logic transition in  $^{27}\text{Al}^+$ . Shown is the excitation probability of the axial RSB of the IP mode of an  $^{27}\text{Al}^+ / ^{40}\text{Ca}^+$  crystal for an increasing laser power (red to green to blue curve). Driving the transition resulted in heating of the crystal that caused an increase in the RSB excitation probability.

tion via optical pumping, while the other beam stays linear polarized and is employed as  $\pi$ -beam.

Fig. 5.12 presents the results of spectroscopy on the  $^1S_0 \rightarrow ^3P_1$  logic transition in  $^{27}\text{Al}^+$  with different laser powers using the 267 nm laser system presented here. Shown is the excitation probability of the 729 nm RSB of the IP motional mode as function of the logic laser frequency detuning. After both axial motional modes had been cooled to the ground state, the frequency of the 267 nm  $\pi$ -beam was scanned across the resonance of the logic transition with different laser powers. When the logic laser was on resonance, the crystal was heated up and therefore the excitation probability of the RSB increased.

In conclusion, a laser system for UV generation at 267 nm via cascaded SHG generation of 1068 nm light has been built and employed at the stationary  $^{27}\text{Al}^+$  clock setup for spectroscopy on the  $^1S_0 \rightarrow ^3P_1$  logic transition in  $^{27}\text{Al}^+$ .

For the second SHG stage a mechanically stable monolithic enhancement cavity was developed that can withstand 1 g vertical vibration excitation in lock and 30 minutes at  $3.020 g_{\text{rms}}$  unlocked without the necessity of cavity optics realign-

## 5. Aluminum logic laser system

ments. Additionally, 130 h uninterrupted operation without decay in output power at 313 nm have been demonstrated. At 267 nm the SHG output power level has been stable over a timescale of months while the system was operated for a few hours per day on average. Therefore, the presented laser system is applicable for transportable optical  $^{27}\text{Al}^+$  clocks.

It has to be emphasized that the basic cavity design can easily be adapted to other resonator geometries in order to install crystals of different materials or shapes. One example is a cavity design for SHG of IR in Periodically Poled Lithium Niobate (PPLN) crystals which is shown in Fig. A.5 in the appendix. For SHG from 882 nm to 442 nm, a conversion efficiency of 85.7% was achieved at an output power level of 25.3 mW<sup>17</sup>.

Lastly, the locking bandwidth of the setup presented here was measured to be 17 kHz, other groups demonstrated piezoelectrically actuated mirror mounts allowing for one order of magnitude higher locking bandwidth [Jitschin and Meisel, 1979, Briles et al., 2010, Goldovsky et al., 2016] that could be adopted in the SHG cavity presented here.

---

<sup>17</sup>Results according to S. King, PTB, 2018, private communication.







# 6. Summary and Outlook

## 6.1. Summary

The principal objective of this thesis was to develop a setup for a transportable ion quantum logic optical clock which reaches a systematic fractional frequency uncertainty in the low  $10^{-18}$  range employing  $^{27}\text{Al}^+$  as clock and  $^{40}\text{Ca}^+$  as logic ion. Key demands to facilitate transportability and operation in the field were:

- Compactness and modularity of the setup to fit into a climatized standard 20 foot container.
- High robustness against typical conditions of on-road and airborne transportation to reduce the start-up time after transportation as far as possible.
- Self-sufficient operation of the setup except for a power supply and an optical fiber for frequency comparisons.

A segmented multi-layer Paul trap made of Rogers<sup>TM</sup> [Herschbach et al., 2012] has been set up for the confinement of ions. It allows for the use of distinct loading and spectroscopy zones, which reduces the risk of micromotion caused by unisotropic deposition from the neutral atom beams used for loading. Additionally, several ion ensembles can be trapped simultaneously, which allows for dead time-free interrogation of two clocks [Schioppo et al., 2017] in the same trap or future multi-ensemble protocols [Rosenband and Leibbrandt, 2013, Borregaard and Sørensen, 2013]. The neutral atom beams are generated by pulsed laser ablation from solid targets. Ions are generated by subsequent photoionization inside the trap volume.

A compact vacuum system entirely made out of titanium alloy simplifies magnetic field compensation due to its low distortion of external fields, cf. Sec. 3.4. The  $^{40}\text{Ca}^+$  laser system is composed of ECDLs and one DFB laser, directly emitting the required wavelengths. Therefore, the system is simple and compact, especially due to the all-fiberized  $^{40}\text{Ca}^+$  repumper laser system, cf. Sec. 3.6. Moreover, the entire

## 6. Summary and Outlook

laser setup is built on stackable breadboards connected by optical fibers and thus is modular.

All  $^{40}\text{Ca}^+$  lasers with the exception of the logic laser have sufficiently narrow linewidths for their application in an  $^{27}\text{Al}^+ / ^{40}\text{Ca}^+$  clock, but suffer from frequency drifts. Therefore, these lasers are stabilized to a thermally shielded wavelength meter for reduced complexity compared to a solution based on multiple reference cavities. Due to its drift of below 0.2 MHz calibrated at wavelengths of 397 nm and 729 nm, it can operate over several hours without interruption for calibration, cf. Sec. 3.6.1.

For state discrimination via electron shelving detection fluorescence light from  $^{40}\text{Ca}^+$  is collected with a single biaspheric lens, covering 7% solid angle seen by the ion with its numerical aperture  $NA = 0.51$ . The collected photons are split such that 10% goes onto a compact sCMOS camera, giving sub- $\mu\text{m}$  spatial resolution and a signal-to-noise ratio of 806.1 for 300 ms exposure time. The remaining 90% are sent onto a PMT. A state discrimination error of below 0.2% is achieved for 25  $\mu\text{s}$  detection time. It improves to below  $10^{-5}$  for 100  $\mu\text{s}$ , cf. Sec. 3.9.

The Al neutral atom beam generated by pulsed laser ablation was characterized by TOF measurements. After parameter optimization to obtain a maximum atom yield for a specific ablation laser pulse energy, the latter was reduced to a level allowing for single  $^{27}\text{Al}^+$  ion loading.  $^{27}\text{Al}^+$  is not directly laser cooled, but only sympathetically via Coulomb coupling to a co-trapped  $^{40}\text{Ca}^+$  ion. The single ion secular frequencies are mass dependent and therefore different for  $^{27}\text{Al}^+$  and  $^{40}\text{Ca}^+$ , hence the energy transfer from a hot  $^{27}\text{Al}^+$  to a crystallized  $^{40}\text{Ca}^+$  ion takes a long time compared to  $^{40}\text{Ca}^+$  crystallization. To reduce the initial kinetic energy of the  $^{27}\text{Al}^+$ , pulsed photoionization was implemented for selective loading of low velocity ions. A crystallization time of  $(231 \pm 102)$  s was measured. An assessment of the contributions to the initial kinetic energy of the  $^{27}\text{Al}^+$  ion yields that the average crystallization time is defined by the extent of the neutral atom beam along the direction of the trap axis.

Chap. 4 reports on the ground state cooling performance employing pulsed sideband cooling. The measured heating rates of below 10 phonons per second for all three motional modes of a single  $^{40}\text{Ca}^+$  ion allow for interrogation times of a few hundred milliseconds without the necessity for simultaneous sympathetic cooling in a future  $^{27}\text{Al}^+ / ^{40}\text{Ca}^+$  quantum logic optical clock. After compensation of excess micromotion using the sideband spectroscopy method, a total remaining rf electric

field of  $(23.5 \pm 5.3) \text{ V m}^{-1}$  was measured at the trap center, cf. Sec. 4.2.

The partial error budget for an  $^{27}\text{Al}^+ / ^{40}\text{Ca}^+$  clock operated in the setup was derived from the previous measurements by rescaling the mass-dependent shifts, cf. Sec. 4.3. From trap chip temperature data recorded during rf heating the BBR shift was calculated. The last shift considered here is caused by phase distortions due to Langevin collisions with background gas particles and has been estimated based on their collision rate inferred from the average observed reordering frequency of  $^{27}\text{Al}^+ / ^{40}\text{Ca}^+$  crystals. All individual systematic fractional frequency uncertainties are below  $1.0 \times 10^{-18}$ , except for the collisional shift. The combined estimated systematic fractional frequency uncertainty of the error contributions investigated in this work is  $1.7 \times 10^{-18}$ , which is equivalent to approximately 2 cm height resolution, assuming that other shifts are negligible, cf. Sec. 4.3.

Apart from the aforementioned clock setup, an  $^{27}\text{Al}^+$  logic laser system for 267 nm light generation for PTB's stationary  $^{27}\text{Al}^+$  clock setup was built by amplifying and frequency quadrupling an ECDL operating in the IR, cf. Chap. 5. For the second frequency doubling stage, an enhancement cavity was developed that is suitable for SHG up to the mid-UV in 10 mm-long BBO crystals.

Several different cavities of this type were built and characterized. For a cavity generating 186 mW output power at 313 nm from 530 mW input power, 130 h uninterrupted operation without any decay in output power has been demonstrated, cf. Fig. 5.5. Moreover, the output power of this cavity was reduced by a maximum of only 10 % during exposure to 1 g vertical acceleration and the optical alignment was proven to withstand  $3 g_{\text{rms}}$  of continuously applied vertical acceleration excitation for 30 minutes without significant misalignment, cf. Sec. 5.5. This is five times the acceleration amplitude as specified in the corresponding ISO13355:2016 norm, which demonstrates the suitability for transportable application.

After the SHG cavity design had been refined in terms of the used materials and the gas sealing to avoid crystal degradation at shorter wavelengths, which has been observed in many SHG setups at various groups, it was employed in the  $^{27}\text{Al}^+$  logic laser system providing  $(5.2 \pm 0.4) \text{ mW}$  output power at 267 nm generated from 170 mW input power. For an average daily operation time of a few hours, no degradation was observed over a period of more than two months, cf. Sec. 5.7. This enabled spectroscopy of the  $^{27}\text{Al}^+$  logic transition  $^1\text{S}_2 \rightarrow ^3\text{P}_1$ , cf. Fig. 5.12.

The basic cavity design can easily be adapted to other resonator geometries and crystal types. E.g. a cavity for SHG of 882 nm in a Periodically Poled Lithium

## 6. Summary and Outlook

Niobate (PPLN) crystal reaches a conversion efficiency of 85.7%, cf. Fig. A.5.

In conclusion, a compact and mechanically robust setup for a transportable  $^{27}\text{Al}^+ / ^{40}\text{Ca}^+$  clock has been developed, built, and characterized. An estimated systematic fractional frequency uncertainty of  $1.7 \times 10^{-18}$  was inferred from mass-scaled measurements using a single  $^{40}\text{Ca}^+$  ion and taking into account the expected dominant frequency shifts. Neglecting other possible shifts and their uncertainties this is equivalent to a height resolution of approximately 2 cm obtainable by chronometric leveling.

### 6.2. Outlook

At the time of writing,  $^{27}\text{Al}^+$  ions can be loaded in the transportable  $^{27}\text{Al}^+ / ^{40}\text{Ca}^+$  clock setup. Hence, a second set of  $^{27}\text{Al}^+$  laser systems will be built to complete the transportable system. Moreover, an active magnetic field stabilization is required to suppress fluctuations of external magnetic fields that lead to decoherence between the laser fields and the ion. Additionally, it can suppress systematic inaccuracies from slowly drifting external fields.

During the experiments reported in this thesis, ground state cooling of a single  $^{40}\text{Ca}^+$  ion was achieved through pulsed sideband cooling, which can only cool one motional mode at a time. The resulting long cooling time leads to a low clock duty cycle. While continuous sideband cooling promises a moderate reduction of the required cooling time, single EIT cooling allows for cooling of two radial modes with the same laser settings.

In this thesis, an average  $^{27}\text{Al}^+$  crystallization time of  $(231 \pm 102)$  s was measured. The potential energy due to an axial displacement of the Al from the trap center during ionization was identified as the main contribution to the total initial energy of the  $^{27}\text{Al}^+$ . While a tighter collimation of the atom beam in the direction of the trap axis would require hardware changes inside the vacuum chamber, a tighter radial confinement could improve cooling in the axial direction. Moreover, bunching of single ion  $^{40}\text{Ca}^+$  and  $^{27}\text{Al}^+$  trap frequencies could feature resonant energy exchange between the ions and therefore lead to reduced  $^{27}\text{Al}^+$  crystallization times.

In contrast to these incremental technical improvements, major improvements on the clock error budget could be achieved by exchanging the trap against a similar design made of AlN [Keller, 2015]. This ceramic material is much stiffer than the Rogers<sup>TM</sup> Material used here. The reduced bending of the chips could result in a

trap whose geometry deviates less from theory than for the current material. In this case, the axial excess micromotion is expected to be less sensitive to the ion position than at the time of writing. Therefore, the second order Doppler shift due to excess micromotion and its uncertainty should be reduced. Moreover, the outgassing rate of AlN is lower than that of Rogers<sup>TM</sup>, which potentially reduces the background gas pressure, resulting in smaller shifts due to Langevin collisions and longer ion storage times. Last but not least, its much higher heat conductivity results in a lower average temperature of the environment "seen" by the ion and therefore a smaller uncertainty of the BBR shift.

After the reduction of the clock error budget a faster averaging down to the minimum obtainable systematic fractional frequency uncertainty level is desirable. This could be achieved e.g. by stabilizing the  $^{40}\text{Ca}^+$  logic laser to a large crystal of dynamically decoupled  $^{40}\text{Ca}^+$  ions and transferring the stability of that laser to the  $^{27}\text{Al}^+$  clock laser via a transportable frequency comb. With the prestabilized clock laser the interrogation time could be increased, which yields a reduction of the statistic fractional frequency uncertainty. Another option is to load multiple  $^{27}\text{Al}^+ / ^{40}\text{Ca}^+$  crystals in different trap zones to stabilize the  $^{27}\text{Al}^+$  clock laser on one of the  $^{27}\text{Al}^+$  ions. Then, a second  $^{27}\text{Al}^+$  ion can be interrogated for a longer time. This approach is in literature referred to as *cascaded clock scheme*. Furthermore, the statistic fractional frequency uncertainty can be reduced by employing a crystal consisting of multiple possibly entangled  $^{27}\text{Al}^+$  and  $^{40}\text{Ca}^+$  ions, ideally combined with a readout technique that only requires a logarithmic overhead in  $^{40}\text{Ca}^+$  ions [Schulte et al., 2016] to minimize the axial extent of the crystal and therefore the EMM second order Doppler shift as far as possible.

Once both  $^{27}\text{Al}^+$  clocks at PTB are operational, a side-by-side comparison of the systems can be carried out before the hardware of the transportable system is moved into a container, cf. Fig. 3.27. Afterwards, a second comparison of the stationary and transportable clock should allow measurement of the gravitational red shift which is expected to result in a fractional frequency difference of approximately  $10^{-15}$  due to the change in height offset of about 10 m between the transportable clock in the container on ground-level and the stationary clock on the fifth floor of the laboratory building.

After these preparatory steps, the transportable clock can be operated at geodetically relevant sites such as offshore islands without direct line of sight to reference points on the mainland. Then, frequency comparisons to the stationary clock or

## 6. Summary and Outlook

a second transportable clock such as the PTB  $^{87}\text{Sr}$  clock allow for chronometric leveling with an expected height resolution in the few-cm range. Since the lateral resolution of chronometric leveling measurements is below 1 m, the transportable  $^{27}\text{Al}^+$  clock could help to significantly refine existing geoid maps derived from satellite measurements. When these new high resolution geopotential data is combined with gravimetry measurements, underground processes such as magma or water transport phenomena could be better understood.

Moreover, the transportable clock allows for frequency comparisons among distant stationary optical clocks that are not connected via length-stabilized optical fibers by subsequent side-by-side frequency comparisons. Concretely, employing the transportable  $^{27}\text{Al}^+$  clock, all stationary clocks under development at various metrology institutes worldwide could subsequently be compared to demonstrate consistency in estimated systematic fractional frequency uncertainty on an unprecedented level. In that case, the transportable  $^{27}\text{Al}^+$  clock could contribute to pave the way towards a redefinition of the second based on an optical atomic transition.







# A. Appendix

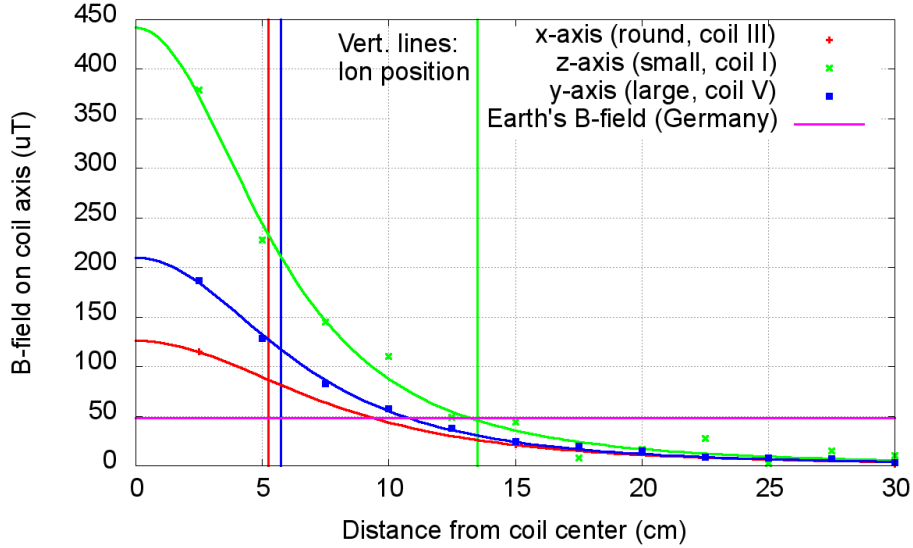


Figure A.1.: Characterization of the B-field coils. Shown are the measured magnetic fields on the axis of individual single coils for a current of 1 A. The coils were not mounted around or near the vacuum chamber, but on an optical table. Vertical lines indicate the ion’s distance from the coil center, once the coils are mounted around the chamber. The function  $f(x) = a / (\sqrt{b^2 + x^2})^3$  modeling the on-axis B-field of a round has been used as fit function in all three cases for simplicity.

Table A.1.: Parameters of the B-field coils. All coils are made of 1.0 mm diameter copper wire wound around an aluminum frame.

Direction	Dimensions (mm <sup>2</sup> )	No. of windings	Distance from ion mm
x	∅ = 222 (round)	20	52.5
y	284 × 152	25	58
z	150 × 88	60	135

Table A.2.: Dimensions of the helical resonator.

Parameter	front surface
Turns primary coil	2.5
Turns secondary	9
Diameter primary coil	$\approx 40$ mm
Diameter secondary coil	45 mm
Length primary coil	$\approx 10$ mm
Length secondary coil	86 mm
Shield inner diameter	95 mm

Table A.3.: Biaspherical lens surface profile parameters according to ISO 10110. The front surface points towards the ion trap, cf. Fig. 3.13. From [Hannig et al., 2018b].

Parameter	front surface	rear surface
$R$ (mm)	75.461975	25.657609
$k$	-13.754	-0.88586
$A_4$ (mm <sup>-3</sup> )	$-1.8442 \times 10^{-6}$	$1.8439 \times 10^{-6}$
$A_6$ (mm <sup>-5</sup> )	$1.2836 \times 10^{-9}$	$7.4104 \times 10^{-10}$
$A_8$ (mm <sup>-7</sup> )	$1.2836 \times 10^{-9}$	$2.7227 \times 10^{-13}$

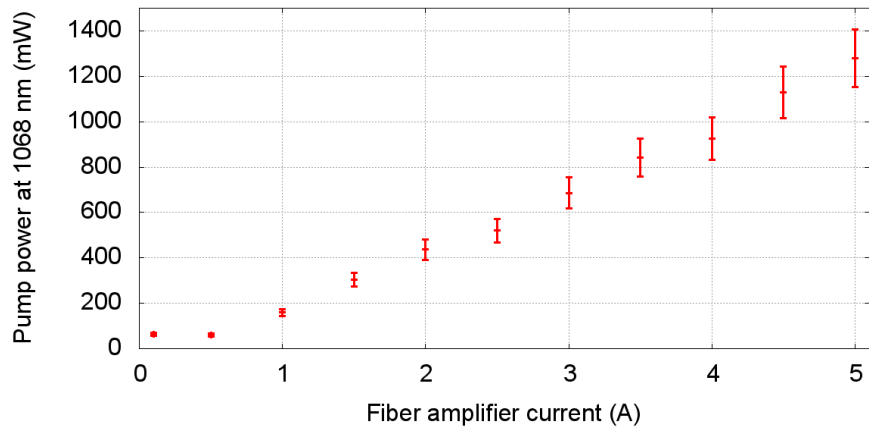


Figure A.2.: Output power of the 1068 nm fiber amplifier as function of the pump diode current.

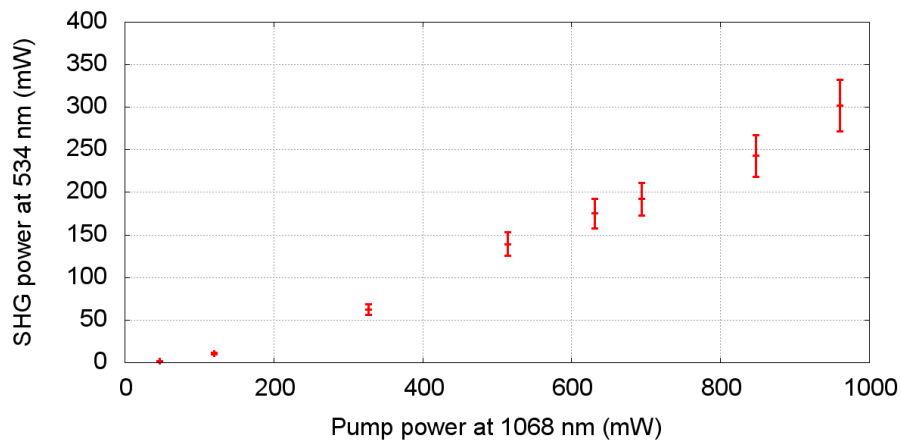


Figure A.3.: Output power of the single-pass waveguide SHG module at 534 nm as function of the pump power. The latter was obtained taking a coupling efficiency of 75% between the output fiber of the amplifier and the input fiber of the SHG module into account.

## A. Appendix

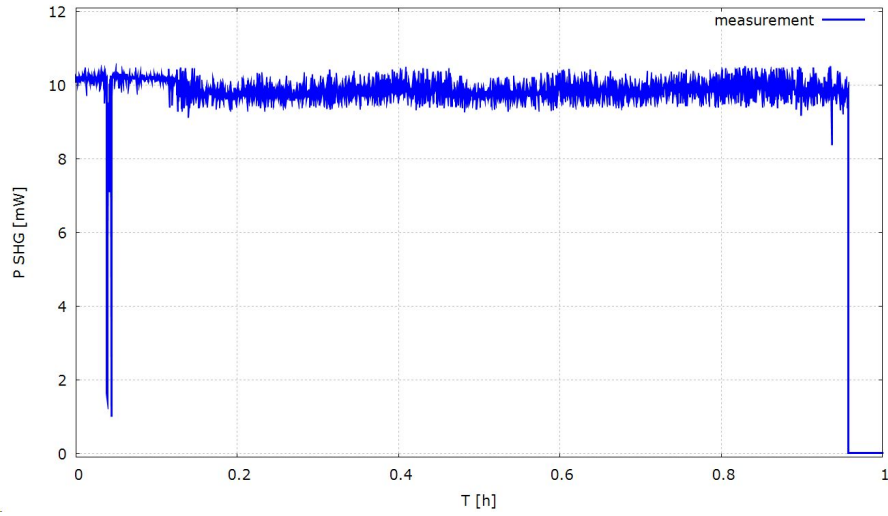


Figure A.4.: 267 nm output power of the second generation SHG cavity versus time for about 300 mW pump power.

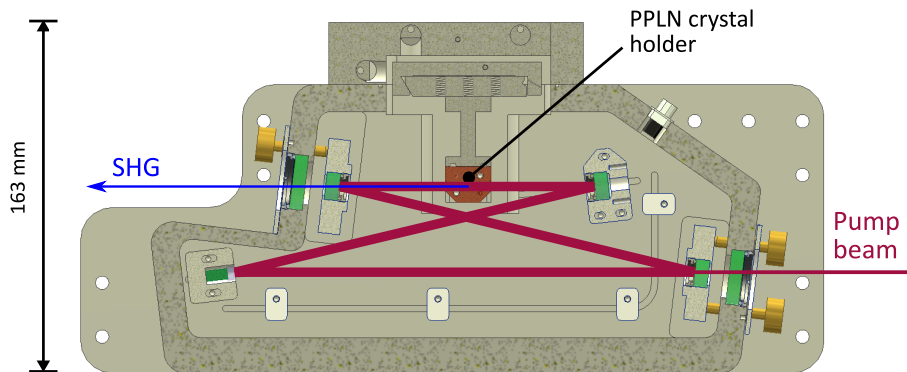


Figure A.5.: Horizontal cross section of the IR to VIS version of the second generation SHG cavity. The cavity is employed for SHG of 882 nm in a 10 mm long PPLN crystal in the highly charged ions experiment at PTB. For 29.5 mW PL coupled into the cavity, an output power of 25.3 mW is achieved, resulting in a doubling efficiency of 85.7%. During the first 100 days after initial alignment the SHG power decreased by 10%, while the entire cavity was left untouched<sup>1</sup>.







# Bibliography

- [Allan, 1966] Allan, D. W. (1966). Statistics of atomic frequency standards. *Proceedings of the IEEE*, 54(2):221–230.
- [Alt, 2002] Alt, W. (2002). An objective lens for efficient fluorescence detection of single atoms. *Optik-International Journal for Light and Electron Optics*, 113(3):142–144.
- [Amairi, 2014] Amairi, S. (2014). *A Long Optical Cavity For Sub-Hertz Laser Spectroscopy*. Phd thesis, Leibniz Universität Hannover.
- [Armstrong et al., 1962] Armstrong, J. A., Bloembergen, N., Ducuing, J., and Pershan, P. S. (1962). Interactions between light waves in a nonlinear dielectric. *Phys. Rev.*, 127:1918–1939.
- [Ashkin et al., 1966] Ashkin, A., Boyd, G., and Dziedzic, J. (1966). Resonant optical second harmonic generation and mixing. *IEEE J. Quant. Electron.*, 2(6):109–124.
- [Ballance et al., 2018] Ballance, T. G., Goodwin, J. F., Nichol, B., Stephenson, L. J., Ballance, C. J., and Lucas, D. M. (2018). A short response time atomic source for trapped ion experiments. *Rev. Sc. Instr.*, 89(5):053102.
- [Barrett et al., 2003] Barrett, M., DeMarco, B., Schaetz, T., Meyer, V., Leibfried, D., Britton, J., Chiaverini, J., Itano, W., Jelenkovic, B., Jost, J., Langer, C., Rosenband, T., and Wineland, D. (2003). Sympathetic cooling of  ${}^9\text{Be}^+$  and  ${}^{24}\text{Mg}^+$  for quantum logic. *Phys. Rev. A*, 68(4):042302.
- [Barton et al., 2000] Barton, P. A., Donald, C. J. S., Lucas, D. M., Stevens, D. A., Steane, A. M., and Stacey, D. N. (2000). Measurement of the lifetime of the  $3d^2d_{5/2}$  state in  ${}^{40}\text{Ca}^+$ . *Phys. Rev. A*, 62(3):032503.

## Bibliography

- [Beev et al., 2017] Beev, N., Fenske, J.-A., Hannig, S., and Schmidt, P. O. (2017). A low-drift, low-noise, multichannel dc voltage source for segmented-electrode paul traps. *Rev. Sc. Instr.*, 88(5):054704.
- [Beloy et al., 2017] Beloy, K., Leibbrandt, D. R., and Itano, W. M. (2017). Hyperfine-mediated electric quadrupole shifts in  $al^+$  and  $in^+$  ion clocks. *Phys. Rev. A*, 95:043405.
- [Berkeland et al., 1998] Berkeland, D. J., Miller, J. D., Bergquist, J. C., Itano, W. M., and Wineland, D. J. (1998). Minimization of ion micromotion in a Paul trap. *J. of Appl. Phys.*, 83(10):5025–5033.
- [Bjerhammar, 1985] Bjerhammar, A. (1985). On a relativistic geodesy. *Bulletin Geodesique*, 59(3):207–220.
- [Bondarescu et al., 2012] Bondarescu, R., Bondarescu, M., Hetenyi, G., Boschi, L., Jetzer, P., and Balakrishna, J. (2012). Geophysical applicability of atomic clocks: direct continental geoid mapping. *Geophysical Journal International*, 191(1):78–82.
- [Borregaard and Sørensen, 2013] Borregaard, J. and Sørensen, A. S. (2013). Efficient Atomic Clocks Operated with Several Atomic Ensembles. *Phys. Rev. Lett.*, 111(9):090802.
- [Boyd and Kleinman, 1968] Boyd, G. D. and Kleinman, D. A. (1968). Parametric interaction of focused gaussian light beams. *J. of Appl. Phys.*, 39(8):3597–3639.
- [Briles et al., 2010] Briles, T. C., Yost, D. C., Cingöz, A., Ye, J., and Schibli, T. R. (2010). Simple piezoelectric-actuated mirror with 180 kHz servo bandwidth. *Opt. Exp.*, 18(10):9739–9746.
- [Brownutt et al., 2015] Brownutt, M., Kumph, M., Rabl, P., and Blatt, R. (2015). Ion-trap measurements of electric-field noise near surfaces. *Reviews of Modern Physics*, 87(4):1419–1482.
- [Bureau International des Poids et Mesures, 2006] Bureau International des Poids et Mesures (2006). SI Brochure: The International System of Units (SI) [8th edition, 2006; updated in 2014]. <http://www.bipm.org/en/publications/si-brochure/second.html>.

- [Cao et al., 2017] Cao, J., Zhang, P., Shang, J., Cui, K., Yuan, J., Chao, S., Wang, S., Shu, H., and Huang, X. (2017). A compact, transportable single-ion optical clock with  $7.8 \times 10^{-17}$  systematic uncertainty. *Appl. Phys. B*, 123(4):112.
- [Carollo et al., 2017] Carollo, R. A., Lane, D. A., Kleiner, E. K., Kyaw, P. A., Teng, C. C., Ou, C. Y., Qiao, S., and Hanneke, D. (2017). Third-harmonic-generation of a diode laser for quantum control of beryllium ions. *Opt. Exp.*, 25(7):7220–7229.
- [Chen et al., 2009] Chen, C. T., Wang, G. L., Wang, X. Y., and Xu, Z. Y. (2009). Deep-uv nonlinear optical crystal kbe2bo3f2—discovery, growth, optical properties and applications. *Appl. Phys. B*, 97(1):9–25.
- [Chen et al., 2017] Chen, J.-S., Brewer, S. M., Chou, C. W., Wineland, D. J., Leibbrandt, D., and Hume, D. B. (2017). Sympathetic Ground State Cooling and Time-Dilation Shifts in an  $^{27}\text{Al}^+$  Optical Clock. *Phys. Rev. Lett.*, 118(5):053002.
- [Chou et al., 2010a] Chou, C. W., Hume, D. B., Koelemeij, J. C. J., Wineland, D. J., and Rosenband, T. (2010a). Frequency comparison of two high-accuracy  $\text{Al}^+$  optical clocks. *Phys. Rev. Lett.*, 104(7):070802.
- [Chou et al., 2010b] Chou, C. W., Hume, D. B., Rosenband, T., and Wineland, D. J. (2010b). Optical Clocks and Relativity. *Science*, 329(5999):1630–1633.
- [Cohen-Tannoudji, 2004] Cohen-Tannoudji, C. (2004). *Atoms In Electromagnetic Fields (2nd Edition)*. World Scientific Series On Atomic, Molecular And Optical Physics. World Scientific Publishing Company.
- [Conference Generale des Poids et Mesures, 1961] Conference Generale des Poids et Mesures (1961). Comptes Rendus de la 11e CGPM (1960). <https://www.bipm.org/en/CGPM/db/11/9/>.
- [Couturier et al., 2018] Couturier, L., Nosske, I., Hu, F., Tan, C., Qiao, C., Jiang, Y. H., Chen, P., and Weidemüller, M. (2018). Laser frequency stabilization using a commercial wavelength meter. *Rev. Sc. Instr.*, 89(4):043103.
- [Cui et al., 2018] Cui, K., Shang, J.-j., Chao, S.-j., Wang, S.-m., Yuan, J.-b., Zhang, P., Cao, J., Shu, H.-l., and Huang, X.-r. (2018). Sympathetic sideband cooling of a  $^{40}\text{Ca}^+ \text{-} ^{27}\text{Al}^+$  pair toward a quantum logic clock. *J. of Phys. B: Atomic, Molecular and Optical Physics*.

## Bibliography

- [Dehmelt, 1968] Dehmelt, H. G. (1968). Radiofrequency Spectroscopy of Stored Ions I: Storage. *Advances in Atomic and Molecular Physics*, 3:53–72.
- [Dehmelt, 1973] Dehmelt, H. G. (1973). Proposed  $10^{-14}\delta\nu/\nu$  laser fluorescence spectroscopy on  $\text{Ti}^+$  mono-ion oscillator. *Bull. Am. Phys. Soc.*, 18:1521.
- [Dolezal et al., 2015] Dolezal, M., Balling, P., Nisbet-Jones, P. B. R., King, S. A., Jones, J. M., Klein, H. A., Gill, P., Lindvall, T., Wallin, A. E., M Merimaa, Tamm, C., Sanner, C., Huntemann, N., Scharnhorst, N., Leroux, I. D., Schmidt, P. O., Burgermeister, T., Mehlstäubler, T. E., and Peik, E. (2015). Analysis of thermal radiation in ion traps for optical frequency standards. *Metrologia*, 52(6):842.
- [Drever et al., 1983] Drever, R. W. P., Hall, J. L., Kowalski, F. V., Hough, J., Ford, G. M., Munley, A. J., and Ward, H. (1983). Laser phase and frequency stabilization using an optical resonator. *Appl. Phys. B.: Lasers and Optics*, 31(2):97–105.
- [Drinkwater et al., 2003] Drinkwater, M. R., Floberghagen, R., Haagmans, R., Muzi, D., and Popescu, A. (2003). *GOCE: ESA's First Earth Explorer Core Mission*, pages 419–432. Springer Netherlands, Dordrecht.
- [Dube et al., 2005] Dube, P., Madej, A., Bernard, J., Marmet, L., Boulanger, J.-S., and Cundy, S. (2005). Electric Quadrupole Shift Cancellation in Single-Ion Optical Frequency Standards. *Phys. Rev. Lett.*, 95(3):033001.
- [Einstein, 1916] Einstein, A. (1916). Die Grundlage der allgemeinen Relativitätstheorie. *Annalen der Physik*, 354(7):769–822.
- [Eismann et al., 2012] Eismann, U., Gerbier, F., Canalias, C., Zukauskas, A., Trenec, G., Vigue, J., Chevy, F., and Salomon, C. (2012). An all-solid-state laser source at 671 nm for cold-atom experiments with lithium. *Appl. Phys. B.*, 106(1):25–36.
- [Essen and Parry, 1955] Essen, L. and Parry, J. V. L. (1955). An atomic standard of frequency and time interval: A caesium resonator. *Nature*, 176:280.
- [European Space Agency, 2018] European Space Agency (2018). GOCE. [https://www.esa.int/Our\\_Activities/Observing\\_the\\_Earth/GOCE](https://www.esa.int/Our_Activities/Observing_the_Earth/GOCE).
- [Fenske, 2015] Fenske, J. (2015). Implementierung eines digitalen PID-Reglers mit dem Entwicklungsboard Red Pitaya. Bachelor's thesis, Ostfalia Hochschule für angewandte Wissenschaften, Germany.

- [Franken et al., 1961] Franken, P. A., Hill, A. E., Peters, C. W., and Weinreich, G. (1961). Generation of optical harmonics. *Phys. Rev. Lett.*, 7:118–119.
- [Franzen, 2009] Franzen, A. (2009). ComponentLibrary, <http://www.gwoptics.org/ComponentLibrary/>. Published according to <http://creativecommons.org/licenses/by-nc/3.0/>.
- [Freearde et al., 1997] Freearde, T., Coutts, J., Walz, J., Leibfried, D., and Hänsch, T. W. (1997). General analysis of type i second-harmonic generation with elliptical gaussian beams. *J. Opt. Soc. Am. B*, 14(8):2010–2016.
- [Fujieda et al., 2018] Fujieda, M., Yang, S. H., Gotoh, T., Hwang, S. W., Hachisu, H., Kim, H., Lee, Y. K., Tabuchi, R., Ido, T., Lee, W. K., Heo, M. S., Park, C. Y., Yu, D. H., and Petit, G. (2018). Advanced Satellite-based Frequency Transfer at the  $10^{-16}$  Level. *IEEE Transactions on Ultrasonics, Ferroelectrics, and Frequency Control*, 65(6):973–978.
- [Ghosh, 1995] Ghosh, P. (1995). *Ion Traps*. International Series of Monographs on Physics. Clarendon Press.
- [Gill, 2011] Gill, P. (2011). When should we change the definition of the second? *Philosophical Transactions of the Royal Society A: Mathematical, Physical and Engineering Sciences*, 369(1953):4109–4130.
- [Godun et al., 2014] Godun, R. M., Nisbet-Jones, P. B. R., Jones, J. M., King, S. A., Johnson, L. A. M., Margolis, H. S., Szymaniec, K., Lea, S. N., Bongs, K., and Gill, P. (2014). Frequency Ratio of Two Optical Clock Transitions in Yb+171 and Constraints on the Time Variation of Fundamental Constants. *Phys. Rev. Lett.*, 113(21):210801.
- [Goldovsky et al., 2016] Goldovsky, D., Jouravsky, V., and Peer, A. (2016). Simple and robust phase-locking of optical cavities with  $> 200$  KHz servo-bandwidth using a piezo-actuated mirror mounted in soft materials. *Opt. Exp.*, 24(25):28239–28246.
- [Gouy, 1890] Gouy, L. G. (1890). Sur une propriete nouvelle des ondes lumineuses. *C. R. Acad. Sci.*, 110:1251.
- [Grotti et al., 2018] Grotti, J., Koller, S., Vogt, S., Häfner, S., Sterr, U., Lisdat, C., Denker, H., Voigt, C., Timmen, L., Rolland, A., Baynes, F., Margolis, H.,

## Bibliography

- Zampaolo, M., Thoumany, P., Pizzocaro, M., Rauf, B., Bregolin, F., Tampellini, A., Barbieri, P., Zucco, M., Costanzo, G., Clivati, C., Levi, F., and Calonico, D. (2018). Geodesy and metrology with a transportable optical clock. *Nat. Phys.*
- [Guena et al., 2017] Guena, J., Weyers, S., Abgrall, M., Grebing, C., Gerginov, V., Rosenbusch, P., Bize, S., Lipphardt, B., Denker, H., Quintin, N., Raupach, S. M. F., Nicolodi, D., Stefani, F., Chiodo, N., Koke, S., Kuhl, A., Wiotte, F., Meynadier, F., Camisard, E., C Chardonnet, Coq, Y. L., Lours, M., Santarelli, G., Amy-Klein, A., Targat, R. L., Lopez, O., Pottie, P. E., and Grosche, G. (2017). First international comparison of fountain primary frequency standards via a long distance optical fiber link. *Metrologia*, 54(3):348.
- [Guggemos, 2016] Guggemos, M. (2016). *Precision spectroscopy with trapped  $40\text{Ca}^+$  and  $27\text{Al}^+$  ions*. Phd thesis, University of Innsbruck, Innsbruck, Austria.
- [Guggemos et al., 2015] Guggemos, M., Heinrich, D., Herrera-Sancho, O. A., Blatt, R., and Roos, C. F. (2015). Sympathetic cooling and detection of a hot trapped ion by a cold one. *New J. of Phy.*, 17(10):103001.
- [Häfner et al., 2015] Häfner, S., Falke, S., Grebing, C., Vogt, S., Legero, T., Merimaa, M., Lisdat, C., and Sterr, U. (2015).  $8 \times 10^{-17}$  fractional laser frequency instability with a long room-temperature cavity. *Opt. Lett.*, 40(9):2112.
- [Hall, 2006] Hall, J. (2006). Nobel Lecture: Defining and measuring optical frequencies. *Rev. Mod. Phys.*, 78(4):1279–1295.
- [Hannig et al., 2018a] Hannig, S., Mielke, J., Fenske, J.-A., Misera, M., Beev, N., Ospelkaus, C., and Schmidt, P. O. (2018a). A highly stable monolithic enhancement cavity for second harmonic generation in the ultraviolet. *Rev. Sc. Instr.*, 89(1):013106.
- [Hannig et al., 2018b] Hannig, S., Pelzer, L., Scharnhorst, N., Kramer, J., Stepanova, M., Xu, Z., Spethmann, N., Leroux, I. D., and Schmidt, P. O. (2018b). Towards a transportable aluminum ion quantum logic optical clock. In preparation.
- [Hänsch, 2006] Hänsch, T. (2006). Nobel Lecture: Passion for precision. *Rev. Mod. Phys.*, 78(4):1297–1309.

- [Hänsch and Couillaud, 1980] Hänsch, T. W. and Couillaud, B. (1980). Laser frequency stabilization by polarization spectroscopy of a reflecting reference cavity. *Opt. Commun.*, 35(3):441–444.
- [Hänsch and Schawlow, 1975] Hänsch, T. W. and Schawlow, A. L. (1975). Cooling of gases by laser radiation. *Opt. Commun.*, 13(1):68–69.
- [Hecht, 2001] Hecht, E. (2001). *Optik*. Oldenbourg.
- [Hemmerich et al., 1994] Hemmerich, A., Zimmermann, C., and Hänsch, T. W. (1994). Compact source of coherent blue light. *Appl. Opt.*, 33(6):988–991.
- [Hemmerling et al., 2012] Hemmerling, B., Gebert, F., Wan, Y., and Schmidt, P. O. (2012). A novel, robust quantum detection scheme. *New Journal of Physics*, 14(2):023043.
- [Hendricks et al., 2007] Hendricks, R., Grant, D., Herskind, P., Dantan, A., and Drewsen, M. (2007). An all-optical ion-loading technique for scalable microtrap architectures. *Appl. Phys. B*, 88(4):507–513.
- [Herschbach et al., 2012] Herschbach, N., Pyka, K., Keller, J., and Mehlstäubler, T. E. (2012). Linear Paul trap design for an optical clock with Coulomb crystals. *Appl. Phys. B*, 107(4):891–906.
- [Hu et al., 2013] Hu, J., Zhang, L., Liu, H., Liu, K., Xu, Z., and Feng, Y. (2013). High power room temperature 1014.8 nm Yb fiber amplifier and frequency quadrupling to 253.7 nm for laser cooling of mercury atoms. *Opt. Exp.*, 21(25):30958–30963.
- [Huntemann et al., 2014] Huntemann, N., Lipphardt, B., Tamm, C., Gerginov, V., Weyers, S., and Peik, E. (2014). Improved Limit on a Temporal Variation of  $m_p/m_e$  from Comparisons of Yb<sup>+</sup> and Cs Atomic Clocks. *Phys. Rev. Lett.*, 113(21):210802.
- [Huntemann et al., 2016] Huntemann, N., Sanner, C., Lipphardt, B., Tamm, C., and Peik, E. (2016). Single-Ion Atomic Clock with  $3 \times 10^{-18}$  Systematic Uncertainty. *Phys. Rev. Lett.*, 116(6):063001.
- [Idel, 2016] Idel, A. (2016). Ein kompaktes Lasersystem zum sympathetischen Kühlen einzelner (Anti-) Protonen durch <sup>9</sup>Be<sup>+</sup> Ionen. Master’s thesis, Leibniz Universität Hannover, Germany.

## Bibliography

- [Itano et al., 1993] Itano, W. M., Bergquist, J. C., Bollinger, J. J., Gilligan, J. M., Heinzen, D. J., Moore, F. L., Raizen, M. G., and Wineland, D. J. (1993). Quantum projection noise: Population fluctuations in two-level systems. *Phys. Rev. A*, 47(5):3554–3570.
- [J. Dick, 1987] J. Dick, G. (1987). Local oscillator induced instabilities in trapped ion frequency standards. *Proc. of Precise Time and Time Interval, Redondo Beach*, pages 133–147.
- [Jitschin and Meisel, 1979] Jitschin, W. and Meisel, G. (1979). Fast frequency control of a cw dye jet laser. *Appl. phys.*, 19(2):181–184.
- [Jurdik et al., 2002] Jurdik, E., Hohlfeld, J., van Etteger, A. F., Toonen, A. J., Meerts, W. L., van Kempen, H., and Rasing, T. (2002). Performance optimization of an external enhancement resonator for optical second-harmonic generation. *JOSA B B*, 19(7):1660–1667.
- [Kane and Byer, 1985] Kane, T. J. and Byer, R. L. (1985). Monolithic, unidirectional single-mode Nd:YAG ring laser. *Opt. Lett.*, 10(2):65–67.
- [Kato, 1986] Kato, K. (1986). Second-harmonic generation to 2048 Å in  $\beta$ -BaB<sub>2</sub>O<sub>4</sub>. *IEEE J. Quant. Electron.*, 22(7):1013–1014.
- [Keller, 2015] Keller, J. (2015). *Spectroscopic characterization of ion motion for an optical clock based on Coulomb crystals*. PhD Thesis, Leibniz Universität Hannover, Hannover.
- [Keller et al., 2015] Keller, J., Partner, H. L., Burgermeister, T., and Mehlstäubler, T. E. (2015). Precise determination of micromotion for trapped-ion optical clocks. *J. of Appl. Phys.*, 118(10):104501.
- [Keselman et al., 2011] Keselman, A., Glickman, Y., Akerman, N., Kotler, S., and Ozeri, R. (2011). High-fidelity state detection and tomography of a single-ion Zeeman qubit. *New Journal of Physics*, 13(7):073027.
- [Kessler et al., 2012] Kessler, T., Hagemann, C., Grebing, C., Legero, T., Sterr, U., Riehle, F., Martin, M. J., Chen, L., and Ye, J. (2012). A sub-40-mHz-linewidth laser based on a silicon single-crystal optical cavity. *Nat. Phot.*, 6:687–692.



- [Kleinman, 1962] Kleinman, D. A. (1962). Nonlinear dielectric polarization in optical media. *Phys. Rev.*, 126:1977–1979.
- [Knoop et al., 2015] Knoop, M., Marzoli, I., and Morigi, G. (2015). *Ion Traps for Tomorrow's Applications*. EBL-Schweitzer. IOS Press.
- [Kobtsev et al., 2007] Kobtsev, S., Kandrushin, S., and Potekhin, A. (2007). Long-term frequency stabilization of a continuous-wave tunable laser with the help of a precision wavelengthmeter. *Appl. Opt.*, 46(23):5840–5843.
- [Koller et al., 2017] Koller, S. B., Grotti, J., Vogt, S., Al-Masoudi, A., Dörscher, S., Häfner, S., Sterr, U., and Lisdat, C. (2017). Transportable optical lattice clock with  $7 \times 10^{-17}$  uncertainty. *Phys. Rev. Lett.*, 118(7):073601.
- [Kozlovsky et al., 1994] Kozlovsky, W. J., Risk, W. P., Lenth, W., Kim, B. G., Bona, G. L., Jaekel, H., and Webb, D. J. (1994). Blue light generation by resonator-enhanced frequency doubling of an extended-cavity diode laser. *Appl. Phys. Lett.*, 65(5):525.
- [Kramida et al., 2018] Kramida, A., Ralchenko, Y., Reader, J., and NIST ASD Team (2018). NIST Atomic Spectra Database (version 5.5.6). [Online]. Available: <https://physics.nist.gov/asd> [Wed Apr 11 2018]. National Institute of Standards and Technology, Gaithersburg, MD.
- [Lamb, 1884] Lamb, H. (1884). Xiii. on electrical motions in a spherical conductor. *Philosophical Transactions of the Royal Society of London*, 174:519–549.
- [Larson et al., 1986] Larson, D. J., Bergquist, J. C., Bollinger, J. J., Itano, W. M., and Wineland, D. J. (1986). Sympathetic cooling of trapped ions: A laser-cooled two-species nonneutral ion plasma. *Phys. Rev. Lett.*, 57(1):70.
- [Lee et al., 2017] Lee, W.-K., Stefani, F., Bercy, A., Lopez, O., Amy-Klein, A., and Pottie, P.-E. (2017). Hybrid fiber links for accurate optical frequency comparison. *Appl. Phys. B*, 123(5):161.
- [Lisdat et al., 2016] Lisdat, C., Grosche, G., Quintin, N., Shi, C., Raupach, S. M. F., Grebing, C., Nicolodi, D., Stefani, F., Al-Masoudi, A., Dörscher, S., Häfner, S., Robyr, J.-L., Chiodo, N., Bilicki, S., Bookjans, E., Koczwar, A., Koke, S., Kuhl, A., Wiotte, F., Meynadier, F., Camisard, E., Abgrall, M., Lours, M., Legero, T.,

## Bibliography

- Schnatz, H., Sterr, U., Denker, H., Chardonnet, C., Le Coq, Y., Santarelli, G., Amy-Klein, A., Le Targat, R., Lodewyck, J., Lopez, O., and Pottie, P.-E. (2016). A clock network for geodesy and fundamental science. *Nat. Commun.*, 7:12443.
- [Ludlow et al., 2015] Ludlow, A. D., Boyd, M. M., Ye, J., Peik, E., and Schmidt, P. (2015). Optical atomic clocks. *Rev. Mod. Phys.*, 87(2):637–701.
- [Macalpine and Schildknecht, 1959] Macalpine, W. W. and Schildknecht, R. O. (1959). Coaxial resonators with helical inner conductor. *Proceedings of the IRE*, 47(12):2099–2105.
- [Mahajan, 1983] Mahajan, V. N. (1983). Strehl ratio for primary aberrations in terms of their aberration variance. *J. Opt. Soc. Am.*, 73(6):860–861.
- [Major et al., 2005] Major, F., Gheorghe, V., and Werth, G. (2005). *Charged Particle Traps: Physics and Techniques of Charged Particle Field Confinement*. Charged Particle Traps. Springer.
- [Märk and Dunn, 2013] Märk, T. and Dunn, G. (2013). *Electron Impact Ionization*. Springer Vienna.
- [Mehlstäubler et al., 2018] Mehlstäubler, T. E., Grosche, G., Lisdat, C., Schmidt, P. O., and Denker, H. (2018). Atomic clocks for geodesy. *Reports on Progress in Physics*, 81(6):064401.
- [Monroe et al., 1995] Monroe, C., Meekhof, D. M., King, B. E., Jefferts, S. R., Itano, W. M., Wineland, D. J., and Gould, P. (1995). Resolved-sideband Raman cooling of a bound atom to the 3d zero-point energy. *Phys. Rev. Lett.*, 75(22):4011–4014.
- [Morigi et al., 2000] Morigi, G., Eschner, J., and Keitel, C. H. (2000). Ground state laser cooling using electromagnetically induced transparency. *Phys. Rev. Lett.*, 85(21):4458–4461.
- [Müller et al., 2018] Müller, J., Dirkx, D., Kopeikin, S. M., Lion, G., Panet, I., Petit, G., and Visser, P. N. a. M. (2018). High Performance Clocks and Gravity Field Determination. *Space Science Reviews*, 214(1):5.
- [National Aeronautics and Space Administration, 2018] National Aeronautics and Space Administration (2018). GRACE. [https://www.nasa.gov/mission\\_pages/Grace/index.html](https://www.nasa.gov/mission_pages/Grace/index.html).

- [Neumann and Meyer, 1885] Neumann, F. and Meyer, O. (1885). *Vorlesungen über die Theorie der Elasticität der festen Körper und des Lichtäthers: gehalten an der Universität Königsberg*. Number Bd. 5 in Franz Neumann. B. G. Teubner.
- [Nicholson et al., 2015] Nicholson, T. L., Campbell, S. L., Hutson, R. B., Marti, G. E., Bloom, B. J., McNally, R. L., Zhang, W., Barrett, M. D., Safronova, M. S., Strouse, G. F., Tew, W. L., and Ye, J. (2015). Systematic evaluation of an atomic clock at  $2 \times 10^{-18}$  total uncertainty. *Nat. Comm.*, 6:6896.
- [Nikogosyan, 2005] Nikogosyan, D. N. (2005). *Nonlinear Optical Crystals: A Complete Survey*. Springer.
- [NTT Electronics Corporation, 2017] NTT Electronics Corporation (2017). Wavelength Conversion Module. <http://www.ntt-electronics.com/en/products/photonics/conversion-module.html>.
- [Paul, 1990] Paul, W. (1990). Electromagnetic traps for charged and neutral particles. *Rev. Mod. Phys.*, 62:531–540.
- [Paul et al., 1958] Paul, W., Osberghaus, O., and Fischer, E. (1958). Ein Ionenkäfig. *Forschungsberichte Wirtschafts- und Verkehrsministerium Nordrhein-Westfalen, Westdeutscher Verlag, Köln und Opladen*.
- [Pham, 2005] Pham, P. T. T. (2005). *A general-purpose pulse sequencer for quantum computing*. PhD Thesis, Massachusetts Institute of Technology, Cambridge, Massachusetts, USA.
- [Picken et al., 2017] Picken, C. J., Legaie, R., and Pritchard, J. D. (2017). Single atom imaging with an sCMOS camera. *Appl. Phys. Lett.*, 111(16):164102.
- [Polzik and Kimble, 1991] Polzik, E. S. and Kimble, H. J. (1991). Frequency doubling with  $\text{KNbO}_3$  in an external cavity. *Opt. Lett.*, 16(18):1400–1402.
- [PTB Working Group 1.71, 2017] PTB Working Group 1.71 (2017). Multi-component acceleration exciter. <https://www.ptb.de/cms/en/ptb/fachabteilungen/abt1/fb-17/ag-171/research-and-development-01/multi-component-acceleration-exciter.html>.
- [Pyka et al., 2014] Pyka, K., Herschbach, N., Keller, J., and Mehlstäubler, T. E. (2014). A high-precision segmented Paul trap with minimized micromotion for an optical multiple-ion clock. *Appl. Phys. B*, 114(1-2):231–241.

## Bibliography

- [Ramm et al., 2013] Ramm, M., Pruttivarasin, T., Kokish, M., Talukdar, I., and Häffner, H. (2013). Precision Measurement Method for Branching Fractions of Excited  $P_{1/2}$  States Applied to  $^{40}\text{Ca}^+$ . *Phys. Rev. Lett.*, 111(2):023004.
- [Raupach et al., 2015] Raupach, S. M. F., Koczwara, A., and Grosche, G. (2015). Brillouin amplification supports  $1 \times 10^{-20}$  uncertainty in optical frequency transfer over 1400 km of underground fiber. *Phys. Rev. A*, 92(2):021801.
- [Reigber et al., 2005] Reigber, C., Schmidt, R., Flechtner, F., König, R., Meyer, U., Neumayer, K.-H., Schwintzer, P., and Zhu, S. Y. (2005). An earth gravity field model complete to degree and order 150 from grace: Eigen-grace02s. *Journal of Geodynamics*, 39(1):1 – 10.
- [Riehle, 2004] Riehle, F. (2004). *Frequency standards: basics and applications*. Wiley-VCH, Weinheim.
- [Riehle, 2015] Riehle, F. (2015). Towards a redefinition of the second based on optical atomic clocks. *Comptes Rendus Physique*, 16(5):506–515.
- [Riehle, 2017] Riehle, F. (2017). Optical clock networks. *Nature Photonics*, 11(1):25–31.
- [Roos et al., 1999] Roos, C., Zeiger, T., Rohde, H., Nägerl, H. C., Eschner, J., Leibfried, D., Schmidt-Kaler, F., and Blatt, R. (1999). Quantum state engineering on an optical transition and decoherence in a paul trap. *Phys. Rev. Lett.*, 83(23):4713–4716.
- [Roos et al., 2000] Roos, C. F., Leibfried, D., Mundt, A., Schmidt-Kaler, F., Eschner, J., and Blatt, R. (2000). Experimental demonstration of ground state laser cooling with electromagnetically induced transparency. *Phys. Rev. Lett.*, 85(26):5547–5550.
- [Rosenband et al., 2008] Rosenband, T., Hume, D. B., Schmidt, P. O., Chou, C. W., Brusch, A., Lorini, L., Oskay, W. H., Drullinger, R. E., Fortier, T. M., Stalnaker, J. E., Diddams, S. A., Swann, W. C., Newbury, N. R., Itano, W. M., Wineland, D. J., and Bergquist, J. C. (2008). Frequency ratio of  $\text{Al}^+$  and  $\text{Hg}^+$  Single-Ion Optical Clocks; Metrology at the 17<sup>th</sup> Decimal Place. *Science*, 319(5871):1808–1812.

- [Rosenband et al., 2006] Rosenband, T., Itano, W. M., Schmidt, P. O., Hume, D. B., Koelemeij, J. C. J., Bergquist, J. C., and Wineland, D. J. (2006). Blackbody radiation shift of the  $^{27}\text{Al}^+ \ ^1\text{S}_0 - \ ^3\text{P}_0$  transition. In *Proceedings of the 20th European Frequency and Time Forum*, pages 289–291, Braunschweig, Germany.
- [Rosenband and Leibbrandt, 2013] Rosenband, T. and Leibbrandt, D. R. (2013). Exponential scaling of clock stability with atom number. *arXiv:1303.6357*.
- [Rosenband et al., 2007] Rosenband, T., Schmidt, P. O., Hume, D. B., Itano, W. M., Fortier, T. M., Stalnaker, J. E., Kim, K., Diddams, S. A., Koelemeij, J. C. J., Bergquist, J. C., and Wineland, D. J. (2007). Observation of the  $^1\text{S}_0 \rightarrow \ ^3\text{P}_0$  Clock Transition in  $^{27}\text{Al}^+$ . *Phys. Rev. Lett.*, 98(22):220801.
- [Safronova et al., 2018] Safronova, M. S., Budker, D., DeMille, D., Kimball, D. F. J., Derevianko, A., and Clark, C. W. (2018). Search for new physics with atoms and molecules. *Rev. Mod. Phys.*, 90:025008.
- [Safronova et al., 2011] Safronova, M. S., Kozlov, M. G., and Clark, C. W. (2011). Precision Calculation of Blackbody Radiation Shifts for Optical Frequency Metrology. *Phys. Rev. Lett.*, 107(14):143006.
- [Saleh et al., 2015] Saleh, K., Millo, J., Didier, A., Kersale, Y., and Lacroute, C. (2015). Frequency stability of a wavelength meter and applications to laser frequency stabilization. *Appl. Opt.*, 54(32):9446–9449.
- [Sandberg, 1993] Sandberg, J. C. (1993). *Research Towards Laser Spectroscopy of Trapped Atomic Hydrogen*. Phd thesis, MIT.
- [Scharnhorst, 2018] Scharnhorst, N. (2018). *Multi-mode ground state cooling of trapped ions*. PhD Thesis, Leibniz Universität Hannover.
- [Scharnhorst et al., 2017] Scharnhorst, N., Cerrillo, J., Kramer, J., Leroux, I. D., Wübbena, J. B., Retzker, A., and Schmidt, P. O. (2017). Experimental and theoretical aspects of double-bright EIT cooling. *arXiv:1711.00732 [physics, physics:quant-ph]*. arXiv: 1711.00732.
- [Scharnhorst et al., 2015] Scharnhorst, N., Wübbena, J. B., Hannig, S., Jakobsen, K., Kramer, J., Leroux, I. D., and Schmidt, P. O. (2015). High-bandwidth transfer of phase stability through a fiber frequency comb. *Opt. Exp.*, 23(15):19771–19776.

## Bibliography

- [Scheid et al., 2007] Scheid, M., Markert, F., Walz, J., Wang, J., Kirchner, M., and Hänsch, T. W. (2007). 750 mw continuous-wave solid-state deep ultraviolet laser source at the 253.7 nm transition in mercury. *Opt. Lett.*, 32(8):955–957.
- [Schindler, 2008] Schindler, P. (2008). *Frequency synthesis and pulse shaping for quantum information processing with trapped ions*. PhD Thesis, University of Innsbruck, Innsbruck, Austria.
- [Schioppo et al., 2017] Schioppo, M., Brown, R. C., McGrew, W. F., Hinkley, N., Fasano, R. J., Beloy, K., Yoon, T. H., Milani, G., Nicolodi, D., Sherman, J. A., Phillips, N. B., Oates, C. W., and Ludlow, A. D. (2017). Ultrastable optical clock with two cold-atom ensembles. *Nat Photon*, 11(1):48–52.
- [Schmidt et al., 2005] Schmidt, P. O., Rosenband, T., Langer, C., Itano, W. M., Bergquist, J. C., and Wineland, D. J. (2005). Spectroscopy using quantum logic. *Science*, 309(5735):749–752.
- [Schmidt-Kaler et al., 2001] Schmidt-Kaler, F., Eschner, J., Morigi, G., Roos, C., Leibfried, D., Mundt, A., and Blatt, R. (2001). Laser cooling with electromagnetically induced transparency: application to trapped samples of ions or neutral atoms. *Appl. Phys. B: Lasers and Optics*, 73(8):807–814.
- [Schulte et al., 2016] Schulte, M., Lörch, N., Leroux, I., Schmidt, P. O., and Hammerer, K. (2016). Quantum Algorithmic Readout in Multi-Ion Clocks. *Phys. Rev. Lett.*, 116(1):013002.
- [Sellmeier, 1871] Sellmeier (1871). Zur Erklärung der abnormen Farbenfolge im Spectrum einiger Substanzen. *Annalen der Physik*, 219(6):272–282.
- [Sherstov et al., 2010] Sherstov, I., Okhapkin, M., Lipphardt, B., Tamm, C., and Peik, E. (2010). Diode-laser system for high-resolution spectroscopy of the  $^2s_{1/2} \rightarrow ^2f_{7/2}$  octupole transition in  $^{171}\text{Yb}^+$ . *Phys.Rev.A*, 81(2) : 021805.
- [Siverns et al., 2011] Siverns, J. D., Simkins, L. R., Weidt, S., and Hensinger, W. K. (2011). On the application of radio frequency voltages to ion traps via helical resonators. *arXiv:1106.5013*.
- [Skoczowsky et al., 2010] Skoczowsky, D., Jechow, A., Menzel, R., Paschke, K., and Erbert, G. (2010). Efficient second-harmonic generation using a semiconductor tapered amplifier in a coupled ring-resonator geometry. *Opt. Lett.*, 35(2):232–234.

- [Smith, 2000] Smith, W. (2000). *Modern Optical Engineering: The Design of Optical Systems*. McGraw-Hill series on optical and electro-optical engineering. McGraw Hill.
- [Stepanova, 2017] Stepanova, M. (2017). Setup of a logic laser for  $\text{Ca}^+$ . Master's thesis, Leibniz Universität Hannover, Germany.
- [Terrien, 1968] Terrien, J. (1968). News from the international bureau of weights and measures. *Metrologia*, 4(1):41.
- [Thorlabs Inc., 2017] Thorlabs Inc. (2017). Co-Fired Piezoelectric Actuator datasheet <https://www.thorlabs.de>.
- [Toptica Photonics AG, 2018] Toptica Photonics AG (2018). DL Pro. <https://www.toptica.com/products/tunable-diode-lasers/ecdl-dfb-lasers/dl-pro/>.
- [Ushijima et al., 2015] Ushijima, I., Takamoto, M., Das, M., Ohkubo, T., and Katori, H. (2015). Cryogenic optical lattice clocks. *Nat. Phot.*, 9:185–189.
- [Vasilyev et al., 2011] Vasilyev, S., Nevsky, A., Ernsting, I., Hansen, M., Shen, J., and Schiller, S. (2011). Compact all-solid-state continuous-wave single-frequency UV source with frequency stabilization for laser cooling of  $\text{Be}^+$  ions. *Appl. Phys. B.*, 103(1):27–33.
- [Vermeer, 1983] Vermeer, M. (1983). Chronometric levelling. Reports of the Finnish Geodetic Institute 83(2), Geodeettinen Laitos, Geodetiska Institutet.
- [Vutha et al., 2017] Vutha, A. C., Kirchner, T., and Dube, P. (2017). Collisional frequency shift of a trapped-ion optical clock. *Phys. Rev. A*, 96(2):022704.
- [Wakui et al., 2014] Wakui, K., Hayasaka, K., and Ido, T. (2014). Generation of vacuum ultraviolet radiation by intracavity high-harmonic generation toward state detection of single trapped ions. *Appl. Phys. B.*, 117(3):957–967.
- [Wan et al., 2014] Wan, Y., Gebert, F., Wübbena, J. B., Scharnhorst, N., Amairi, S., Leroux, I. D., Hemmerling, B., Lörch, N., Hammerer, K., and Schmidt, P. O. (2014). Precision spectroscopy by photon-recoil signal amplification. *Nat. Commun.*, 5:4096.
- [Watanabe et al., 1991] Watanabe, M., Hayasaka, K., Imajo, H., Umezu, J., and Urabe, S. (1991). Generation of continuous-wave coherent radiation tunable down to 190.8 nm in  $\beta\text{-BaB}_2\text{O}_4$ . *Appl. Phys. B.*, 55:11–13.

## Bibliography

- [Wen et al., 2014] Wen, X., Han, Y., Bai, J., He, J., Wang, Y., Yang, B., and Wang, J. (2014). Cavity-enhanced frequency doubling from 795nm to 397.5nm ultra-violet coherent radiation with PPKTP crystals in the low pump power regime. *Opt. Exp.*, 22(26):32293–32300.
- [Wilson et al., 2011] Wilson, A. C., Ospelkaus, C., VanDevender, A. P., Mlynek, J. A., Brown, K. R., Leibfried, D., and Wineland, D. J. (2011). A 750-mW, continuous-wave, solid-state laser source at 313 nm for cooling and manipulating trapped  ${}^9\text{Be}^+$  ions. *Appl. Phys. B.*, 105:741–748.
- [Wineland and Dehmelt, 1975] Wineland, D. and Dehmelt, H. (1975). Proposed  $10^{-14}\delta\nu/\nu$  laser fluorescence spectroscopy on Tl<sup>+</sup> mono-ion oscillator III (side band cooling). *Bull. Am. Phys. Soc.*, 20:637.
- [Wineland et al., 1992] Wineland, D. J., Bollinger, J. J., Itano, W. M., Moore, F. L., and Heinzen, D. J. (1992). Spin squeezing and reduced quantum noise in spectroscopy. *Physical Review A*, 46(11):R6797–6800.
- [Wineland et al., 1978] Wineland, D. J., Drullinger, R. E., and Walls, F. L. (1978). Radiation-pressure cooling of bound resonant absorbers. *Phys. Rev. Lett.*, 40(25):1639–1642.
- [Wineland and Itano, 1979] Wineland, D. J. and Itano, W. M. (1979). Laser cooling of atoms. *Phys. Rev. A*, 20(4):1521.
- [Wineland et al., 1998] Wineland, D. J., Monroe, C., Itano, W. M., Leibfried, D., King, B. E., and Meekhof, D. M. (1998). Experimental issues in coherent quantum-state manipulation of trapped atomic ions. *Journal of Research of the National Institute of Standards and Technology*, 103(3):259–328.
- [Wübbena, 2014] Wübbena, J. B. (2014). *Controlling Motion in Quantum Logic Clocks*. PhD Thesis, Leibniz Universität Hannover.
- [Wübbena et al., 2012] Wübbena, J. B., Amairi, S., Mandel, O., and Schmidt, P. O. (2012). Sympathetic cooling of mixed-species two-ion crystals for precision spectroscopy. *Phys. Rev. A*, 85(4):043412.
- [Zimmermann et al., 1990] Zimmermann, C., Kallenbach, R., and Hänsch, T. W. (1990). High-resolution spectroscopy of the hydrogen 1s-2s transition in an atomic beam. *Phys. Rev. Lett.*, 65:571–574.







# List of publications

- **S. Hannig**, L. Pelzer, N. Scharnhorst, J. Kramer, M. Stepanova, N. Spethmann, T. E. Mehlstäubler, and P. O. Schmidt: Towards a transportable Al optical ion clock. In preparation.
- L. Klaus, **S. Hannig**, H. Bothe: Vibration Testing to Assess the Transport Behaviour of Reference Standards and Mobile Scientific Devices, accepted as conference paper for XXII IMEKO World Congress (2018)
- **S. Hannig**, J. Mielke, J. A. Fenske, M. Misera, N. Beev, C. Ospelkaus, and P. O. Schmidt: A highly stable monolithic enhancement cavity for second harmonic generation in the ultra violet. *Review of Scientific Instruments*, 89(1):013106, January 2018. doi:10.1063/1.5005515.
- N. Beev, J. A. Fenske, **S. Hannig**, and P. O. Schmidt: A low-drift, low-noise, multichannel dc voltage source for segmented-electrode Paul traps. *Review of Scientific Instruments* 88, 054704 (2017)
- I. Leroux, N. Scharnhorst, **S. Hannig**, J. Kramer, L. Pelzer, M. Stepanova, and P. O. Schmidt: On-line estimation of local oscillator noise and optimisation of servo parameters in atomic clocks. *Metrologia*, Vol. 54, No. 3 (2017)
- N. Scharnhorst, J. B. Wübbena, **S. Hannig**, K. Jakobsen, J. Kramer, I. D. Leroux, and P. O. Schmidt. High-bandwidth transfer of phase stability through a fiber frequency comb. *Optics Express*, Vol. 23, Issue 15, pp. 19771-19776 (2015)



# Curriculum vitae

## PERSONAL DETAILS

Name	Stephan Hannig
Date of birth	23.12.1988
Place of birth	Minden, Germany

## POSTGRADUATE STUDIES

Since 2013	Doctoral studies at the QUEST Institute for Experimental Quantum Metrology, PTB and Leibniz Universität Hannover, Braunschweig, Germany
2013	Master of Science from Technische Universität Dortmund, Germany
2011-2013	Master student of physics at Technische Universität Dortmund, Germany

## UNDERGRADUATE STUDIES

2011	Bachelor of Science from Georg-August-Universität, Göttingen, Germany
2008-2011	Bachelor student of physics at Georg-August-Universität, Göttingen, Germany

## FORMAL EDUCATION

2008	Abitur from Städtisches Gymnasium Porta Westfalica, Germany
1999-2008	Städtisches Gymnasium Porta Westfalica, Germany



# Acknowledgements / Danksagung

Zuerst danke ich Piet Schmidt dafür, dass er mich trotz fehlender Erfahrung im Umgang mit gefangenen Ionen in sein Institut aufgenommen hat und mir so die Promotion ermöglicht hat. Zudem war seine langjährige Expertise an vielen Stellen Gold wert. Ich bedanke mich bei Christian Ospelkaus zum Einen als Koreferenten meiner Doktorarbeit und zum Anderen für die hervorragende Zusammenarbeit bei der Entwicklung hochstabiler Resonatoren zur optischen Frequenzverdopplung.

Insbesondere in meiner Anfangszeit bei QUEST haben mir meine erfahrenen Kollegen Jannes Wübbena und Nils Scharnhorst eine Fülle von experimentellen Grundlagen vermittelt und somit den späteren Aufbau von IQLOC2 ermöglicht. Ausdrücklich danke ich auch für die vielen gemeinsamen Freizeit-Experimente zur Untersuchung des Flugverhaltens von Discgolf-Scheiben und Gleitschirmen. Lennart Pelzer war bei den Charakterisierungsmessungen von IQLOC2 eine große Unterstützung und konnte zudem als ernstzunehmender Squash-Trainingspartner Akzente setzen. Ich danke ausdrücklich Tanja Mehlstäubler und ihrer Gruppe dafür, dass ich auf ihre Fallentechnologie zurückgreifen konnte. Weitere Unterstützungsbeiträge beim Aufbau von IQLOC2 wurden von Johannes Kramer, Kornelius Jakobsen, Mariia Stepanova, Nicolas Spethmann und Kai Dietze geleistet. Besonderer Dank gilt Ian Leroux und Steven King, die mich an ihrem Erfahrungsschatz teilhaben ließen und mir viele Fragen geduldig beantworteten.

Ein großes Projekt war die Entwicklung von optischen Frequenzverdopplungscavities. Ich danke Johannes Mielke für seinen professionellen und zielgerichteten Einsatz beim Aufbau dieser Systeme und Leonard Klaus für die unkomplizierte Durchführung der nachfolgenden Vibrationsmessungen.

Viele weitere Personen verdienen Dank für ihre hervorragende technische Unterstützung, namentlich Nicolai Beev, Julia Fenske, Mattias Misera, Alex Pabloki und Rebecca Müller. Des Weiteren danke ich Tobias Leopold, Peter Micke, Fabian Wolf und Jan Christoph Heip für die konstruktive projektübergreifende Zusammenarbeit. Auch die FWJ-ler Jan-Wilke Henke, Ida Sigusch, Jannik Dierks und Julia Buscher-

## *Bibliography*

möhle waren eine wichtige Hilfe.

Birgit Ohlendorf ließ mich an ihrem perfekten Überblick über alle die Promotion betreffenden Formalitäten teilhaben und hat durch ihr Organisationstalent mein Vorhaben maßgeblich unterstützt.

Zu guter Letzt bedanke ich mich bei meinen Eltern und Monique für ihre konstante Unterstützung und unerschöpfliches Verständnis.